Beyond Lithium-Ion Technology: Lithium-Sulfur and Potassium-Ion for Better and Cheaper Batteries

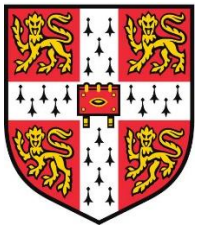

Darwin College

Department of Materials Science and Metallurgy

University of Cambridge

Cheng-Yen Lao

Under the supervision of

Professor R Vasant Kumar

This thesis is submitted for the degree of Doctor of Philosophy

September 2019

It was fun.

Declaration

This thesis is the result of my own work and includes nothing which is the outcome of work done in collaboration except as acknowledged specifically in the text. It is not substantially the same as any that I have submitted, or, is being concurrently submitted for a degree or diploma or other qualification at the University of Cambridge or any other University or similar institution except as specified in the text. I further state that no substantial part of my thesis has already been submitted, or, is being concurrently submitted for any such degree, diploma or other qualification at the University of Cambridge or any other University or similar institution except as specified in the text. The length of this dissertation does not exceed the prescribed word limit imposed by the Degree Committee of the Faculty of Physics and Chemistry.

Cheng-Yen Lao

Beyond Lithium-Ion Technology: Lithium-Sulfur and Potassium-Ion for Better and Cheaper Batteries

Cheng-Yen Lao

Abstract

Large-scale energy storage is one of the key components to power a sustainable future. While lithium-ion batteries (LIBs) have revolutionised our modern lifestyles, the cost of lithium resources and limited energy density that can be safely accessed have limited their potential as large-scale energy storage systems. Lithium-sulfur batteries (LSBs) and potassium-ion batteries (KIBs) are studied as the alternatives due to the high energy density sulfur and cheaper potassium.

In the first part of this PhD project, metal oxides are *in situ* integrated with conductive and flexible carbon framework as the LSBs interlayer, for the first time, to mitigate active material loss. The composite prepared has a large TiO_2 content that can chemically trap polysulfides and a high porosity CNF scaffold for physically hosting the polysulfides. The combined results in the interlayer increase initial discharge capacity and prolong the cycle life as compared to the cell without this interlayer.

In the next part of this PhD project, a new ion storing mechanism is designed to compete for the diffusion limitation and the structural deterioration of KIB electrodes. Unlike a rigid oxide electrode, the oxygen deficient loose-layered potassium titanates (LL-KTO) anode delaminates and restacks reversibly upon charging and discharging, to name it, stacked ↔ sliced structural transformation. This mechanism allows for large storage of K^+ ions in the electrode with net-zero structural deterioration during cycling. Subsequently, layered sodium titanates (L-NTO) are prepared to examine whether stacked ↔ sliced structural transformation mechanism can be engineered in sodium-ion storage. Nevertheless, as evidenced by the electrochemical performances, L-NTO stored sodium with intercalation.

The work conducted in this PhD project provided essential knowledge on methods for mitigating active material loss in a sulfur based battery and mechanism on how to efficiently store potassium.

Acknowledgment

First and foremost, I would like to express my deepest appreciation to my supervisor Professor Vasant Kumar, who has been a tremendously important mentor to me. It is my privilege to learn from his knowledge, experience and the excellent example he sets as a successful scientist.

I would also like to extend my heartfelt thanks to Dr Yingjun Liu, Dr Kai Xi, Dr Wei Wang and Dr Teng Zhao, who has been brilliant support for my research. My appreciations also go to Mr Chenlong Gao, without whom, I would not have been able to conduct the electrospinning process. Appreciations also go to Dr I-Ting Lin and Dr Hyun-Kyung Kim for their advice not only in research but also in life. I would like to thank Dr Giorgio Divitini for the great TEM and STEM images. I would also like to thank Mr Simon Griggs for SEM, Mr Andres Moss for XRDs, Mr Zlatko Saracevic for gas adsorption and textural characterisation and Mr Giovanni Orlando for electronic devices.

Many thanks go to my fellow members of the Materials Chemistry Group for they are involved immensely in my professional and personal life at Cambridge. Our group is a place for friendship, ideas and cakes. It is a pleasure to work and have a joyful time with Dr Rumen Tomov, Dr Paul Coxon, Dr Robert Liu, Dr Peter Knight, Dr Chris Harris, Dr Mike Coto, Dr Vimal Selvaraj, Dr Marcel Yao, Dr Varun Choda, Mr Amir Fakeeh, Ms Siti Norbaya Ahmad Nor, Ms Paulina Librizzi, Mr Liam Bird, Ms Eleonore Poli, Mr Minfei Fei, Mr Nsolebna Jaato and Ms Sarah Firnadya.

Last but not the least, my finest appreciation goes to my parents and my brother for their love, patience and support. Words cannot express how grateful I am for their constant encouragements in my path towards a scientist.

Table of Contents

Nomenclature

0D	0 Dimentional
1D	1 Dimentional
2D	2 Dimensional
3D	3 Dimensional
λ	Wavelength
d	D-spacing
θ	Incident angle
C	Current rate
V	Reduction potential
E	Half-cell reduction potential
R	Universal gas constant
T	Temperature
z	Number of moles of electrons
F	Faraday constant
v	Volume
I_D	Area under curve of D band
I_G	Area under curve of G band
k	Peukert's constant
d	Fractal dimension
r	Inverse of cations per transition metal

C	Capacity
I	Discharge current
LIBs	Lithium-ion batteries
KIBs	Potassium-ion batteries
NIBs	Sodium-ion batteries
LSBs	Lithium-sulfur batteries
KSBs	Potassium-sulfur batteries
SEM	Scanning electron microscope
SEs	Secondary electrons
BSEs	Backscattered electrons
TEM	Transmission electron microscope
SAD	Selected area diffraction
EDS	Energy-dispersive x-ray spectroscopy
STEM	Scanning transmission electron microscope
XPS	X-ray photoelectron spectroscopy
XRD	Powder x-ray diffraction
TGA	Thermogravimetric analysis
P_o	Equilibrium pressure
P	Saturation pressure
EPR	Electron paramagnetic resonance
CV	Cyclic voltammetry
E^0	Standard electrode potential
DFT	Density function theory
VASP	Vienna Ab initio Simulation Package
GGA-PBE	Generalised gradient approximation of Perdew–Burke–Ernzerhof

NMO	$LiNi_xMn_{1-x}O_2$
NCA	$LiNi_xCo_yAl_zO_2$, x+y+z=1
NMC	$LiNi_xMn_yCo_zO_2$, x+y+z=1
TM	Transition metal
LCPs	Long chain polysulfides
SCPs	Short chain polysulfides
CNFs	Carbon nanofibres
CNTs	Carbon nanotubes
MWCNTs	Multiwall carbon nanotubes
SEI	Solid electrolyte interface
GO	Graphene oxide
MHCFs	Metal hexacyanoferrates
PB	Prussian blue
PG	Prussian green
PW	Prussian white
GICs	Graphite intercalation compounds
PNCM	Porous carbon monolith

Chapter 1

Introduction

“Keeping global temperature rise "well below" 2 °C above pre-industrial times”, was an agreement signed by nearly 200 nations in Paris 4 years ago. The rise in temperature originates from the rise of CO_2 content in the atmosphere arising from our growing energy demand. Unfortunately, the energy demand is still growing at a rapid pace[1]. To ensure the targets set in the Paris Climate Agreements can be met, scientists are working hard to transform the eco-system of energy generation, transportation, storing and consumption from fossil fuel to renewable energy[2,3] and off-site to on-site generation[3,4] and storage[5,6]. To take part in this global challenge, this PhD focuses on economical large-scale energy storage systems for renewable energy, specifically, batteries. They are key roles to fuel the next revolution in clean energy generation and transportation. They are efficient, easy to handle and require low maintenance compared to the other storage mechanisms like a hydroelectric dam or an underground compressed air storage.

While lithium-ion batteries (LIBs) are the most successful energy storage system, the fluctuation price and environmental impact for acquiring the raw materials and the stagnated increase in their energy capacity call for alternative technology beyond the lithium-ion technology[5,7–12]. Lithium-sulfur batteries (LSBs)[13–16] with high energy density sulfur and potassium-ion batteries (KIBs)[17,18] with cheaper raw materials are promising alternatives and will both be the focus for this PhD project.

§ 1.1. Aims and report structure

This PhD project focuses on the pressing issues of LSBs and KIBs and is separated into two parts: 1.) LSBs in Chapter 4 and 2.) KIBs in Chapter 5 and Chapter 6.

The key issue for LSBs is the capacity fading associates with active material loss[13–16] while the challenge for KIBs is the inevitable structural deterioration caused by the large K^+ ions[17,18]. Therefore, in this PhD, I will focus on the LSB cathode and KIB anode.

In the first part, I aim to advance LSBs with new cell configuration to minimise the active material loss. I focused on the nano structural design of flexible hybrid interlayers made from oxide nanoparticles and porous carbon. With the ability to chemically and physically trap and re-utilise these active materials, the concept of interlayers may offer the breakthrough for further LSBs development. TiO_2 nanoparticles (78 wt%) were *in situ* integrated with carbon nanofibres (CNFs) as flexible hybrid interlayers. Due to the combined effects of physisorption, chemisorption, and the interlayer's conductive and flexible nature, promising electrochemical properties were delivered experimentally.

In the second part, design of a new ion storing mechanism for potassium storage to compete for structural deterioration is reported, focussing on the preparation of layered titanates. By controlling the formation conditions of the titanates, a loose-layered potassium titanate (LL-KTO) was prepared. LL-KTO stored potassium with a new mechanism based on the structural transformation that allowed it to store a large number of K^+ ions with net-zero structural deterioration during cell cycling. As a result, KIB with specific capacity, reversibility and cycle life comparable to LIBs with similar electrodes was successfully demonstrated. To the best of our knowledge, this is reported for the first time. Subsequently, layered sodium titanates (L-NTO) are also prepared to examine whether stacked ↔ sliced structural transformation mechanism can be engineered in sodium-ion storage. Nevertheless, L-NTO stored sodium with intercalation.

The thesis documents my research discoveries in this PhD project on the topic of *"Beyond lithium-ion technology: lithium-sulfur and potassium-ion for better and cheaper batteries"*.

It is structured as follows:

- Chapter 1: Introduction of the background and the aim of this PhD as well as the structure of the thesis.
- Chapter 2: Literature review focuses on lithium-ion batteries and technology beyond, including lithium-sulfur, potassium-ion and potassium-sulfur batteries.
- Chapter 3: A brief introduction of the electrospinning technique, materials characterisation technique and electrochemical analysis carried out in this work.
- Chapter 4: Results and discussion of flexible carbon nanofibre interlayer with highly mounted TiO_2 polysulfide anchors for lithium-sulfur batteries. TiO_2-CNF interlayer is shown to be an effective component of LSBs to improve the electrochemical performances.
- Chapter 5: Results and discussion of oxygen defect chemistry for the reversible transformation of titanates for sizeable potassium storage. A new stacked ↔ sliced structural transformation ion storing mechanism that can facilitate large ion storage without destruction of the electrode during cycling is demonstrated.
- Chapter 6: Results and discussion to examine stacked ↔ slices structural transformation in sodium storage. No evidence of the mechanism of Na^+ ion incorporation with sodium titanates is found to be stacked-slices structural transformation.
- Chapter 7: Conclusion of the key findings in this PhD.
- Chapter 8: Future work for the research that can help progress in potassium-sulfur batteries, a combination of LSBs and KIBs.

§ 1.2. Administrative and organisational aspects

§ 1.2.1. Supervision

The experimental works documented in the thesis were carried out under the supervision of Professor R. Vasant Kumar, Head of Materials Chemistry at the Department of Materials Science and Metallurgy, University of Cambridge.

§ 1.2.2. Research laboratory, collaborations and contributions

The experimental works documented in the thesis were conducted by different experts in the field at institutions as follows:

- **Department of Materials Science and Metallurgy, University of Cambridge, UK**
  Materials synthesis; Scanning electron microscope (SEM); Transmission electron microscope (TEM); Energy-dispersive x-ray spectroscopy (EDS); Powder x-ray diffraction; Raman spectrometry (XRD); Thermogravimetric analysis (TGA); Gas adsorption analysis
  By me
- **Department of Materials Science and Metallurgy, University of Cambridge, UK**
  Transmission electron microscope (TEM)
  With the help of Professor Cate Ducati, Dr Giorgio Divitini and Dr Xiaoyu Peng
- **Maxwell Centre, University of Cambridge, UK**
  Raman spectrometry
  By me
- **School of Materials Science and Engineering, Beijing Institute of Technology, China**
  Electrochemical tests
  With the help of Professor Renjie Chen and Dr Yusheng Ye.
- **Institute of Advanced Structure Technology, Beijing Institute of Technology, China**
  Electrochemical tests; X-ray photoelectron spectroscopy (XPS); Ex situ transmission electron microscope (TEM); Electron paramagnetic resonance (EPR)
  With the help of Dr Wei Wang, Dr Qiyao Yu and Mr Jun Hu
- **State Key Laboratory of Silicate Materials for Architectures, Wuhan University of Technology, China**
  Density functional theory (DFT)
  With the help of Professor Neng Li and Ms Xingzu Chen

Chapter 2

Literature Review

Battery is one of the most ubiquitous devices that dominate the modern day and will continue to be an important element in the coming future[5,7,12]. It is therefore important to understand the history and recent progress of batteries to develop future batteries. In this literature review, the advances and challenges of rechargeable batteries are covered in terms of their underlying chemistries.

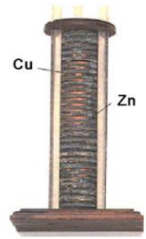

Figure 2-1 – Schematic illustration of the voltaic pile developed by Alessandro Volta in 1799[19].

Our knowledge to design superior batteries can be dated over 200 years ago. In 1799, Alessandro Volta, an Italian physicist and chemist, created the first ever primary (non-rechargeable/primary) battery that can provide constant electrical current through the external circuits (Figure 2-1). This battery consisted of pairs of copper positive electrodes and zinc negative electrodes piled on top of each other as sites for electrochemical reactions. The electrodes were separated by pieces of cloth soaked in brine that worked as the electrolyte to enable ionic movements and insulate electrical conduction between the electrodes. A set of electrodes and the electrolyte formed the basic unit for a battery, an electrochemical cell. Each cell liberated electrons by tandem

electrochemical reactions and supplied current through the external circuits connected both electrodes. This invention soon inspired others to conduct similar experiments which eventually opened a new field of study, electrochemical energy storage, and brought us the most successful secondary (rechargeable) LIBs.

§ 2.1. Lithium-ion batteries

The commercialisation of rechargeable LIBs in 1991 by Sony revolutionised the way we communicate in the past three decades and will continue to fuel the evolution of modern communication and transportation[5,12]. In the early 70s, the concept of chemical intercalation between alkali elements and inorganic compounds was studied and defined as the basis for rechargeable LIBs[20]. In the 1980s, Goodenough's group proposed using Li_xMO_2 (where M is Co, Ni or Mn) as the cathode material for LIBs[21]. Later on, Mohri and co-workers found reversible intercalation of Li^+ ions in to and out of carbonaceous material[22]. Combining their findings, Sony successfully commercialised the first LIBs with graphite-$LiCoO_2$ (C-LCO) rocking-chair configuration with a typical commercial capacity of 145 mAh g^{-1} in 1991. The cell reactions are shown below:

Cathode redox: $LiCoO_2 \leftrightarrow 0.5Li^+ + e^- + Li_{0.5}CoO_2$ Equation 2-1

Anode redox: $C_6 + Li^+ + e^- \leftrightarrow LiC_6$ Equation 2-2

Following the intercalation mechanism in the first LIBs, conversion and alloying mechanism were discovered in the subsequent decades. The developments and challenges of intercalation, conversion and alloying mechanism will be briefly introduced in the following paragraphs.

LIBs with their superior electrochemical performances are deemed to be an important componet that will contribute to a widespread impact in an energy sustainable future. The fundamental advantages of LIBs over other options can be summarised into the followings: 1.) lithium is the most electropositive (-3.04 V vs. Standard Hydrogen Electrode) of all elements that can contribute to the highest possible output voltage, 2.) lithium is the third lightest element that will provide highest possible specific capacity and 3.) lithium has one of the smallest ionic radii to allow rapid ion movements within the cell[11]. A tremendous amount of research has been taking place, the continuous

search for novel material and advance electrochemical mechanism have pushed LIBs to a fresh frontier for better batteries.

§ 2.1.1. Intercalation

An intercalation material allows guest ions to insert into and leave from the solid network it provides. These solid hosts can be transition metal oxides, carbon, metal chalcogenides and polyanionic crystals, and can be further categorised by different crystal structures, as layered, olivine, spinel and tavorite[11,23]. They follow the generalised redox reaction shown below.

$$M_aZ + xLi \leftrightarrow Li_xM_aZ \quad \text{Equation 2-3}$$

Among the cathodes, LCO is the first and most successful metal oxide intercalation material. Its structure is described as a cubic close-packed array of O^{2-} with Co^{3+} and Li^+ ions sitting at octahedral voids in alternate layers[21]. Upon complete delithiation, oxygens will rearrange the material into hexagonal close-packed CoO_2[24]. The performance was best between $Li_{0.5}CoO_2$ and $LiCoO_2$[21,25] in terms of reversibility and specific capacity (~150 mAh g^{-1}). While LCO dominates the rechargeable battery markets, due to its high capacity, low self-discharge and high discharge voltage, the high cost, high toxicity and low thermal stability greatly limit its future applications. Therefore, much work has been done to search for LCO alternatives.

$LiNiO_2$ (LNO) is one of the first material being explored. It shares the same crystal structure and provides a similar theoretical specific capacity of 275 mAh g^{-1} to LCO at a relatively lower cost due to the more abundant nickel as opposed to cobalt[26]. Nevertheless, in stoichiometric LNO, Ni^{2+} ions tend to substitute Li^+ ions during synthesis and delithiation that will, in turn, obstruct lithium diffusion[27]. Furthermore, LNO is even more thermally unstable than LCO[28]. $LiMnO_2$ (LMO) is another promising candidate as manganese is less expensive and toxic compared to both cobalt and nickel[29]. The electrochemical performance is, however, less than ideal for two reasons: 1.) the layered structure tends to transform into spinel structure upon delithiation[30] and 2.) manganese tends to dissolve into the electrolyte when Mn^{3+} ion undergoes disproportionation reaction to form Mn^{2+} and Mn^{4+} [31]. Further efforts have been put into the making of a compound formed by both nickel and manganese,

$LiNi_{0.5}Mn_{0.5}O_2$ (NMO). The addition of nickel is to extend the extraction capacity while maintaining the structural integrity[32].

Beyond conventional layered LNO and LMO, nickel-rich and manganese-rich materials in presence of cobalt to improve the structural stability[33] are promising materials for near term future batteries. For instance, $LiNi_{0.8}Co_{0.15}Al_{0.05}O_2$ (NCA) cathodes with low cobalt content, average cell potential at 3.7 V vs. Li/Li^+ and high specific capacity of 200 mAh g^{-1} can now be found in some high performance batteries[34]. The partial substituting nickel for cobalt can effectively mitigate cationic disorder[35] and doping with aluminium can improve thermal stability[36]. Furthermore, $LiNi_xMn_yCo_zO_2$ (NMC, x+y+z=1) with similar theoretical specific capacity and operating voltage as compared to LCO at a lower cost is being developed. Based on its underlying structure, scientists and their industrial counterparts have tried various combinations among the three elements; $LiNi_{0.33}Mn_{0.33}Co_{0.33}O_2$ (NMC-111) is one the most common form and has been widely applied in commercial batteries[11]. Recently, Ni-rich-$LiNi_{0.6}Mn_{0.2}Co_{0.2}O_2$ (NMC-622) is introduced to the market and $LiNi_{0.8}Mn_{0.1}Co_{0.1}O_2$ (NMC-811) is being designated for future automotive applications. NMC-622 and NMC-811 are high-Ni-content alternatives to NMC-111 with higher energy density at the expense of higher cost and stability[37].

Extensive research has also been focusing on cobalt free polyanionic crystals for reasons of cheaper price, greater safety and less toxicity. The olivine structured $LiFePO_4$ is an example of low-cost and environmentally benign cathode that has been successfully launched in the market[38]. $FePO_4$ is formed upon full delithiation through a two-phase reaction that leads to a specific capacity of 160 mAh g^{-1} with long life time[39]. Other materials, such as the olivine structured $LiFe_{0.5}Mn_{0.5}PO_4$ with 4.5 V [40] and $LiCoPO_4$ with 4.2 V [41] average cell potential have also been reported to be potential replacements of the current LCO cathode in near future. The safety concerns of LIBs also led to the development of $Li_4Ti_5O_{12}$ (LTO), a defected spinel structural material that serves as an anode. The chemical formula of LTO can be re-written as $Li[Li_{0.33}Ti_{1.67}]O_4$, and it can accommodate one lithium at the potential of 1.55 V vs. Li/Li^+ and transform into $Li_2[Li_{0.33}Ti_{1.67}]O_4$ with similar cell parameters to $Li[Li_{0.33}Ti_{1.67}]O_4$ [42,43]. Therefore, one of the most important aspects of LTO is it being a “zero-strain”

intercalation material. Although it has a lower specific capacity (150 mAh g^{-1}) compared to graphite (374 mAh g^{-1}), its high rate performance[44] and greater safety make it attractive for transport applications.

Intercalation mechanism is by far the most reliable and technologically mature for storing Li^+ ion. Nevertheless, the never-ending demand for better batteries continuously drives the advances for higher performing anode and cathode materials. Among those breakthroughs, alloying and conversion materials are promising alternative mechanism to replace intercalation chemistry.

§ 2.1.2. Alloying

In 1971, Dye first demonstrated electrochemical alloying of lithium with various metals, including Sn, Pb, Al, Au, Pt, Zn, Cd, Hg and Mg. Ever since, the lithium-alloying mechanism with metallic and semi-metallic elements have been studied[45]. Although alloy electrodes have advantages over other electrodes due to higher specific capacity and greater safety[46,47], they are plagued with first-cycle irreversible capacity loss and large volume change during cycling that ultimately leads to pulverisation of electrodes and failure of the cell within limited cycles[45,48]. Another merit for alloy electrodes is the moderate operational potential against lithium, for example, silicon anode has an onset voltage potential of 0.3~0.4 V vs. Li/Li^+. A potential that is low enough to avoid energy penalty and high enough to avoid lithium plating[49]. They follow the generalised redox reaction shown below.

$$M + yLi \leftrightarrow Li_yM \quad \text{Equation 2-4}$$

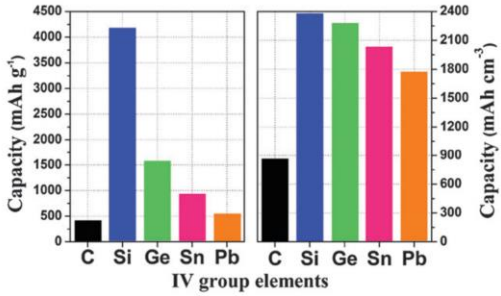

Figure 2-2 – Gravimetric and volumetric capacity of Group IV elements and graphite[45].

Among the metal elements investigated, Group IV elements are of focus owing to their high capacity (Figure 2-2). The theoretical maximum lithium-content is $Li_{22}Si_5$ in Li-Si binary phase[50] and $Li_{17}M_4$ (M = Ge, Sn, Pb) as suggested by Goward *et al*[51]. Silicon has attracted the most attention because of its natural abundance, chemical stability and non-toxicity. The earliest works were conducted in the 1970s at Argonne National Laboratory[52] and General Motors[53,54]. In its pure form, silicon anode may deliver high specific capacity up to 4,200 mAh g^{-1} with attractive operating voltage of 0.3 V vs. Li/Li^+, the severe volume changes (up to 440%), however, severely impairs its use[55–57]. Nevertheless, motivated by the high specific capacity, countless efforts have focused on the structural design of the electrode to overcome the huge volume expansion. Cui group structural engineered silicon into nanowires to mitigate electrode pulverisation and maintain a capacity of 3,500 mAh g^{-1} for 20 cycles at a current rate of 0.2C [49] [1].Scientists have further designed a yolk-shell configuration to host silicon metals to minimise the mechanical instability. In 2012 Liu *et al* designed a silicon-carbon yolk-shell nanoparticle configuration and achieved high capacity (~2,800 mAh g^{-1} at 0.1C) for long cycle life (1,000 cycles) at high Coulombic efficiency (99.84%)[58]. Another approach with Si–SiO_x double-walled silicon nanotubes demonstrated by Wu *et al* reached a lifetime of 6,000 cycles at 12C (Figure 2-3)[59].

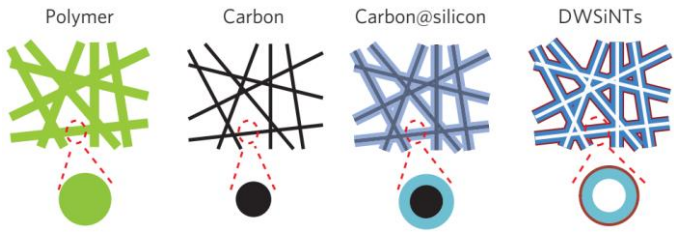

Figure 2-3 – Schematic illustration of the synthesis process for Si–SiO_x double-walled silicon nanotubes[59].

[1] C represents the discharging-charging current rate. It is recognized to be 1C when the battery is discharged from its full capacity in one hour. Current rate is 2C when the discharge time is 0.5 hour.

Other metals have been explored as well. Tin with a lower gravimetric capacity (960 mAh g^{-1}) and cell potential (0.5 V vs. Li/Li^+) but higher conductivity has also been under the spotlight. The severity of fracture problem can be solved by incorporating tin nanoparticles within carbon matrix[60,61] or onto graphene nanosheets[62]. Germanium and lead have not received much attention mainly due to the higher price of germanium and toxicity of lead[11]. Germanium nanowires grown directly on the current collector have, however, shown minimal electrode pulverisation as opposed to other alloy materials[63]. This may be attributed to the strain relaxation enabled by the direct growth of germanium nanowires[64]. Other elements including Group V elements, Ag, Mg, Al, and Zn[45,48,65] have shown ability to electrochemically form alloys with lithium, they, however, suffer from huge volume expansions during lithiation and therefore offer poor cycle life.

Despite the huge volume expansions, alloying materials as alternatives to graphite can be a near term solution for high energy density storage[12] due to their high-specific-capacity. The commercialisation of silicon-based LIBs is just around the corner, and many products have already reached the final stage of marketing, including one from one of the largest LIBs producer, CATL[66].

§ 2.1.3. Conversion

There are two types of conversion mechanisms. Type A, true conversions, involves the complete reduction of binary transition metal compounds, M-X (M = transition metal, X = F, Cl, O, N, P, S, etc), into a metallic state of transition metal embedded within Li-X compound to yield high specific capacities[67,68]. They follow the generalised redox reaction shown below.

$$M_aX_b + (b \cdot w)Li \leftrightarrow aM + bLi_wX \quad \text{Equation 2-5}$$

Many M-X was not regarded as good intercalation host for not having enough or any vacant sites in their structure for lithium insertion. It wasn't until Poizot *et al* in 2000 achieved high reversible capacities with stable cyclability using metal oxides, the active studies of conversions materials finally took off. They showed the formation and decomposition of Li_2O accompanied by the reduction and oxidisation of other metal oxide nanoparticles, MO (M = Co, Ni, Cu or Fe)[69]. Apart from the traditionally well

studied oxides, metal fluorides offer both high gravimetric and volumetric potential and highest operation potential among conversion materials[70]. They are not, however, exonerated from the poor conductivity[71], volume expansion (~25%)[67,72], large voltage hysteresis (difference in charge and discharge potentials)[73] and undesirable side reactions with electrolytes[67] that are associated with most conversion materials.

Poor conductivity and volume expansion can be overcome by synthesising nano-architecture active material as the most straightforward strategy. For example, a $FeF_3{\cdot}xH_2O$ polymorphs with intersecting nano tunnel structure was designed to accommodate Li^+ ions and volume expansion by Li *et al*[74]. Others have incorporated metal fluorides with CNT[75,76] and graphene[77] to enhance electronic conductivity and buffers the volume expansion. Voltage hysteresis that results in poor Columbic efficiency and therefore lower accessible energy is another issue. The reasons for hysteresis are over-potential resulted from the active energy barrier formed to decompose Li-X compounds and the concomitant sluggish kinetics[67]. These compounds are generally thermodynamically stable and have high chemical bonding energies[78] with a large electronegativity towards those anions, particularly for metal fluorides and chlorides[79]. Doping cation or anion has shown great improvement to reduce potential hysteresis. Wang *et al* demonstrated a drop in hysteresis from 700 to 150 mV by partially substituting iron with copper in FeF_2[80]. Furthermore, by partially substitute oxygen into the fluorine lattice, a mixed-anion FeO_xF_{2-x} with high capacity stability (0.14% decay per cycle) and energy density (650 Wh kg^{-1}) was achieved[81]. Hysteresis is most prominent in the first cycle due to the unwanted interactions with electrolyte, including dissolution and formation of the solid-electrolyte interface (SEI)[82]. The dissolution of copper when using CuF_2 as cathodes have been reported[83]. Cu^+ ion can be oxidised to a dissolvable Cu^{2+} ion compound that consumes LiF and therefore hindering the reversible reaction between Cu and CuF_2. The dissolution issue can be more challenging for metal chlorides since LiCl has high solubility in most organic solvents[67]. SEI formed at the surface of cathode has high ionic resistance that can slow the kinetics and increase the hysteresis, furthermore, the continuous volume change may damage the already-formed SEI and result in forming even more SEI[84]. While the formation of SEI is inevitable, electrolyte additives maybe an approach for stable SEI formation[85,86] that may also protect the electrodes[87].

While many issues are still standing between conversion materials and their practical implementation, nevertheless, compared to intercalation and alloying mechanisms, the conversion mechanism is still in its infancy, leaving much room for future developments.

Type B, chemical transformation, of conversion reaction is the lithiation of elemental S, Se, Te, Br and I. It is the transformation of one single phase state to another during charge and discharge[67]. They follow the generalised redox reaction shown below.

$$X + wLi \leftrightarrow Li_wX \quad \text{Equation 2-6}$$

This type of conversion mechanism is usually recognised not as Li-ion technology since lithium does not simply form a compound with chalcogens, instead, a multiple reduction process is involved[88]. Among them, sulfur cathodes in LSBs have the highest theoretical cathode capacity and have attracted the most attention. It will be introduced in detail in section § 2.2.1. Lithium-sulfur batteries.

§ 2.2. Beyond lithium-ion technologies

LIBs are deemed as the most successful electrochemical energy storage mainly due to lithium having the lowest reduction potential, the lightest weight among all metallic elements and one of the smallest ions[11]. Nevertheless, limited energy density that can be safely accessed, foreseeable increase in cost and price and environmental impact due to non-uniformly distributed scarce raw resources bring doubts to LIBs' future development as a dominant source of stored energy[5,7–12]. Furthermore, the energy density, one of LIBs' most important merit, has reached a bottleneck at ~250 Wh kg^{-1}. It is therefore important to research into alternatives with cheaper and more sustainable raw materials for higher energy density. Among the alternative technologies, LSBs[13–16] with high energy density and KIBs[17,18] with cheap raw materials are of interests and will be introduced. Potassium-sulfur batteries (KSBs)[89–93] that combined both high energy and cheap raw materials will also be briefly introduced. Sodium-ion batteries (NIBs) will be briefly mentioned for comparison with KIBs.

§ 2.2.1. Lithium-sulfur batteries

Sulfur, the third abundant elements on the earth crust, often in the form of by-product from oil and natural gas refinement, is also the most promising active material for next generation batteries. It has a theoretical cathode capacity of 1,673 mAh g^{-1}, an average output voltage of 2.15 V and an energy density of 2,500 Wh kg^{-1} [13–15] [2]. LSBs are also one of the most prominent systems beyond LIBs that reached maturity in the research and currently hold the greatest chance for full-out commercialisation. LSBs were first considered in the 1960s when Herbert and Ulam reported the concept of utilising sulfur, followed by Argonne National Laboratory in 1967 [94]. Nevertheless, LSBs back then were plagued with low capacity output and rapid capacity decay. It wasn't until 2009 when Nazar and co-workers proposed a revolutionary high capacity nanostructured conductive mesoporous carbon-sulfur cathode that made LSBs performed for 20 cycles with good cycle stability and delivered 80% of theoretical capacity in the first cycle[95]. Since then, more extensive works have allowed scientists to turn the previously poorly performed LSBs into systems that can achieve long cycle life and high Coulombic efficiency without sacrificing energy density. Much progress has been seen over the past 10 years and commercial products are within reach.

Rechargeable LSBs are composed of an active sulfur cathode, organic liquid electrolytes and a lithium anode (Figure 2-4a). LSBs operate by a multi-step reduction of sulfur during discharge and form various intermediate polysulfide species that combine with Li^+ ions (Figure 2-4b). The discharge process involves two electrons per sulfur atoms and is completed upon full conversion to Li_2S [16]. The overall redox reaction is described as below.

Cathode redox: $S_8 + 16Li^+ + 16e^- \rightarrow 8Li_2S$ Equation 2-7

Anode redox: $16Li \rightarrow 16Li^+ + 16e^-$ Equation 2-8

[2] Both theoretical capacities for current LIBs and LSBs are based on active material. The commercial LIBs has a specific capacity of ~250 Wh kg^{-1}, this number is based on the total weight of the battery. As for LSBs, if all the other components were taken into account (including the anode, separator current collector and electrolyte weight), the practical capacity will be around ~600 Wh kg^{-1}.

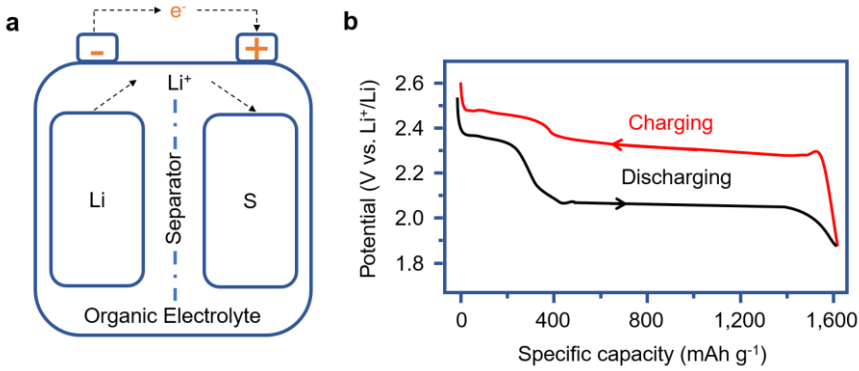

Figure 2-4 – Schematic illustrations of **a**, A typical LSB. **b**, A typical cyclic voltammetry plot of LSBs to illustrate the multi-step reaction during discharging and charging.

During discharging, the lithium anode is oxidised into Li^+ ions and e^- that further migrate to the sulfur cathode through electrolytes and external circuits, respectively. At the cathode, the multi-step reductions take place can be generally related nominally to two main plateau discharge-charge voltage profile as presented in the following reactions (Equation 2-9 to Equation 2-12) and in Figure 2-4b:

High and steep planar plateau: $S_8^0 + 4e^- \rightarrow 2S_4^{2-}$ Equation 2-9

$$E_H = E_H^0 + (RT/z_HF)\cdot\ln(S_8^0/(S_4^{2-})^2) \quad \text{Equation 2-10}$$

Long and planar plateau: $S_4^{2-} + 4e^- \rightarrow 2S^{2-} + S_2^{2-}$ Equation 2-11

$$E_L = E_L^0 + (RT/z_LF)\cdot\ln(S_4^{2-}/(S^{2-})^2(S_2^{2-})) \quad \text{Equation 2-12}$$

Where E is the half-cell reduction potential, R is the universal gas constant, T is the temperature in Kelvins, z is the number of moles of electrons takes place in the reaction and F is the Faraday constant.

The first plateau represents reductions that take place from ~2.3 V, where S_8 is reduced to S_4^{2-} forming Li_2S_4 with Li^+ ions. Although the as-written reaction seems simple, the actual process is a series of lithiation process from the initial cyclo-S_8 ring to various long chain polysulfides (LCPs) intermediate species that are dissolved in the electrolyte ($S_8 \rightarrow Li_2S_8 \rightarrow Li_2S_6 \rightarrow Li_2S_4$). This reaction chain is represented by the high and steep

plateau in the upper part of voltage profile and contributes to ~25% of the theoretical capacity[13–16]. The second plateau represents further lithiation of the dissolved LCPs into short chain polysulfides (SCPs) by the continuous breaking of S-S bonds and eventual formation of Li_2S (Li_2S_4 → Li_2S_2 → Li_2S). The non-soluble Li_2S will precipitate onto the electrodes. This long and planar lower voltage profile accounts for the remaining ~75% of theoretical sulfur capacity[13–16]. Upon recharging, the reverse process is carried out by oxidising Li_2S back to elemental sulfur in multi-steps.

The reactions that take place during the discharge-charge process show a cycle of sulfur species transition from insoluble form to a soluble form. This is very different from LIBs systems and the primary reason LSBs are trickier to deal with[13–16]. The fundamental challenges revolving around LSBs can be summarised into three main issues as follows[13–16]: 1.) The electronically and ionically insulating nature of both S and Li_2S impede the charge carrier movements in and out of the electrode. This results in poor utilisation of active materials. 2.) The density difference between S and Li_2S (2.03 vs 1.66 g cm^{-3}) leads to the inevitable volume expansion of ~22% upon full lithiation (discharging) and ultimately pulverisation of the sulfur electrode. 3.) The dissolution of LCPs leads to continuous loss of active materials as some of them do not precipitate back onto sulfur cathodes upon full discharge.

The dissolution of LCP intermediates also leads to another pressing issue at the batteries' anode side, the shuttle effect. During discharge, dissolved LCPs diffuse towards lithium anode may be chemically reduced into SCPs. SCPs can diffuse back to the cathode and undergo re-oxidisation to form LCPs again upon recharging. The continuous migration of polysulfides back and forth between two electrodes eventually lead to a shuttle tunnel that is in principle an internal short circuit that causes self-discharging. Furthermore, instead of shuttling back to the cathode, the SCPs may precipitate at the anode and cause passivation and structural change at the lithium metal surface, respectively leading to a rise in internal resistances and instability. The recent achievements to overcome the challenges faced in LSBs will be introduced in the following sub-sections, from the cathode to the anode side.

§ 2.2.1.1. Cathodes

Many of the challenges are now addressed with functional nanomaterials especially at the cathode side. By designing nanostructured sulfur cathode, the utilisation rate and stability of active materials can be improved. The ideal structure/material to host sulfur should satisfy a few features: 1.) large conductive surface area, 2.) short[3] electronic and ionic transport pathway to reach sulfur/polysulfides, 3.) sufficient structural voids for efficient volume expansion restraint, 4.) closed structure to confine both non-polar sulfur and polar sulfide/polysulfides and 5.) a buffer layer between sulfur species and electrolyte to minimise dissolution and shuttling in order to suppress active materials loss[13,96].

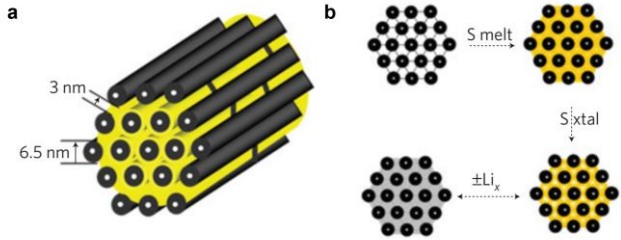

Figure 2-5 – Schematic illustrations of CMK 3-S cathode. **a**, Structure. Yellow: sulfur; Black: CMK-3. **b**, Synthesis process[95].

Carbon is one of the most researched materials with numerous nanostructure designs for hosting sulfur[94]. Exploiting the hydrophobic nature shared between them, carbon materials work as adsorption carriers for sulfur. The significant breakthrough for carbon material as sulfur host material was the same discovery Nazar group made that brought many years of advancement in LSBs in 2009 as aforementioned[95]. A highly ordered nanostructured carbon-sulfur cathode prepared from sulfur infiltrated CMK-3 mesoporous carbon was used as a showcase. CMK-3 is a carbon scaffold consisting of

[3] The normal thickness of sulfur coating onto electronic conductive support is ~50 nm. By calculating the capacity difference between theoretical value and one of the best reported performance of LSBs at 1,030 mAh g^{-1} [111], we can estimate the penetration depth of electron into sulfur is ~30 nm.

arrays of 6.5 nm hollow carbon rods with uniform 3-4 nm channel voids (Figure 2-5). With 70 wt% of sulfur loading, the material displayed an initial specific capacity of 1,005 mAh g^{-1} with 20 stable cycles at 0.1C. Other nanostructures are detailed in the following paragraphs.

1D carbon nanotubes (CNTs) were one of the first carbon material employed into LSBs cathode. The high aspect ratio allows them to form self-assembled interconnected links that provide long range electronically conductive pathways[16,94]. Lee and group were among the earliest group to use CNTs[97]. By mechanically mixing 20 wt% of multi-walled CNTs (MWCNTs) to the sulfur cathode as conductive agents, the initial discharge specific capacity was improved from 400 to 485 mAh g^{-1} and retention capacity was increased from ~100 to 300 mAh g^{-1} after 50 cycles at 1/16C. The 3D structural modification with an electronically conductive MWCNTs matrix greatly improved the sulfur utilisation and cycle life, but the poor contact between sulfur and carbon resulted in limited cell performances. In a later attempt by Yuan and co-workers, sulfur was coated onto carbon at 155 °C, a temperature where sulfur shows the lowest viscosity, for more intimate contact. With only 17 wt% of MWCNT, the cell outperformed the former group by having a reversible capacity of 670 mAh g^{-1} after 60 cycles[98]. Nevertheless, the carbon-sulfur cathode was plagued from open electrolyte exposure which further caused significant detachments of Li_2S from the carbon surfaces. Cui group discovered the weak interactions between non-polar carbon and polar sulfide/polysulfides were the main reason for that phenomenon and alleviated this problem by modifying the carbon surface with amphiphilic polyvinylpyrrolidone (PVP), which anchored firmly onto carbon with its non-polar carbon backbone and bond strongly to lithium sulfide/polysulfides with its polar amide groups. As, a result, high capacity retention was achieved at 97% for the PVP treated cathode in the first 100 cycles at 0.2C whereas the untreated cathode decayed more than 30%.

Heteroatom modifying carbon surface was another attempt used to improve carbon cathodes. The *ab initio* computations suggested nitrogen doping minimises the loss of sulfide/polysulfides and favours the delivery of Li^+ ions to sulfur species[99]. Based on the calculations, Peng *et al* prepared a N-doped CNTs cathode that yielded 70% capacity retention from an initial capacity of 937 mAh g^{-1} after 200 cycles at 1C[100]. An oxidised

CNTs cathode was prepared as well. It showed stronger binding energy with sulfur species but poorer cycling performances. The authors concluded that, apart from a strong affinity for sulfur species, the electronic conductivity of the cathode is of equal importance. Therefore, some of the more recent approaches combined CNT with highly conductive graphene to form multidimensional nano carbon framework[101,102]. Apart from the high electronic conductivity to facilitate fast electron transportation, graphene has large surface area to accommodate sulfur and surface functionalisation durability for sulfide/polysulfides chemical encapsulation[13,15].

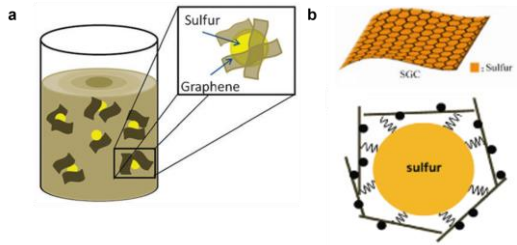

Figure 2-6 – Schematic illustrations graphene-sulfur composites. **a,** Graphene enveloped sulfur cathode[103]. **b,** Graphene wrapped sulfur cathode[105].

Evers and Nazar used a scalable chemical method to *in situ* reduce graphene oxide (GO) to graphene with sodium polysulfide and encapsulate micron-sized sulfur within the graphene networks by C-S interactions (Figure 2-6). The graphene-sulfur composite cathode exhibits one of the highest sulfur loading (87%)[103]. A similar methodology was carried out by Sun group[104]. In both cases, the cell performances were limited with capacity degradation caused by dissolved polysulfide shuttling. It was concluded that the pristine hydrophobic graphene cannot effectively chemical-adsorb the polar polysulfides, furthermore, the graphene with large interlayer pores is not the ideal structure to confine soluble polysulfides. Based on this conclusion, Wang and co-workers coated submicrometer sulfur particles with hydrophilic polyethylene glycol (PEG) and enclosed them within carbon black decorated graphene sheets (GSs) (Figure 2-6b) as sulfur cathode[105]. The array of GSs would suppress polysulfides shuttling and improve overall electronic conductivity. Whereas the PEG coating functioned as a buffer to limit sulfur growth, a cushion to accommodate volume expansion and most

importantly, a chemical trap for polysulfides. As a result, this unique design showed a reversible specific capacity of ~600 mAh g^{-1} for over 100 cycles.

Further attempts by *ab initio* computation showed the hydroxyl group commonly found linked to GO can create chemical gradients that limit polysulfides diffusion[106]. Based on the calculations, Zu and Manthiram fabricated hydroxylated graphene-sulfur (GNSOH-S) cathode[107]. GNSOH-S exhibited astonishing utilisation of active materials and efficient binding with polysulfides evidenced by the superior cycling performance compared with pristine graphene cathode. At 1C, the GNSOH-S had a reversible capacity of ~1,000 mAh g^{-1} after 50 cycles whereas the pristine graphene cathode showed merely ~400 mAh g^{-1}.

Apart from chemically mitigating active material loss, other methods focused on morphological tailoring the graphene surface to create nanopores that physically hold sulfur and limit sulfur-electrolyte interaction. Either through post hydrofluoric treatment[108] or *in situ* facile oil-water synthesis[109], a large amount of uniformly distributed active nanopores are created on the graphene surface to encapsulate sulfur particles. This structure effectively averted physical contact between sulfur species and electrolyte and therefore suppress polysulfides diffusion compared to the untreated graphene surface. The voids also provided sufficient space for volumetric expansion.

3D hierarchical skeletons based on multidimensional nano carbon are among recent efforts to improve carbon-based sulfur cathode. Chen's group integrated 1D MWCNTs-S composite into GS interlayers as a composite cathode (Figure 2-7). The carbon matrix formed by vertical oriented CNTs and planar graphene facilitates fast electron/ion transfer, the pores created were ideal for fast ion diffusion and the mechanical flexibility from GSs provided sufficient volume expansion buffer. More importantly, the functional oxygen group on the graphene surface and the physisorptive MWCNTs generated collaborative effects to suppress polysulfide shuttling[101]. Du *et al* took this idea to the next level by incorporating 0D carbon nanoparticles, 1D CNTs and 2D graphene together to prepare a carbon host for high sulfur loading (90 wt%)[102].

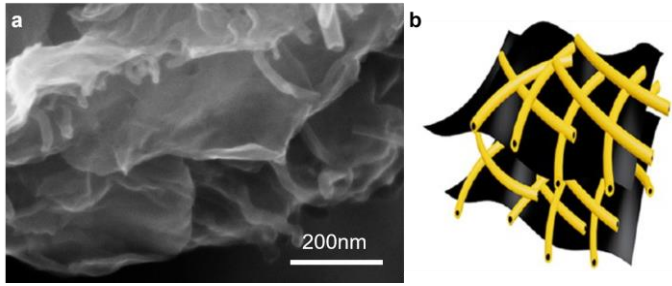

Figure 2-7 – Morphology and structure of GC-MWCNT cathode. **a,** SEM image. **b,** Schematic illustration[101].

Overall, the chemical and physical developments for carbon-sulfur cathode improved the cell performances. With doping heteroatom, grafting functional group or tailored nanopore surface, effective active material utilisation and polysulfides dissolution suppression and can be achieved. Furthermore, the idea of multidimensional nanocomposite by combining a highly electric conductive network with porous sulfur host deliver outstanding sulfur species immobilisation and high specific capacity.

Apart from carbon materials, inorganics are promising carrier materials for sulfur. The intrinsically polarised surfaces induced by oxygen, nitrogen or sulfur atoms have a strong chemical affinity towards polysulfides[13] and were first used as additives in the sulfur cathode. $Mg_{0.6}Ni_{0.4}O$ nanoparticles were initially added to acetylene black-sulfur cathode to mitigate polysufides shuttling by Song *et al*[110]. The authors further discovered not only the electrochemically inactive $Mg_{0.6}Ni_{0.4}O$ could effectively bond with polysulfides, but the oxide also worked as a catalyst during sulfur reduction.

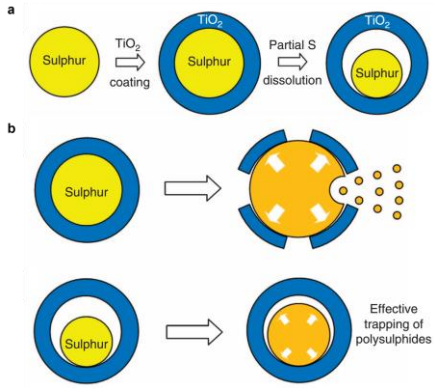

Figure 2-8 – Schematic illustrations of yolk-shell S-TiO_2 composite cathode. **a,** Synthesis process. **b,** Lithiation process comparison between composite without and with extra voids[111].

Cui group utilised inorganics from a different perspective by using inorganics as a sulfur host instead of merely additives. They reported a yolk-shell structure S-TiO_2 composite design[111]. Monodispersed sulfur nanoparticles were uniformly coated by TiO_2 shell followed by the dissolution of partial sulfur to create internal void space within the shell as shown in Figure 2-8a. In addition to the delicate sulfur encapsulating design, the hydrophilic Ti-O and hydroxyl groups' rich surface would bind favourably with polysulfides, therefore, reducing their dissolution and migration. The co-effective properties prompted excellent overall electrochemical performances and demonstrated capacity fade rate as small as 0.033% per cycle over 1,000 cycles at 0.5C with an initial discharge capacity of 1,030 mAh g^{-1}. The internal voids were the key for the brittle TiO_2 shell to sustain volume expansion and remain structurally intact. Without the extra spaces, the volume expansion would create fractures over the TiO_2 protective layer and eventually cause shell cracking which leads to open contact between polysulfides and electrolyte as shown in Figure 2-8b.

The above cases have presented one or more attractive aspects of metal oxides, however, the non-conductive nature for inorganics remain an area for improvements. Non-stoichiometric Magéli Ti_nO_{2n-1} [112] and MXene Ti_2C [113] with metallic conductivity and inherently functionalised surface were among the materials examined as potential

LSBs cathodes. The high conductivity of these materials arose from oxygen and carbon-deficient nature respectively. On top of that, both materials exhibited strong sulfur species attraction at low-coordinated titanium atom sites on the surface through Ti-S bonding. Experimentally, Cui group prepared sulfur-infiltrated TiO_2, Ti_4O_7 and Ti_6O_{11} composites to prove the concept. Ti_4O_7-S cathode with the highest conductivity showed exceptional performances of high capacity retention (99%) over 100 cycles with an initial capacity of 1,044 mAh g^{-1} at 0.1C [112]. Furthermore, Liang and co-workers demonstrated a high discharge capacity of 1,090 mAh g^{-1} and minimal decay of only 0.05% per cycle over 650 cycles at 0.5C with Ti_2C-S composite[113]. The two studies established the predominant feature of the functional surface environment for strong sulfur binding and high electrical conductivity of oxygen/carbon-deficient inorganics. These findings can be generalised to other inorganic compounds[112,113].

Conductive polymers, another class of materials, have inherently conductive nature to promote fast electronic transfer, elastic and flexible nature to accommodate volume expansion and readily equipped functional groups to trap sulfide/polysulfides[13–16]. In addition to their intrinsic properties, the polymer synthesis routes usually involve *in situ* polymerisation in aqueous solutions which favours sulfur surface modification. Inspired by the improvements in stability brought by organosulfur and electro-polymerised compound in LIBs[114], Wang and co-workers were one of the first group to introduce conductive polymer as additives into LSBs cathode[115]. The authors thermally mixed polyacrylonitrile (PAN) with sulfur at 300 °C. Extensive research was carried out ever since.

Similar to inorganic compounds, conductive polymers are usually tailored into different morphology. Wu group prepared three sulfur-polythiophene (PT) core-shell composites with different S-PT ratios as cathodes[116]. The best electrochemical performance composite did not have the highest conductivity nor the highest active material content but a balance between the two. Other attempts focused on mechanically accommodating the volume expansion. Zhou and co-workers developed the yolk-shell nanoarchitecture using polyaniline (PANI) as the shell[117] around the same time Cui group designed the S-TiO_2 yolk-shell composite[111]. Both groups created internal voids by partial sulfur removal, however, the difference lied with the

formation of 3D cross-linked disulfide network through the vulcanisation between PANI and S in Zhou's composite. The PANI-S composite delivered an initial specific capacity of 1,101 mAh g^{-1} at 0.2C with 30% cycle fade after 200 cycles. The authors drew to the same conclusion with Cui group[111] that extra internal voids played a vital role to buffer the volume expansion and maintain the shell integrity.

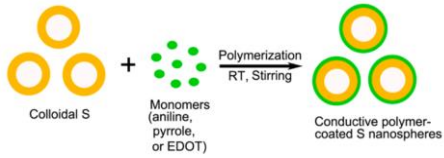

Figure 2-9 – Schematic illustration of the synthesis process for various polymer coated hollow sulfur composite cathodes[118].

Instead of using solid sulfur core, hollow sulfur nanoparticles coated with PANI, polypyrrole (PPY) and poly (3,4-ethylene dioxythiophene) (PEDOT) were fabricated by Li and co-workers to compare chemisorption ability of different conductive polymer on polysulfides[118]. PEDOT was found to be the best coating material and additives to the sulfur cathode. With initial discharge capacity of 1,165 mAh g^{-1} and reversible capacity of 780 mAh g^{-1} after 500 cycles at 0.5C, it outperformed the 726 and 500 mAh g^{-1} reversible capacity by PPY and PANI coating respectively. The theoretical calculations for chemical interactions between polymers and sulfur species revealed PEDOT had the strongest binding energy to sulfide/polysulfides which agreed with the experimental data[118].

In general, each class of materials offered distinctive advantages toward tackling the fundamental challenges of LSBs. The optimum cathode material would be a hybrid cathode that accommodates sulfur and traps polysulfides at the same time. This, however, will complicate the design. By placing an interlayer that only traps the polysulfide[14] between the separator and a cathode that only hosts sulfur, not only can sulfur loading be maximised[119], the cathode design can also be simplified. This interlayer is a platform for polysulfide-adsorption materials that were once incorporated in the cathode.

§ 2.2.1.2. Interlayers

It is important that this "interlayer" is not to be confused with the molecular interlayer between 2D nanosheets, and most importantly not to be confused with a separator. The interlayer between nanosheets is a space between those sheets and a separator is a film that permits the migration of Li^+ ions and prevents a short circuit between the two electrodes. Interlayer works as an extra barrier to capture the theoretically inevitable dissolution and shuttling of polysulfide towards anode through either chemisorption, physisorption or combined adsorption and ultimately provide reactivation and re-utilisation sites for dissolved polysulfides (Figure 2-10). A functional free-standing/flexible interlayer material requires a detailed design as followings: 1.) smooth contact with the surface of the cathode to prevent a rise in internal resistance, 2.) porous structure as polysulfide trapping and re-utilisation site and 3.) sufficient sites for polysulfide chemisorption[14,120]. Since the main purpose of an interlayer is to suppress the loss of polysulfides, the design of which shared many similarities with the cathode.

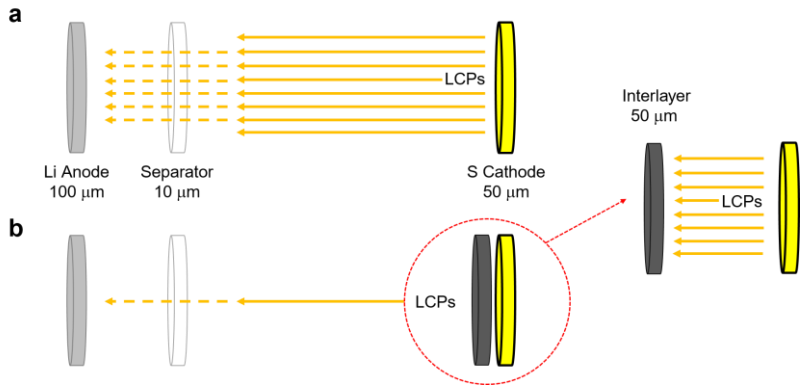

Figure 2-10 – Schematic illustration of the concept for inserting interlayer. **a,** Without and **b,** with an interlayer.

The interlayer concept was first introduced by Su and Manthiram[121]. The authors employed a bi-functional MWCNT film between the separator and sulfur cathode as an interlayer as well as a pseudo-upper current collector. The inserted conductive fibrous interlayer played two roles: 1.) trapping and storing polysulfide at the pores on

and between the fibres to constrain and mitigate dissolution and migration of active materials and 2.) reducing the interface resistance to enhance more efficient charge transfer. After pairing the interlayer with a pure sulfur cathode, significant improvements were demonstrated: with the interlayer, the cell maintained a capacity of 962 mAh g^{-1} (66% capacity retention) after 50 cycles at 0.2C, whereas, the cell without the interlayer merely showed a capacity of ~330 mAh g^{-1} (49% capacity retention) after 50 cycles under same conditions. Manthiram group further extended this idea by introducing hydroxyl functional groups onto the carbon paper through alcohol-alkaline/thermal treatment to chemically intercept the migrating polysulfides[122]. The group also investigated the physisorption of polysulfides by carbonising a leaf to form a carbon skeleton with a structural gradient of microporous and mesoporous adsorption sites[123]. Further works have been done to provide insights into the reactivation and re-utilisation mechanism of the polysulfide-trapping layer[124–126]. The pore size distribution of the interlayer structure becomes important as sulfur loading increases. The associated collective amount of migrating polysulfides to be trapped would rely on more pore volume to accommodate them without jeopardising Li^+ ion transportation and blocking electrolyte path way[14,120]. Unlike micropores, larger mesopores and macropores can provide more pore volume which is advantageous while building reactivation layer. On the other hand, the compatible size between micropores (<2 nm) and polysulfides (Li_2S_8 ~2 nm)[127] made micropores a more sensible choice. Careful selection of micropores, mesopores, macropores or combinations of these is the key to enhance cell performance at high sulfur loading and high-rate cycling. Manthiram's group have demonstrated good cyclability with bimodal micro-/mesoporous carbon paper interlayer at high rates of 10C and 15C for over 250 cycles[128].

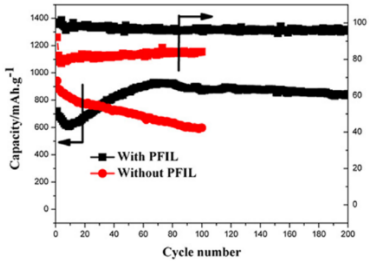

Figure 2-11 – Cyclability of CMK 8-S cathode with and without PPY interlayer[129].

Similar to the development trend with the sulfur cathode, carbon materials, polymers and inorganic compounds are the three main class of materials exploit for designing better interlayers[14]. Ma and co-workers were the first to employ PPY nanoparticles as functional interlayer[129]. The results were effective due to the conductive nature of PPY and the abundant binding sites and strong chemisorption between PPY and polysulfides that constrained polysulfides migration. By pairing it with a CMK 8-S cathode, the cell delivered an initial discharge capacity of 719 mAh g^{-1} and a capacity retention of 846 mAh g^{-1}after 200 cycles at 0.2C. Interestingly, the capacity dropped in the first few cycles and rose for 70 cycles. This indicated a gradual increase in active material utilisation rate as shown in Figure 2-11. A phenomenon reflecting how interlayer physically blocking efficient Li^+ ions diffusion towards sulfur cathode for redox reactions. Therefore, not all sulfur was reacted in the first few cycles. Nevertheless, this successful attempt motivated the group to design a self-assembly PPY nanotube film with greater pore volume and higher specific surface area[130]. By yielding more pore structure with its nanotube scaffold the pairing cathode can have sulfur loading up to 3.0 mg cm^{-2}. As a result, a high reversible capacity of 712 mAh g^{-1} after 300 cycles at 0.5C with an initial capacity of 1,102 mAh g^{-1} was achieved.

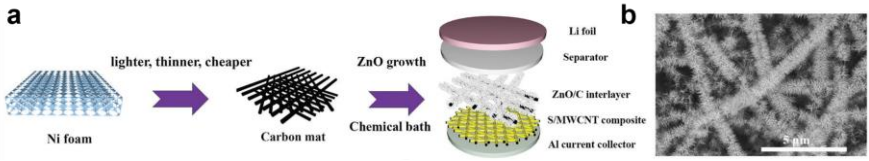

Figure 2-12 – From of ZnO-Ni foam to ZnO-C interlayer. **a**, Schematic illustrations of interlayer evolution. **b**, SEM images for ZnO-C interlayer[131].

The readily robust porous structure and high electrical conductivity made metal foam a logical choice at first glance. By incorporating nickel foam foil with the raw sulfur cathode, Zhang *et al*[132] increased the cell reversible specific capacity from 424 to 604 mAh g^{-1} at 0.2C after 80 cycles. Nevertheless, the extra weight imposed by nickel foam dramatically undermined the benefits. Our group extended these ideas and took inspiration from brush-like micro villi for nutrient adsorptions to design zinc oxide (ZnO) nanowires decorated conductive substrate as the chemisorption interlayers to obtain both high trapping capabilities and polysulfide re-utilisation rates[131] (Figure 2-12). ZnO nanowires were grown on flexible, lightweight micro-/mesoporous CNF mat. Carrying a high sulfur loading of 3 mg cm^{-1}, the cell achieved a reversible capacity of 776 mAh g^{-1} after 200 cycles at 1C with only 0.05% average capacity fading rate per cycle. The combination results of chemical, mechanical and physical effects were attributed for this successful demonstration. Chemically, the ZnO nanowires provided strong chemical gradients that kept migrating polysulfides largely immobilised within the well-structured, interconnected framework. Mechanically, the brush-like arrangement enhanced the effectiveness of polysulfide trapping by reaching out to the migrating species. Physically, the conductive CNFs facilitated fast electron and ion transports that boosted active material re-utilisation rate.

The concept of interlayer, polysulfide-reactivation layer, may be the most promising structural design in LSBs that has the potential to curb one of the notorious challenges: dissolving and shuttling of polysulfides. Furthermore, it is also the most prominent method to allow a high sulfur loading cathode. In this dissertation, my recent work of designing a free-standing flexible TiO_2-CNF mat as chemi-/physisorptive interlayer will be presented.

§ 2.2.1.3 Anodes

The vulnerable corrosive nature of lithium by shuttled polysulfides leads to non-reversible deteriorated surface that undermines the high theoretical capacity of lithium. In addition to that, the dendritic growth of redeposited lithium and uneven distribution of SEI are also the reason for poor cyclability and safety concern. *In situ* and *ex situ* protection strategies for lithium anode are developed in order to address the challenges and prolong the performances.

One of the methods is to form passivation SEI *in situ* by electrolyte additives. Followed by the work of Mikhaylik *et al* on their discovery about the suppression of polysulfides corrosion on lithium surface with N-O bonds containing additives[133], a major breakthrough was led by Aurbach group during a study about SEI formation in the presence of $LiNO_3$[134]. The group discovered that $LiNO_3$ can transform into Li_xNO_y and/or Li_xSO_y in the presence of sulfur species and both materials can form a protective layer on lithium. As a result of the success, $LiNO_3$ additives are now incorporated in most LSBs. Nevertheless, the explosive nature from the oxidising reagent may cause some safety concern[135]. A safer alternative was reported by Liang' group[136]. The group employed P_2S_5 that effectively forms a passivation layer of ionic conducting Li_3PS_4 with lithium metal. In addition to forming protective SEI, P_2S_5 also formed complexes with insoluble sulfide into species with higher solubility thus alleviate sulfide precipitation onto anode surface.

As opposed to *in situ* formation of a protective layer with electrolyte additives during cycling, lithium metal surface could be protected with a physical film coating. One of the most straightforward approaches was to insert a layer of graphite film between anode and separator in order to form a buffer zone between lithium metal and shuttled polysulfides[137]. Other approaches include the work done by Jing and co-workers[138], they spin-coated porous Al_2O_3 nanoparticles thin layer onto lithium surface. In another attempt, Wu group fabricated a uniform layer of Li_3N onto lithium anode by direct reaction of N_2 gas and lithium[139]. The Li_3N protective layer not only shields lithium from polysulfides but also facilities fast ionic transport. Lithium anode was analysed after the cycling tests. A much thinner (~10 μm) lithium sulfide species was formed on the anode surface compared to the one (~100 μm) from the unprotected anode.

§ 2.2.2. Potassium-ion batteries

KIBs may not be the direct substitute LIBs in all areas, but the abundant potassium resources on earth crust make it a very promising cheaper alternative. With 20 ppm of lithium reserved in the earth crust[140] and uneven distribution of the resource, these limitations on lithium resources have caused concerns about the future increase of lithium price[141] but opened up opportunities for alternative alkali-ion batteries. While sodium and potassium hold similar crust abundance (23,000 and 15,000 ppm, respectively)[17], sodium falls short on its electrochemical properties (Table 2-1). The low standard reduction potential at -2.93 vs. E^0 for potassium is closer to -3.04 V vs. E^0 for lithium[18,140], and therefore more ideally as a potential candidate for future energy storage for applications such as low-cost grid-scale energy storage or long life power supply. On the other hand, the high standard reduction potential (-2.71 V vs. E^0) of sodium greatly limits the voltage output and therefore the practicality of NIBs[142]. Furthermore, as suggested by the reduction potential of these three elements in propylene carbonate (PC), a well-known battery solvent, more potential can be exploited from KIBs. As shown in Table 2-1, the potentials are -2.79, -2.56 and -2.88 V for Li^+/Li, Na^+/Na and K^+/K. Additionally, with the common LIBs' electrolyte solvent, ethylene carbonate (EC) and diethyl carbonate (DEC), Komaba group found out that K^+/K has a 0.15 V lower potential as compared to Li^+/Li[143]. That is said, KIBs may deliver a 0.15 V higher cell voltage than LIBs.

Apart from the abundancy and electrochemical properties of potassium, the price for potassium salt is much cheaper than lithium salts. Furthermore, the copper foil current collector in LIBs can be replaced for cheaper aluminium foil current collector in KIBs[140,142]. This reduces the cost and the weight of the cell and addresses the over-charge problem. With all those advantages, the biggest challenge in developing KIBs is the large size of K^+ ions (1.38 Å vs. 0.76 Å for Li^+ ions) that cause sluggish diffusion kinetics and severe structural deterioration as the large cation cycled in and out of the electrode[17,18]. Generally, the performances for sodium and potassium-storage are almost non-exclusively worse than lithium-storage with the same or similar materials. For example, MoS_2[144–146], V_2O_5[147], and titanium oxide-based materials[148–162].

It is therefore essential to design suitable electrode materials that sustain long term structural fluctuation. In the following sub-sections, recent research on KIBs will be highlighted in sections of cathode and anode.

Table 2-1 – Properties of lithium, sodium and potassium[17,163,164].

Properties	Lithium	Sodium	Potassium
Atomic mass (u)	6.941	22.989	39.098
Atomic radius (pm)	145	180	220
Ionic radius (Å)	0.76	1.02	1.38
Voltage vs. SHE (V)	-3.04	-2.71	-2.93
Voltage vs. SHE in PC (V)	-2.79	-2.56	-2.88
Crust abundance (ppm)	20	23,000	15,000
Cost of carbonate (US$ ton^{-1})	6,500	200	1,000
Cost of industrial grade metal (US$ ton^{-1})	100,000	3,000	13,000

§ 2.2.2.1. Cathodes

Intercalating cathodes are the most common cathodes in KIBs research to date. Among them, Prussian blue (PB) used in the first KIBs by Eftekhari[165] and its metal hexacyanoferrates (MHCFs) analogues[166–168] by Cui *et al*, Padigi *et al* and Nazar *et al* are still the top choices for K^+ ion interaction/de-intercalation (Figure 2-13). PB has a chemical formula of $KFe^{III}Fe^{II}(CN)_6$. Having $(C{\equiv}N)^-$ functional groups bond with both Fe^{III} and Fe^{II}, a rigid cubic metal-organic framework is formed (Figure 2-13a inset). Its analogues have a general formula of $A_xM[Fe^{II}(CN)_6]_y{\cdot}zH_2O$, where A is an alkali ion and M is a metal and x is between 0 and 2 (x=0: Prussian green (PG); x=1: PB; x=2: Prussian white (PW)). The valence states of M and Fe ions are the determining factors of whether alkali ions can be hosted. Their 3D open structure has large enough interstitial sites to accommodate large K^+ ions that allow reversible intercalation without severe volume distortion during cycling.

The first potassium cell which Eftekhari demonstrated with PB[165] was tested in a nonaqueous electrolyte solution. The cell cycled over 500 cycles with 88% of its initial discharge specific capacity retained and with comparable K^+ ions diffusivity to that of Li^+ ions. This initial trial inspired the Cui group to examine PB analogues under

aqueous environment. MHCF with M=Ni and Cu were tested in an aqueous electrolyte solution of 1M KNO_3 with more than 66% and 83% of capacity retention after thousands of cycles at high discharging rates of 41.7C and 17C, respectively[166,169]. They further employed *ex situ* XRD to reveal minimal volume expansion during K^+ ion intercalation and single-phase reactions. Although these results suggest MHCFs are promising materials for long-life energy storage, their cell potentials are greatly limited to less than 1.23 V in aqueous environment[170]. It is therefore essential to apply them in nonaqueous organic solvents for a larger potential window.

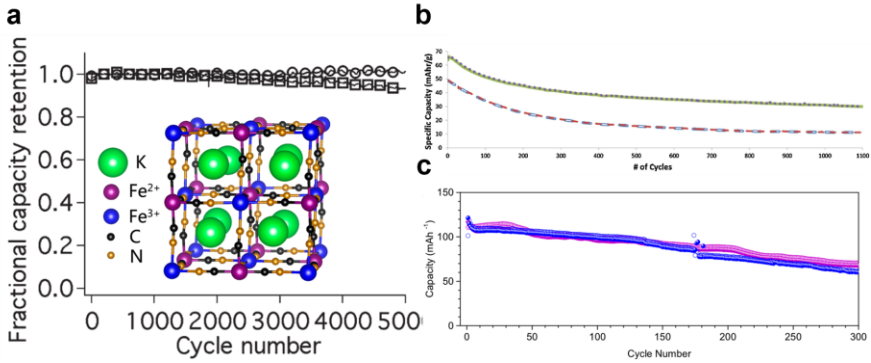

Figure 2-13 – Cyclic performances of **a**, PB, **b**, PG and **c**, PW[166–168]. Inset of (**a**) is the lattice structure of PB[165].

Goodenough group[171] reported a high capacity manganese based MHCFs with the ability to store nearly two K^+ ions into its structure and therefore a high theoretical capacity of 156 mAh g^{-1}. This was much higher than the previous reported MHCFs. Furthermore, the dual reduction couple, Mn^{III}/Mn^{II} and Fe^{III}/Fe^{II} both have high reduction potential centred at 3.6 V. As a result, the cell delivered up to 511 Wh kg^{-1} in an organic solvent. Another PB analogue, PG, with the zero-strain property was synthesised by Shadlike *et al*[172]. It showed minimal lattice deformation of 0.39% after its initial discharge and delivered a specific capacity of 93 mAh g^{-1} after 500 cycles at 5C. Nazar group reported another PB analogue, PW, with high energy density in organic electrolyte[168]. It achieved an energy density of ~500 Wh kg^{-1} after 100 cycles. These experiments successfully demonstrated the advantages of PB and its analogues'

unique structure but not enough knowledge about the intercorrelations between the structure, the operation potential and the species of intercalants.

Recent computational work by Ling *et al*[173] revealed that different alkali ions can intercalate into Fe-HCFs with negligible structural deformation at different preferred intercalation sites. Larger K^+, Rb^+ and Cs^+ ions tend to occupy the body-centred *8c* sites while smaller Li^+ and Na^+ ion prefer face-centred *24d* sites. An important aspect pointing out the correlation between the intercalation voltage and alkali ion species was also reported: larger cations intercalate at higher potentials and thus provide higher energy density. They are 3.08, 3.23, 3.70, 4.09 and 4.13 V for Li^+, Na^+, K^+, Rb^+ and Cs^+ ions, respectively. Experimental works by Piernas-Munoz *et al* supported this work and showed higher cell voltage by 0.211 V for KIBs as compared to that of NIBs[174]. Overall, it showed that KIBs are better alternatives than NIBs.

Apart from hexacyanoferrate compounds, other class of cathodes including layered metal oxides and polyanionic compounds will be introduced. Many of them are analogues to their lithium cathode counterparts.

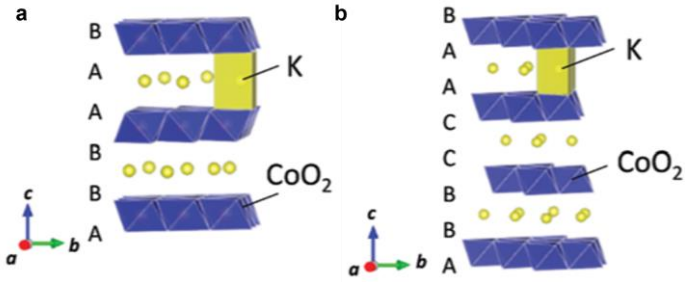

Figure 2-14 – Crystal structures of K_xCoO_2. **a**, P2 and **b**, P3[175].

The phase stability of P2- and P3-K_xCoO_2 with different potassium content was reported by Delmas in 1975[176]. But it wasn't until 2005 when Taniguchi *et al* reported reversibly cycling of K^+ ions in and out of $K_{0.55}CoO_2$[177]. In 2017 Komaba *et al* investigated P2- and P3-K_xCoO_2 (Figure 2-14) as cathode materials for KIBs[175]. The two crystal structures delivered a specific capacity of ~60 mAh g^{-1} for 30 cycles at ~12 mA g^{-1} in a voltage window of 2.0-3.9 V. Furthermore, after comparing the electrochemical

behaviours of Li_xCoO_2 and Na_xCoO_2, they revealed that the interlayer spacing between CoO_2 layers is the predominant factor to determine the intercalation potential and therefore the cell voltage. The larger the interlayer spacing the higher the redox potential. Around the same time, Cedar group[178] and Wang group[179] reported using P2-$K_{0.6}CoO_2$ as K^+ ions intercalation host. Within the potential window of 1.7-4.0 V, microspherical P2-$K_{0.6}CoO_2$ synthesised by Wang showed better cyclability than the granular like ones synthesised by Cedar. At 40 mA g^{-1}, P2-$K_{0.6}CoO_2$ by Wang cycled for 300 cycles with a reversible capacity of 65 mAh g^{-1}, whereas P2-$K_{0.6}CoO_2$ by Cedar decayed to a reversible capacity below 65 mAh g^{-1} after only 10 cycles. Nevertheless, the capacities were still limited. Passerini group synthesised P2-$K_{0.3}MnO_2$ as cathode material for KIBs to increase the capacities[180]. They showed that at different voltage window, 1.5-4.0, 2.0-4.0 and 1.5-3.5 V, the obtained specific capacities were different, 136, 105 and 75 mAh g^{-1}, respectively. Furthermore, they ran the rate performance ability and showed different capacity retention rates for each voltage window; they were 58, 73 and 91%. Although having a lower capacity, cycling within 1.5-3.5 V avoided the irreversible volume changes of two-phase transitions at 3.7 and 3.9 V and therefore retaining more capacities. A similar phenomenon was reported by Cedar *et al* with P3-$K_{0.5}MnO_2$[181]. By decreasing the upper cut-off voltage, the capacity retention improved from 30% to 76% of the initial discharge capacity. To further improve on the performances, Mai *et al* reported a P3-$K_{0.7}Fe_{0.5}MnO_2$ nanowire interconnected framework[182]. This framework provided a stable skeleton for large K^+ ions intercalation and easy access channels for K^+ ion diffusion. As a result, it delivered a reversible capacity of 125 mAh g^{-1} for 45 cycles at 20 mA g^{-1}. Apart from earth abundance iron and manganese, chromium[183] and vanadium[184] based layered oxides were also investigated. $KCrO_2$ and $K_{0.5}V_2O_5$ were both able to deliver reversible capacities of ~90 mAh g^{-1} and show high stability during reversible potassiation/depotassiation.

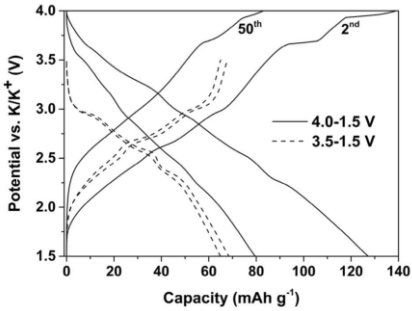

Figure 2-15 – Reducing the cut-off voltage for higher capacity retention[180].

Metal oxides are promising candidates as electrode materials mainly due to their low cost, unfortunately, they suffer from structural distortion imposed by large K^+ ions. This makes them difficult to have long cycle lifes[18,163]. Polyanionic compounds on the other hand exhibit excellent structural stability. As the counterpart of $LiFePO_4$ in LIBs, $KFePO_4$ in KIBs has drawn attentions to the researcher. Yakubovich *et al* synthesised a new type of $KFePO_4$ via hydrothermal[185]. The single crystal XRD revealed a microporous 3D framework with open channels formed by FeO_4 and FeO_5 with PO_4. Those micropores were large enough to accommodate K^+ ions diffused from the electrolyte through the open channels. Unfortunately, the authors did not provide electrochemical results in this work. Applying amorphous $FePO_4$ for alkali ion intercalation was an interesting approach by both Liu *et al*[186] and Mathew *et al*[187]. Mathew *et al* demonstrated the short-range ordered structure was more favourable for large K^+ ions intercalation as compared to crystalline $KFePO_4$. The amorphous materials prepared at low temperature minimised particle growth and allowed these nanoparticles to form voids when self-assembled. This intercluster voids served as hosting sites for large cations insertion and acted as a buffer to volume expansion during ion insertion, thereby increasing both the number of ions stored and cycle life[187]. The intercalation of large cations in crystalline $KFePO_4$, on the other hand, maybe impractical due to the limited space and size of interstitial sites. As a result, the specific capacity delivered by amorphous $FePO_4$, 156 mAh g^{-1} at 5 mA g^{-1}, is higher than most of oxide materials[175,178–184]. Vanadium based polyanions is another class of material

interested to researcher owing to their success in LIBs and NIBs. The KVP_2O_7 with 3D conductive network synthesised by Han *et al* delivered an energy density of ~250 Wh kg^{-1} over 100 cycles[188]. Another approach by Lin *et al* with $K_3V_2(PO_4)_2F_3$ delivered an energy density up to 400 Wh kg^{-1} [189]. Tarascon group reported a new fluorosulfate base polyanion (Figure 2-16), $FeSO_4F$ with large and empty interstitial space (about 4.3 Å x 4.8 Å) readily to host large cations such as K^+ ions[190]. Up to 0.8 K^+ ions can be stored per unit formula, less than 0.9 and 0.85 for Li^+ and Na^+ ions. Nevertheless, the intercalation potential at 3.5 V for K^+ ions is highest of all three. Although, many polyanions can deliver high voltage, most electrolyte would have been decomposed before reaching those voltages. It is therefore essential to develop electrolytes for high potential applications.

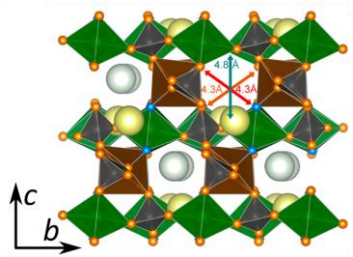

Figure 2-16 – Crystal structure of $FeSO_4F$[190].

The overall performances of cathode materials for KIBs are much lower as compared to those of LIBs and NIBs. Discovering new materials suitable for large ion storage will be a crucial step for further advancing KIBs technology.

§ 2.2.2.2. Anodes

Anode materials can be classified according to ion storing mechanism: intercalation, alloying and conversion. Among the carbon family, graphite with high electronic conductivity, stable electrochemistry and layered structure is one of the most important intercalating materials not just in the infancy state of KIBs research but also in the technological matured LIBs[163]. In LIBs, graphite forms graphite intercalation compounds (GICs) with lithium[191]. Likewise, the formation of GICs between graphite and potassium is possible and was reported by Schleede and Wellmann back in the

1930s[192]. In-depth studies were carried out since the 1950s with different stages of potassiated GICs (K-GICs) being prepared[193–197]. Matuyama reported that these stages occur at distinct temperatures[194]. Nixon and Parry applied XRD techniques to examine the progressive potassium intercalation into XRD. From stage 4 to 1, they identified KC_{48}, KC_{36}, KC_{24} and KC_8, respectively[196], with KC_8 being the fully intercalated K-GIC. These K-GICs have potassium atoms hosted at hexagonal carbon centres in a single layer separated by 4, 3, 2 and 1 un-intercalated graphite layers depending on the intercalation stages (Figure 2-17a). Inevitable volume expansion as the result of potassium intercalation is uniform within any given intercalated graphite layer and is constant for all those un-intercalated graphite layers[197]. Recently, the Grande group used density functional theory (DFT) calculations to study the intercalation energy of Li^+, Na^+ and K^+ ions into graphite[198]. The formation enthalpies for LiC_6 and KC_8 were -16.4 and -27.5 kJ mol^{-1}, while the formation energies for NaC_6 and NaC_8 were 20.8 and 19.9 kJ mol^{-1}. These results of Na-GIC reflect previous experimental works[199,200], that sodium intercalation in graphitic material is in-practical.

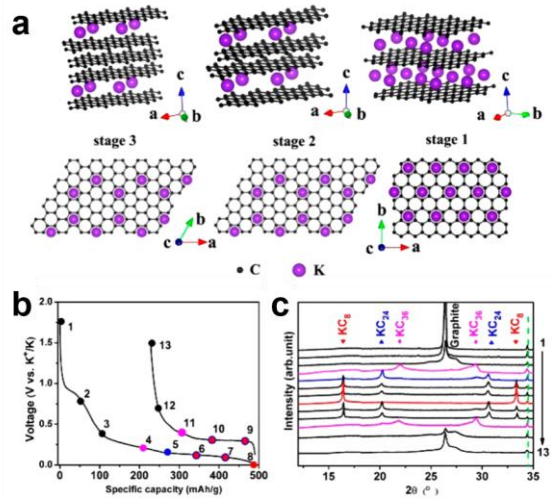

Figure 2-17 – Progressive potassium intercalation into graphite. **a**, Structural representations of stage 3 to 1 K-GICs. **Top:** side views. **Bottom:** top views. **b**, Potential profiles of discharge-

charge in the first cycle at 0.1C. **c**, *ex situ* XRD patterns showing the corresponding state of charge in (**b**)[191].

The electrochemical intercalation of K^+ ions with graphite was first reported by Jian *et al*, Luo *et al* and Komba *et al* around the same time in 2015[143,191,201]. Jian *et* al achieved a high capacity at 273 mAh g^{-1} while the theoretical capacity for KC_8 was 279 mAh g^{-1}. They used *ex situ* XRD (Figure 2-17b,c) to investigate the storing mechanism in graphite and revealed that diffraction peaks for graphite disappeared between 0.3 and 0.2 V followed by the appearance of KC_{36}, KC_{24} and KC_8. A 61% volume expansion was calculated during potassiation leading to rapid capacity decay (from 273 to 100 mAh g^{-1} in 50 cycles at 0.5C). To improve the cyclability, the authors prepared a low-density soft carbon as the host to mitigate structural distortion. As a result, it showed a retention rate of 81.4% after 50 cycles at 2C. In separate work, Jian *et al* use hard carbon prepared by hydrothermal carbonisation of sucrose[202]. Hard carbon exhibits high stability by delivering a reversible capacity of 216 mAh g^{-1} after 100 cycles at 0.1C. That was 83% capacity retention. By blending soft and hard carbon at a ratio of 8:2, the group achieved a reversible capacity of 200 mAh g^{-1} after 200 cycles at 1C with a capacity retention rate of 93% [203]. As aforementioned in previous sections (§ 2.2.2.1. Cathodes), amorphous materials have advantages in providing larger voids to host large K^+ ions as opposed to the restricted space in well-crystalline materials. Inspired by this, Wang *et al* fabricated an amorphous ordered mesoporous carbon[204]. They showed a mere 7% deformation after full potassiation. This flexible form of carbon achieved a reversible capacity of 257 mAh g^{-1} over 100 cycles at 0.18C, the highest reported at that time, and ~150 mAh g^{-1} after 1,000 cycles at 1 A g^{-1}.

Graphene and carbon nanofibres are other popular anode materials for KIBs. Anions doping for carbons[205–210] is an effective strategy to improve the overall performance of carbon materials as it introduce charged defects into carbon and increase locally accessible active sites[211]. Among them, nitrogen doping is the most common and have commercial potential with scalable manufacturing techniques[211]. Share *et al* demonstrated a 6-fold improvement in rate performance of N-doped graphene as compared to undoped graphene[205]. Furthermore, an initial capacity, 350 mAh g^{-1}, exceeding the maximum achievable value for KC_8 was reached. Using *in situ* Raman

technique, they revealed nitrogen's role as activation agent for storage sites and energetic pathway for KC_8 formation. Xie *et al* prepared a pyridinic N-doped porous carbon monolith (PNCM) as an anode to achieve a high capacity of 487 mAh g^{-1} in the first cycle[206]. They further assembled a full cell to evaluate the practicality of PNCM. A high energy density of ~154 Wh kg^{-1} of the full cell was demonstrated (Figure 2-18a). In recent work, Xu *et al* showed that nitrogen doping content was positively correlated to the material capacity[209]. With 4.9, 8.1 and 13.8 at% of nitrogen, N-doped CNFs exhibit initial capacities of 281, 297 and 368 mAh g^{-1}, respectively. The 13.8 at% N-doped CNFs had good cyclability for 4,000 cycles with a reversible capacity of 146 mAh g^{-1} at 2 A g^{-1}. A full cell was assembled against PB cathode and showed a cell capacity of 190 mAh g^{-1} with two discharge plateaus of 3.4-3.9 V and 2.5-3.0 V (Figure 2-18b). Furthermore, a F-doped graphene with a reversible capacity of ~166 mAh g^{-1} at 500 mA g^{-1} after 200 cycles was reported by Ju *et al*[208]. The authors suggested the combined effects of fluorine doping, high surface area, mesoporous structure and a large number of defect sites were the reason for the excellent performance.

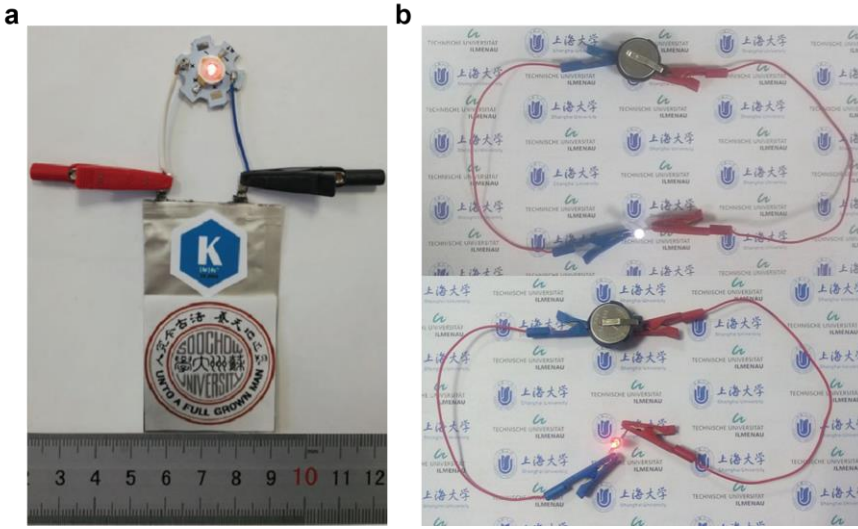

Figure 2-18 – Full cell demonstrations with an LED bulb. **a,** PNCM as anode and PTCDA as cathode[206]. **b,** N-doped carbon nanofibres as anode and Prussian blue as cathode[209].

The overall research focuses on non-graphitic carbon can be summarised to one point: disordered structure originates from either amorphous nature or dopant modification was more tolerable against large K^+ ions, therefore, perform better in terms of cyclability, stability and rate performance.

Layered potassium titanate is another class of intercalating anode for KIBs[212]. The large diffusion channels within both $K_2Ti_4O_9$ and $K_2Ti_8O_{17}$ (8.5 and 7.9 Å, respectively) makes them attractive intercalation hosts for large K^+ ions[153,154]. Kishore *et al* synthesised $K_2Ti_4O_9$ via solid state method[153]. Although an initial discharge capacity of ~80 mAh g^{-1} was achieved at 100 mA g^{-1}, the capacity rapidly faded to ~50 mAh g^{-1} in less than 10 cycles. On the other hand, Zhang *et al* used a hydrothermal method to prepare nanostructured $K_2Ti_8O_{17}$ with stable cycle performance at a reversible capacity of ~120 mAh g^{-1} up to 50 cycles[154]. Wu group further demonstrated the importance of structural design in terms of improving the performances. They prepared nanoribbons of $K_2Ti_4O_9$ by oxidising and alkalising Ti_3C_2 MXene with KOH_{aq}[151]. The open microporous structure along with the nanosized thickness (<11 nm) and width (<60 nm) of these nanoribbons contributed to the improvement in ion kinetics. As a result, it delivered high capacities of 151 and 88 mAh g^{-1} at 50 and 300 mA g^{-1}, respectively, and was able to cycle over 900 times at 200 mA g^{-1}. By coupling potassium titanates with reduced graphene to form 2D heterostructure material, a reversible capacity of ~75 mAh g^{-1} at 2 A g^{-1} for over 700 cycles was demonstrated by Zheng *et al*[152]. Although, having large interlayer spacing, these titanates still suffered from the strain induced by K^+ ions when cycling in and out due to the large solvation structures around the K^+ ions in organic solvents[213]. An attempt by Reeves *et al* to prepare a titanate with even larger interlayer spacing (>1 nm), lepidocrocite-type layered titanates, further support this claim[150] with a reversible capacity of less than 50 mAh g^{-1} at 25 mA g^{-1}. While LTO serves as a zero-strain anode for LIBs, the same behaviour was yet to be discovered for potassium titanates reported in KIBs. Nevertheless, I and Wang *et al* reported a manganese fluoride based zero-strain (Figure 2-19a) $K_{0.6}MnF_{2.7}$ nanocubes (KMnF-LE) for KIBs[214]. Vacancies created by potassium and fluorine deficiency served as storage sites for K^+ ions. As a result, KMnF-LE delivered a reversible capacity of 110 mAh g^{-1} at 400 mA g^{-1} for an impressive 10,000 cycles.

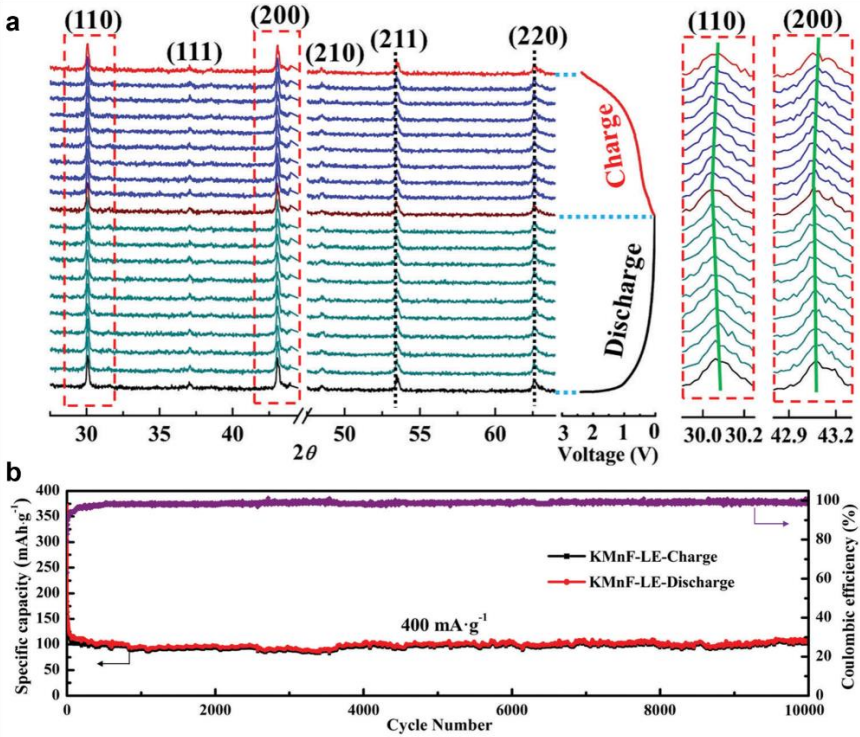

Figure 2-19 – Electrochemical performance of $K_{0.6}MnF_{2.7}$. **a**, *In situ* XRD analysis collected in the first discharge-charge cycle. Diffraction peak (110) shifted 0.05° during intercalation corresponding to changes in interlayer spacing and volume of 0.2% and 0.5%, respectively. **b**, Long cycle at 400 mA g^{-1} for 10,000 cycles[214].

Similar to lithium, elemental potassium is able to form alloys with various elements, including tin, antimony and bismuth. Being able to provide higher capacities via multiple reactions with potassium per atom, alloying anodes present some advantages as compared to intercalating anodes[18,215]. The inevitable huge volume expansion will, however, be one of the greatest challenge[216]. Glushenkov *et al*[217] (Figure 2-20a) and Huang *et al*[218] (Figure 2-20b) both tried to solve this problem by using a general strategy:

mixing tin with carbon materials. As a result, Glushenkov *et al* improved the reversible capacity of pure tin from near 0 to 100 mAh g^{-1} at 25 mA g^{-1} after 100 cycles; and Huang *et al* demonstrated a high reversible capacity of ~276 mAh g^{-1} at 50 mA g^{-1} for 100 cycles. Similar strategies were applied to antimony. Zheng *et al* encapsulated antimony nanoparticles inside a carbon sphere network (Sb@CSN)[219] (Figure 2-20c). The full intercalated K_3Sb has a theoretical specific capacity of 660 mAh g^{-1} and Sb@CSN delivered 83% and 76% of the theoretical capacity at 100 and 200 mA g^{-1} for 100 and 220 cycles, respectively. Liu *et al* also demonstrated graphene encapsulating antimony nanoparticles (Figure 2-20d) with a reversible capacity of 474 mAh g^{-1} at 100 mA g^{-1} over 800 cycles[220]. Li group reported that bismuth will gradually self-assembled into a 3D porous structure when interacting with dimethoxyethane (DME) molecules after three--two-phase reactions Bi ↔ KBi_2 ↔ K_3Bi_2 ↔ K_3Bi[221]. They, therefore, assembled a full cell using bismuth as anode and PB as cathode. An energy density of ~108 Wh kg^{-1} was maintained after 350 cycles with an operation voltage of 2.8 V.

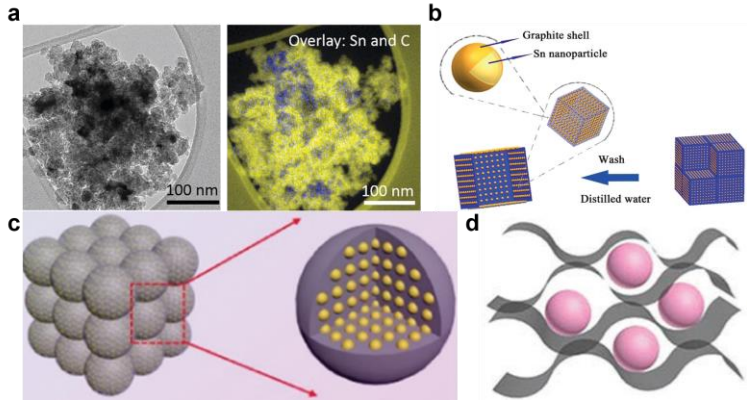

Figure 2-20 – Structures for different Sn/Sb-C composite anodes. **a,** Tin-graphite anodes mixed with ball milling[217]. **b,** Uniformly distributed tin nanoparticles encapsulated with graphite[218]. **c,** Sb@CSN prepared by electrospraying[222]. **d,** Antimony nanoparticles within graphene framewroks[223].

Conversion anodes in KIBs are plagued with volume expansion the same way alloying anodes are. Carbon-mixing techniques are, therefore, essential while designing

conversion electrodes[163]. Rahman group mixed Co_3O_4-Fe_2O_3 nanoparticles with super P carbon black at a weight ratio of 2:1 [224]. The result of the dual conversion reactions between potassium and Co_3O_4 and Fe_2O_3 showed a reversible capacity of 220 mAh g^{-1} at 50 mA g^{-1}. Apart from simple ball mill mixing, different carbon-mixing techniques were investigated. I and Yu *et al* used solvothermal to incorporate metallic $CoSe_2$ into flexible nitrogen doped carbon nanotubes[225] and achieved a reversible capacity of 173 mAh g^{-1} at a high current density of 2 A g^{-1} over 600 cycles. The electronic conducting nature of both $CoSe_2$ and carbon nanotubes accelerated the electron transfer and enhanced the rate and cycle performances. Wang *et al* prepared $MoSe_2$ in pistachio shuck like carbon shell using solid-state carbonisation[226]. This unique morphology (Figure 2-21a) gave the material a high packing density, as a result, it delivered a reversible capacity of 322 mAh g^{-1} at 200 mA g^{-1} for 100 cycles and 226 mAh g^{-1} at 1 A g^{-1} for 1,000 cycles. Liu *et al* sandwiched few-layered Sb_2S_3 within carbon sheets via high-shear exfoliation[227]. Sb_2S_3 underwent an intercalation reaction followed by conversion and alloying reactions (Equation 2-13 to Equation 2-15) to store potassium.

$$Sb_2S_3 + xK^+ + xe^- \rightarrow K_xSb_2S_3 \quad \text{Equation 2-13}$$

$$K_xSb_2S_3 + 2xK^+ + 2xe^- \rightarrow 2Sb + 3K_xS \quad \text{Equation 2-14}$$

$$2Sb + 3K_xS + (8-3x)K^+ + (8-3x)e^- \rightarrow 2K_3Sb + K_2S_3 \quad \text{Equation 2-15}$$

Irreversible sulfur by-product would be formed during these reactions and treated as a loss of active material. The carbon sheets not only suppressed the volume expansion but also traps those sulfur by-products. Wei *et al* vertically grew MoS_2 onto graphene sheets with large layer spacing via a two-step solvothermal reactions[146]. Like Sb_2S_3, the potassium storing process contained two mechanisms: intercalation and conversion (Equation 2-16 and Equation 2-17).

$$MoS_2 + xK^+ + xe^- \rightarrow K_xMoS_2 \quad \text{Equation 2-16}$$

$$K_xMoS_2 + (4-x)K^+ + (4-x)e^- \rightarrow Mo + 2K_2S \quad \text{Equation 2-17}$$

The unique morphology (Figure 2-21b) and the chemical bonds between MoS_2 and graphene led to an initial discharge capacity of 679 mAh g^{-1} at 20 mA g^{-1}. There were

many other methods employed to incorporate different conversion anodes with various forms of carbon[210,228–233].

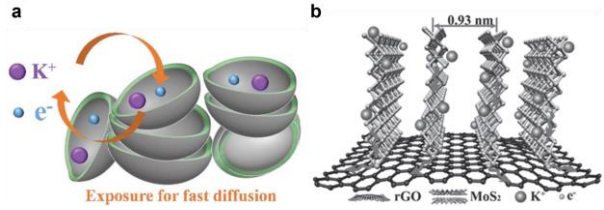

Figure 2-21 – Morphologies of **a**, $MoSe_2$-pistachio shuck like carbon[226] and **b**, MoS_2-graphene[146].

Regardless of the size difference between Li^+ and K^+ ions, the electrode materials reported for both LIBs and KIBs are very much alike[11,18,163]. The development for KIBs if not all but mostly followed the progression path of LIBs. This trend may misguide research to the wrong direction. A different storing mechanism, other than intercalation, alloying nor conversion should be designed specifically for K^+ ions storage simply due to the size differences between cations.

§ 2.2.3. Potassium-sulfur batteries

There are only and a handful of research reports on KSBs. They share similar cell configuration with LSBs, a sulfur cathode against a potassium metal anode with a polymer separator[89–93]. Zhao *et al* used CMK-3 as sulfur host for KSBs[89] and achieved an initial capacity of ~510 mAh g^{-1}. This value was not even a half of what was achieved for LSBs with CMK-3 cathode (1,320 mAh g^{-1})[95]. This may be owing to the major product of this KSBs being K_2S_3 instead of K_2S (analogues to Li_2S in LSBs). Xiong *et al*, however, suggested the major product is K_2S[93] and achieved an initial capacity of ~1,200 mAh g^{-1}. Nevertheless, this is still debatable since Hwang *et al* suggested both K_2S_3 and K_2S as the discharged product in two separate publications[91,92]. Many fundamental questions are yet to be answered for KSBs. This PhD project would study and attempt to solve the most prominent issues in LSBs and KIBs as a groundwork for future KSBs research.

Chapter 3

Methods

§ 3.1. Electrospinning technique

Simple and straightforward as it is, electrospinning is a highly versatile technique to generate 1D nanostructures with a variety of materials. The precursor, a viscoelastic solution is drawn by electrostatic force for continuous uniaxial elongation to form nanofibres. The contactless arrangement and continuous process allow high volume production of high purity ultrathin fibres[234–237].

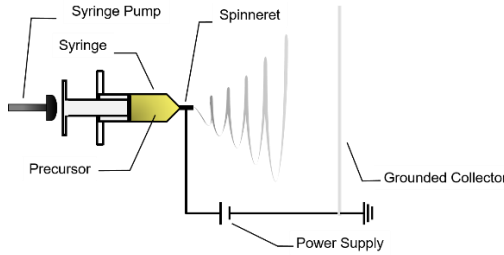

Figure 3-1 – Schematic illustration of a typical electrospinning set-up.

Electrospinning can produce nanofibres from a variety of viscoelastic solutions including, but not limited to polymer solutions, sol-gels, emulsions and liquid crystals. The precursor is hosted in a syringe and fed into the spinneret at a controlled feeding rate with high voltage (5 to 30 kV) applied to the tip. The spinneret serves as an electrode and the grounded collector usually distanced at 10 to 25 cm away serves as the counter electrode. An electric field of strength ~100 kV m^{-1} stretches the solution as it ejects from the spinneret. A self-organised woven mat of solid nanofibres is expected

to form at the collector under the perquisite of effective solvent evaporation as the jet travels through the atmosphere[235,236].

Without any applied potential, droplets are formed by the confinement of surface tension as the polymer solution emerges at the tip of the spinneret. When a voltage is applied, the positive charges built on the surface of a droplet form a direct competing electrostatic force against surface tension. A stable spherical shape is maintained when the potential applied is below the threshold. At the same time, the Coulombic force imposed by the external electric field tends to pull the droplet toward the counter electrode. A droplet can be deformed and elongated into a cone-shaped distortion, commonly known as Talyor cone, once the electrostatic force and the Coulombic force achieves a balance with the surface tension. If the Coulombic force surpassed a supercritical electric field strength, an electrified liquid jet would eject from the stable Talyor cone towards the counter electrode since the equilibrium can no longer be sustained. With further stretching, narrowing and solidifying, solid fibres with diameters from a tenth of nanometres to several micrometres can arrive on the grounded collector with high velocities[234,235].

As aforementioned, versatility is one of the most practical advantages in electrospinning. Through manipulation of equipment set-ups and experimental parameters, different levels of structural control can be achieved with electrospinning. For example, different forms of rotating collector have been used to yarn aligned fibres. Matthews's group pioneered in using mechanical rotating shear force to align the fibres with a rotating drum[238]. Nevertheless, the difficulties in matching the rotating speed and electrospun rate for high-quality continuous yarn hindered the practicality of the method[238]. Other attempts to control fibre orientation have been discussed by different groups in the past decades. Teo and co-workers placed knife-edged auxiliary electrodes under or inside the rotating drum collector as guidance to limit electrospun fibres collection path as effective methods for highly aligned fibres[239]. Sundaray and co-workers obtained cross-bar patterned fibres by replacing knife-edged auxiliary electrodes to a sharp pin inside a lateral-moving rotating collector[240].

Apart from designing dynamic collectors, some researchers have manipulated the uniform external electric field with different types of static collectors in an attempt to

control the jet distribution path. Li and Xia created aligned arrays and patterned fibres by placing patterned conductive collectors on insulating substrates[241,242]. The authors placed two parallel pieces of conducting metal with a gap in between (from hundreds of micrometres to several centimetres). The charged nanofibres were stretched across the gap and formed uniaxial aligned arrays perpendicular to the collectors as driven by electrostatic interactions[241]. They further arranged conductive collectors into different configurations[242]. The pattern tested was based upon a four-electrode cross shaped configuration and a six-electrode in a circle shape at 60° apart from each other as shown in Figure 3-2a and b. Magnetic controlled electrospinning process was another attempt tried by researchers. Yang and co-workers demonstrated this idea by incorporating magnetic Fe_3O_4 into the solutions[243]. The authors then applied a magnetic field during the electrospinning process (Figure 3-2e). As a result, the magnetised electrospun fibres formed parallel arrays along the magnetic field lines.

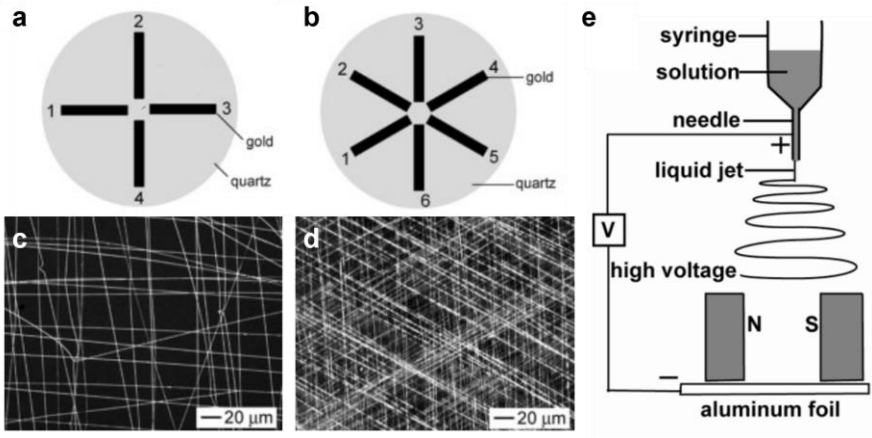

Figure 3-2 – Schematic illustrations of **a,** Four-electrode pattern and **b,** Six-electrode pattern. Optical images of fibres collected from **c,** Four-electrode pattern and **d,** Six-electrode pattern. **e,** Schematic illustration for magnetic electrospinning.

In addition to equipment set-ups, experimental parameters including operational settings and properties of the precursor are both means of controlling the fibre morphology[244,245]. One of the main controlling parameters for fibre diameter is the

electric field strength. Within an optimal range, fibre diameter decreases as electric field strength increases (applied voltage increases or collection distance decreases). Although decreasing the distance between electrodes have the same effect as increasing applied potential, upon shortening the distance, inadequate drying of solvents may lead to the formation of spherical droplets[245].

Chemical modification to a large extent is the most versatile route that provides the flexibility to design nanofibre morphology. In a typical electrospinning precursor for ceramic materials, the main components are the solvent, polymer and metal salts. The viscoelastic characters and electrical conductivity of the precursor along with interplay among chemicals determine the behaviour of the jet thus the morphology[236]. Although general rules of parameters can be summarised when it comes to controlling nanofibre morphology, the complexity of chemical interactions may bring out very different results for each solution system. The role of the polymer is to increase the viscosity to an optimal value, alter the surface tension of the solution and therefore control the viscoelastic behaviour as well as the electro-spinnability. If the viscosity of the solution is too low, surface tension tends to convert liquid jet into droplets instead of fibres[236]. However, fibres are not electro-spinnable if the viscosity is too high due to uncontrollable ejection rate. In between these two extremes, there is a window of optimal value. Within this range, fibre diameter tends to increase with the higher concentration of the same polymer or larger molecular weight of different polymers[244]. The presence of metal salts in the solution have effects on the charge density in the solution which affects the fibre diameter distribution. With higher conductivity, the jet is subjected to more severe stretching by the extra tensile stress exerted by an electric field. Therefore, the fibres tend to be narrower[246]. On the other hand, the value of the diameters tend to spread along with a wide distribution due to rapid bending instabilities[247]. More stable fibres can be electrospun with semiconducting or insulating liquid.

Generally, fibres prepared by electrospinning have a solid core and a smooth surface. Nevertheless, secondary architectures such as porous, core-shell and hollow structures can be prepared with appropriate experimental parameters or through appropriate gadgets employed in the process. A porous structure can be introduced onto the fibre

surface with several methods. Both humidity and temperature affect the surface roughness of the electrospun nanofibres surface by manipulating solvent evaporation rate and moisture content in the atmosphere. It has been suggested that pores are formed by the condensation of moisture on the liquid jet during solidification[248]. The selection of solvents can be crucial as well in terms of controlling the porosity. The volatility of the solvent greatly influences the evaporation rate as the jet travels through the atmosphere before reaching the collector. Higher density of pores can be created with more volatile solvents. Furthermore, with sufficient phase separation between solvents and the solid fibres, high porosity if desired can be achieved[249]. Secondary core-shell structure can be achieved by co-electrospinning two immiscible solutions through implementing of co-axial spinneret[250,251]. With similar methods but a sacrificial core, the hollow structure can be obtained through selective removal of phases[252].

In this dissertation, a simple flat grounded collector with optimised operational and chemical parameters was used to obtain the best possible nanofibres.

§ 3.2. Materials characterisation

§ 3.2.1. Scanning electron microscopy

Scanning electron microscope (SEM) is an imaging technique for high-resolution surface topography, phase composition as well as the elemental information. With a spatial resolution of 10 nm, SEM can provide images with magnification up to 1,000,000 times depending on the nature of the sample. The large depth of field gives rise to 3D imaging.

In a high performing SEM, electrons are generated by a field emission gun located at the top of the microscope. The electrons are usually accelerated at an energy of 5 to 20 keV through vacuum environment towards the sample. A set of lenses, apertures and scanning coils are applied to guide and focus the electron beam to the designated spot on the sample surface. The interactions between the electron beam and the sample will generate a series of signals from the specimen. Among those, the three main signals are secondary electrons (SEs), backscattered electrons (BSEs) and characteristic x-rays.

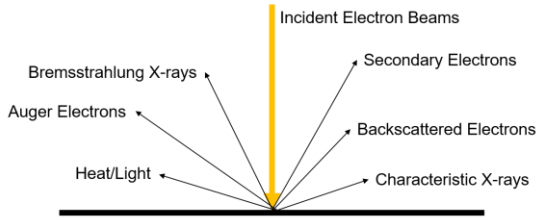

Figure 3-3 – Schematic illustration of signals generated in SEM.

SEs are the weakly bounded electrons being knocked out of their shell by high-energy electrons. These electrons are low-energy electrons escape from the areas close to the specimen surface. Therefore, they are mainly used for visualising the morphological properties of the sample surface. In contrast to SEs, BSEs are high-energy electrons escaped back out of the surface after multiple elastic and inelastic scatter interactions with the atomic nucleus of the specimen. They carry both compositional and topographic information. X-rays are generated when an electron from an outer shell filled in the vacancy left by a knocked-out inner shell electron. The excess energy (energy difference between the outer shell and inner shell) is emitted as characteristic x-ray, which can be used to identify the chemical information.

Samples with poor conductivity were coated with gold with EMITECH *550* before analysing. 10 mA for 40 seconds.

FEI Nova NanoSEM was used in this dissertation for high-resolution image and elemental mapping.

§ 3.2.2. Transmission electron microscopy

Similar to SEM, transmission electron microscope (TEM) utilises the energy-intense electron beam generated by field emission gun. The main difference between the two is how the electrons interact with the sample. In a TEM, the monochromatic electron beam passes straight through the sample. This technique requires ultrathin (nanoscale) sample and additional lenses placed below the sample to magnify and project sample image onto the camera. The high-energy electrons (usually 200 keV) in TEM facilitate atomic scale image resolution.

Both images and diffraction pattern formed by the TEM technique exploit parallel electron beam passing through the specimen. In general, a diffraction pattern should first be analysed before setting the microscope for imaging. Diffraction pattern for crystallography analysis is obtained in diffraction mode by using a selected area electron diffraction (SAED) aperture. By replacing the SAED aperture with an objective aperture, the TEM is engaged in imaging mode. It can be in either bright field or dark field imaging depending on whether it is the un-diffracted or diffracted electron beam passing through the specimen.

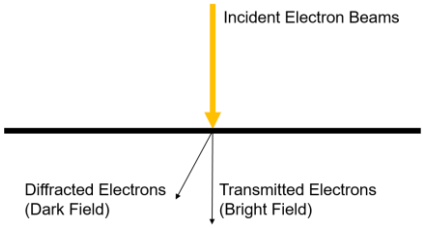

Figure 3-4 – Schematic illustration of electron beam-sample interaction in TEM.

Different type of informative image contrast is utilised in TEM for various applications. This includes mass-thickness and diffraction contrasts which are observed in bright field and dark field imaging, respectively. As suggested by the term itself, mass-thickness contrasts arise because of non-uniform sample density or thickness. Given a uniform thickness, the parts formed by heavier atoms appear darker than that contained lighter atoms due to stronger interactions between electrons and atoms. In a single element sample, thinner areas appear lighter because of less electron scattering events. The compositional information provided by diffraction contrast arises because of the difference in crystallinity. The crystalline area in the specimen appears darker due to stronger scattering, *vice versa* for the amorphous area.

Samples were grinded into powders and suspended within ethanol. The suspensions were then ultra-sonicated to ensure thin layers of the sample.

FEI Tecnai Osiris operated by Dr Giorgio Divitini was used in this dissertation.

§ 3.2.3. Energy-dispersive x-ray spectroscopy

Energy-dispersive x-ray spectroscopy (EDS) utilise the characteristic x-rays generated in both SEM and TEM. The x-rays carrying elemental information are emitted isotropically as the electron beam scan through the sample surface. Elemental mapping can thus be plotted on to the monitor. By colour coding different elements, distribution and the variations in the concentration of several target elements can be obtained. In the TEM, EDS requires high spatial resolution and is performed with a convergent electron beam in scanning transmission electron microscope (STEM) mode.

§ 3.2.4. X-ray photoelectron spectroscopy

X-ray photoelectron spectroscopy (XPS) is a quantitative surface-sensitive spectroscopic chemical analysis technique with an average depth of analysis around 5 nm. It is used to quantify the chemical state information in the surface region over a wide range of materials. In a typical XPS, the sample surface is energetically excited by illuminating energetic mono x-rays which emits photoelectron signals from the first ~20 atomic layers of the sample that are being further analysed to measure their energy. The binding energy and the intensity of those photoelectron peaks in the XPS spectrum provide quantitative information of the constituent elements, the valence state of the chemicals and the quantity of the detected elements.

§ 2.2.5. Powder x-ray diffraction

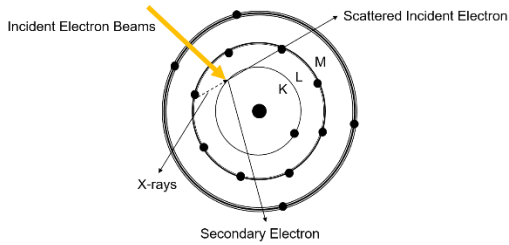

Figure 3-5 – Schematic illustration of x-ray generation.

Powder x-ray diffraction (XRD) is a common technique to acquire crystallography information by using x-ray on homogenised and finely grounded material. The x-rays

are generated by hitting a target with high voltage accelerated electrons inside a vacuum cathode ray tube in the same principle as in SEM and TEM. They are then filtered to produce a monochromatic beam and collimated directly toward the sample. Rotating the sample and scanning through a range of 2θ angles, the strongly diffracted incident radiation by crystal lattice in the specimen produces detectable constructive interference that satisfies the condition of Bragg's Law (see below) in all possible directions.

$$n\lambda = 2dsin\theta$$ Equation 3-1

Where n is an integer given by maximum order. This equation relates the wavelength, λ, of the x-ray with the lattice spacing, d, and the incident angle between x-ray and atomic plane, θ.

The number of diffracted x-ray photon reaches the detector will be processed, counted and plotted against incident angle. The diffraction pattern provides a structural fingerprint by which crystalline phases can be identified. In a mixture where multiple phases coexist; each phase will have their unique diffraction pattern independent from other. Apart from phase identification, degree of crystallinity can be determined by the shape of the patterns, lattice parameters can be given by conversion of peak position to d-spacings and particle sizes can be calculated with Scherrer equation.

Samples were grinded into powders by mortar and pestle.

Bruker D8 and D8 Advance were used in this dissertation.

§ 3.2.6. Raman spectrometry

Raman spectroscopy relies on inelastic scattering of monochromatic light (e.g. laser) after interaction with molecule, phonons or other excitations in the sample. It is a common surface spectroscopic technique used to identify substances through characteristic patterns in low-frequency vibrations: rotation, bending and wagging modes.

Generally, a laser beam illuminates the specimen and produced radiation from the illuminated spot. The incident photons from a laser source can be absorbed by the sample resulting in a shift in the energy of the incident photons that give rise to the information of vibrational mode and is further detected by Raman spectroscopy. The

incident photons can also be scattered upon interaction with the sample and give rise to information related to chemical structure and physical phases.

Samples were scanned using laser with energy of 0.5 mW.

Ramascope-1000 and RL633 laser source were used in this dissertation.

§ 3.2.7. Thermogravimetric analysis

Thermogravimetric analysis (TGA) is a thermal analysis technique that measures the mass of a sample while subjected to a programmed heat treatment under a controlled environment. It requires an inert sample pan (e.g. platinum or aluminium oxide), a precision microbalance, an accurate and programmable furnace and a controlled environment. TGA can be used to analyse the mass change during the test, which gives rise to an understating of the phase change, degradation/decomposition mechanism, oxidation reactions and other chemical reactions that may occur in the system during the heat treatment. It can also be used to investigate the thermal stability under different gaseous atmosphere.

Samples were grinded into powders. 5 to 10 mg of sample was used for each measurement.

TGA Q500 instrument was used in this dissertation.

§ 3.2.8. Gas adsorption and textural characterisation

Gas adsorption analysis is widely used to determine the surface area and porosity of a given solid material. Nitrogen gas (N_2) is one of the most common types of adsorbate gas used to probe the samples. Other inert gas can be krypton (Kr) or carbon dioxide (CO_2). After degassing contaminants from the sample surface, the samples are cooled to 77 K (boiling point of N_2) under vacuum. During the physisorption measurement, several dosages of N_2 are purged into the analysis tube to fill the pores along with an increase in pressure. From the gas volume uptake needed to form a monolayer of N_2 molecule on the surface, the specific surface area can be calculated. Furthermore, an isotherm curve can be generated by relating the adsorbed gas quantity with the relative pressure, a ratio of equilibrium (P_o) and the saturation pressure (P) at constant temperature (77 K).

5 to 10 mg of sample was used for each measurement.

Micrometrics TriStar instrument was used in this dissertation.

§ 3.2.9. Electron paramagnetic resonance

Electron paramagnetic resonance (EPR) is used to detect the presence of unpaired electrons, such as free radicals and defects, in a material. EPR detects unpaired electron transitions with an applied magnetic field. Under the influence of this magnetic field, electron "spin" may either orient in the same or opposite direction in respect of the external magnetic field. Lower and upper energy levels are created when the electron orients in the same and opposite direction, respectively. By supplying a fixed frequency microwave while sweeping the applied magnetic field, we can excite the electrons in the lower energy level to the upper energy level at a specific magnetic field strength that create a resonance for the defects or free radicals. The sweeping event is recorded.

10 mg of sample was used for each measurement.

JES-FA200 ESR spectrometer was used in this dissertation.

§ 3.3. Electrochemical analysis

LSBs, KIBs and NIBs are studied in this work using several electrochemistry testing techniques that includes the following.

Cyclic voltammetry (CV), galvanostatic discharge-charge curve, cycle life, cycling stability, capacity retention, Coulombic efficiency and specific capacity were used to evaluate the electrochemical performances of the cells tested in this dissertation.

CV is an electrochemical method for measuring the current response to an excess voltage applied in an electrochemical cell. It is performed by applying a potential (V) to the working electrode for a linear scan of V vs. time across a certain range of potential and recording the current (I) that develops as a function of applied potential. The measurements were taken with a two-electrode system, where working electrode potential is measured against a fixed potential at the reference electrode which also acted as the counter electrode. The resultant current which reflects reaction kinetics at the electrode is determined by mass and electron concentration profile at the electrode

surface. Various electrochemical information can be revealed by further investigating the collected data, including the reduction potential of the analyte, redox reaction reversibility, presence of intermediate and diffusion coefficient of the analyte.

Galvanostatic discharge-charge measurement is a technique used to characterise the capacity of the electrochemical cell by measuring the potential response by forcing the system with a constant current (C) rate. The discharge-charge curve varies with different C rate. At higher rates, stronger polarisation (Faradic current induced kinetic deviation from equilibrium) occurs between electrodes and electrolytes and isolates the electrodes from electrolytes. The unfavourable side effects lead to rapid potential drops and thus low capacity.

Cycling stability and cycle life are two important factors to determine the overall performance of the cell. The capacity at the end of each discharging cycle is recorded to plot the cycling stability curve. The total number of discharge-charge cycles survived is stated as the cycle life. The capacity retention rate (fraction of final capacity to initial capacity) at the end of cycle life is regarded as an important indicator for cyclability. Specific capacity is calculated by dividing the capacity over active material mass. Coulombic efficiencies throughout the cycles are measured by dividing the charged capacity over discharged capacity.

Chapter 4

Flexible Carbon Nanofibre Interlayer with Highly Mounted TiO_2 Polysulfide Anchors for Lithium – Sulfur Batteries

The development of lithium-sulfur batteries (LSBs) is impeded by the polysulfide dissolution and diffusion in organic electrolytes that leads to gradual failure of the cell[13–16]. To address this, a flexible carbon nanofibre interlayer with high-loading (78 wt%) TiO_2 nanoparticles (TiO_2-CNF interlayer) is prepared. TiO_2 nanoparticles are *in situ* grown from the core to the surface of the conductive carbon nanofibre with a size gradient and serve as anchors to chemically adsorb polysulfides. The CNF backbone physically adsorbs polysulfides at the same time and provides reactivation and re-utilisation sites to allow the polysulfides to be reused. Furthermore, CNF act as a buffer to accommodate the huge volume expansion and a rigid framework for holding TiO_2 nanoparticles.

Due to the combined effects of TiO_2 and CNF, significant improvements regarding capacity, cycle stability and rate capability is demonstrated when coupling TiO_2-CNF interlayer with a multi-walled carbon nanotube-sulfur cathode (MWCNT-S) as compared to pure MWCNT-S cathode. It shows, the TiO_2-CNF interlayer increased initial discharge capacity by 46%, prolonged the cycle life with 25% more capacity retention at the end of 300 cycles and improved the average Coulombic efficiency by 5%. The design and synthesis of flexible hybrid interlayers by *in situ* integrating metal oxides with carbon nanofibers offer a breakthrough to advance LSBs for practical applications in the future.

Parts of the findings are reported in:

Teng Zhao†, Yusheng Ye†, **Cheng-Yen Lao†**, Giorgio Divitini, Paul R Coxon, Xiaoyu Peng, Xiong He, Hyun-Kyung Kim, Kai Xi, Caterina Ducati, Renjie Chen*, Yingjun Liu*, Seeram Ramakrishna, R. Vasant Kumar*. A praline-like flexible interlayer with highly mounted polysulfide anchors for lithium–sulfur batteries. *Small* **13**, 1700357–1700363 (2017).

*Corresponding authors.

†These authors contributed equally.

T.Z., C-Y.L., Y.L. and R.V.K. conceptualised the study and wrote the manuscript. C-Y.L. performed the experiments. T.Z. and C-Y.L. analysed and interpreted data. R.C. coordinated and Y.Y. performed the electrochemical testing and the theoretical computations. C.D. supervised and G.D. and X.P. contributed to the TEM acquisition. P.R.C., H-K.K. and K.X. provided insights. All authors contributed to the overall discussions and edited the manuscript.

§ 4.1. Introduction

In the past decade, the role of metal oxides either as additives or sulfur hosts in cathode has been extensively researched[110–113]. However, only a handful of research has utilised metal oxides as interlayer materials. One of the main reasons attributing to the absence of such studies is related to their intrinsic mechanical properties. Even though metal oxides preserve high strength, these materials only absorb limited energy prior fracture and therefore brittle in nature. The brittleness presents an immediate challenge to fabricate free-standing flexible film, a factor essential for interlayer design[14,120].

Preparing metal oxides within the nanosized range is one of the most effect methods to prevent pulverisation of metal oxide interlayers[44]. In one of our group's work, ZnO nanowires were grown onto carbon nanofibre mat as the interlayer[131]. This design, however, has one major issue: the diffusion path for the chemically adsorbed polysulfides on the surface of ZnO to the re-utilisation carbon site is far. This significantly reduced re-utilisation efficiency. If chemical polysulfide anchors can be brought locally near the carbon, the re-utilisation rate may be improved.

To achieve this, the electrospinning technique followed by calcination-pyrolysis as a method to nano structural design flexible hybrid interlayers made from oxide nanoparticles and porous carbon. During the electrospinning stage, titanium source was buried inside polymer nanofibres. TiO_2 crystals nucleate and grow from the oxide precursor by calcination process, while the polymer is being carbonised by pyrolysis at elevated temperature under constant nitrogen gas flow. By adjusting the amount of polymer, the flexibility of the composite and weight percentage of TiO_2 can be controlled and an optimal polymer content was determined to achieve flexible TiO_2-CNF interlayer. Combining SEM and electrochemical performance, the active material loss under battery cycling was effectively minimised with the implementation of a hybrid interlayer.

§ 4.2. Materials synthesis and characterisation

§ 4.2.1. Electrospun TiO_2-CNF interlayer

A TiO_2-polyvinylpyrrolidone (PVP, Mw=1,300,000) electrospinning precursor was prepared by mixing TiO_2 sol with viscous PVP solution. The TiO_2 sol was prepared by adding 1 ml of titanium (IV) isopropoxide (TTIP) and 0.2 ml of acetylacetone into 5 ml of ethanol followed by 6 hours of gentle stirring under ambient condition. An additional 2 mL of 8M acetic acid was added into the solution. PVP solutions were prepared by dissolving 0.36g of PVP into 3.8 ml of ethanol followed by an 18-hour stirring to achieve homogenous PVP. After that, the two solutions were mixed with a 24-hour stirring to ensure PVP coating on TTIP.

The total electrospun precursor was 12 mL with a PVP concentration of 0.03 g ml^{-1}. The readily prepared TiO_2-PVP precursor was loaded into a syringe with a stainless steel 23-gauge flat-tip spinneret and ejected with a controlled rate of 1.25 ml hr^{-1}. The solution was subjected to an applied potential of 20 kV. As-spun, solid fibres were collected on a flat aluminium foil located 15 cm away from the tip of the spinneret. The humidity and the temperature of the electrospinning environment were kept at 25% and 23 °C. After 8 hours of electrospinning, the nanofibre mat was peeled off the aluminium foil and transferred into a tube furnace. The as-spun TiO_2-PVP nanofibre mats were subject to pyrolysis at 700, 800 and 900 °C under an N_2 atmosphere (gas

flow rate: 80 ml min^{-1}) for 3 hours with a ramp rate of 5 °C min^{-1} to remove solvents, form crystallise TiO_2 and carbonise PVP.

As briefly described above, TiO_2-CNF interlayers were prepared by a two-step process: electrospinning and pyrolysis. Morphological analysis and materials characterisation results of the as-spun fibres and the pyrolysed material will be discussed in the following sections.

The electrospinning precursor was the building block for the designated interlayer. Each chemical added to the solution played an essential role to prevent premature hydrolysis of TTIP as well as for uniformly distributing the titanium organo-compound. Acetylacetone worked as an effective surfactant while acetic acid was added in order to stabilise the sol and control TTIP hydrolysis rate[244]. PVP was selected due to good solubility in ethanol and high compatibility with TiO_2 sol and most importantly due to its large molecule weight, the viscosity of precursor is easily altered. PVP also served as the carbon source. During the electrospinning process, as the electrified TiO_2 sol travelled through the controlled atmosphere, two simultaneous processes resulted later formed the solid non-woven mat at the collector: 1.) effective evaporation of ethanol, acetic acid and acetylacetone and 2.) rapid hydrolysis of TTIP that formed TiO_2.

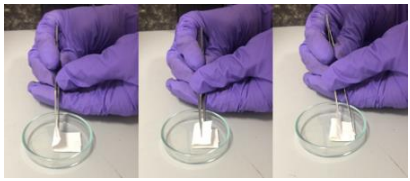

Figure 4-1 – Photographs demonstrating the appearance and flexibility of as-spun TiO_2-PVP.

The as-spun polymeric-oxide gel mats had a brush of yellow colour over the white base and exhibited high flexibility as shown in Figure 4-1. The microstructures of TiO_2-PVP mat is shown in Figure 4-2a. The highly-interconnected web composed of fibres with large aspect ratio with a diameter in the range of submicron and length from few micrometres to several centimetres. These nanofibres have an average diameter of 122 nm. There were no signs of TiO_2 nanoparticles under the SEM images as deducted from the smooth surface. This was consistent with Li and Xia's previous study as

amorphous TiO_2 particulates were embedded within the PVP fibre backbones[244]. The PVP matrix with uniformly distributed amorphous TiO_2 throughout the fibres became the blueprint for the *in situ* grain growth and integration of TiO_2 nanoparticles inside and outside the CNF framework during high-temperature treatment in a non-oxidising atmosphere.

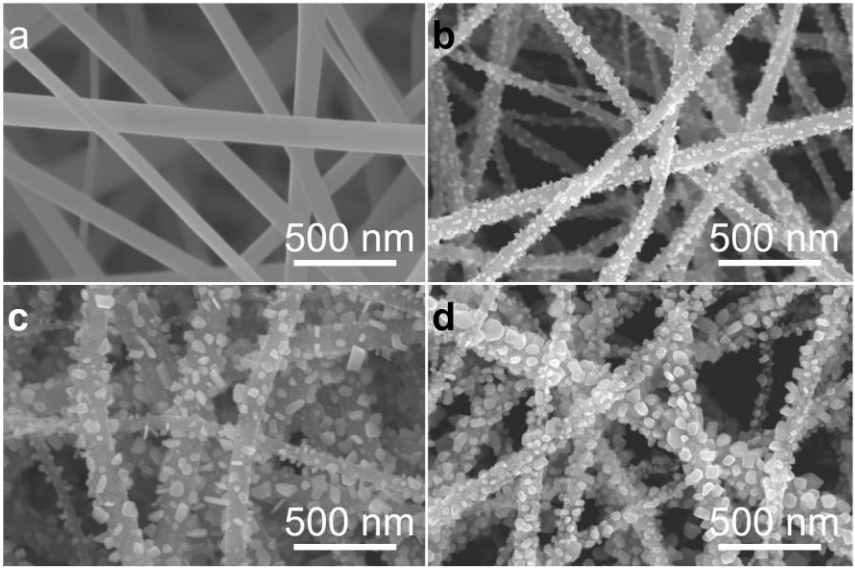

Figure 4-2 – SEM images for electrospun TiO_2-PVP and heat treated TiO_2-CNF composites at different temperatures. **a**, TiO_2-PVP. **b**, 700 °C. **c**, 800 °C. **d**, 900 °C.

The dramatic morphological change occurred after pyrolysis at elevated temperatures while retaining their fibrous structure as shown in Figure 4-2b-d. The hierarchical frameworks of all three samples were alike and can be described as the formation of CNF backbone with nanosized TiO_2 crystals protruding from the surface. The diameters were reduced due to PVP thermal decomposition and pore reduction during TiO_2 sintering[253]. As opposed to the similar average fibre diameter of 101, 102 and 100 nm; the particles showed an ascending trend in sizes, from 24 to 29 to 45 as the

temperature increased. This phenomenon implied that carbon blocks can act as structure-directing agents that controls the growth of TiO_2 particles[254].

TiO_2-CNF obtained at 800 °C was the only free-standing flexible TiO_2-CNF composite. With the mechanical stiffness provided by entangled CNF and the substantial amount of polysulfide anchor from TiO_2, it was a suitable chemi-/physisorptive interlayer material for advance LSBs. More detailed observations were made to examine the properties of the as-prepared TiO_2-CNF at 800 °C (referred to TiO_2-CNF interlayer from now on).

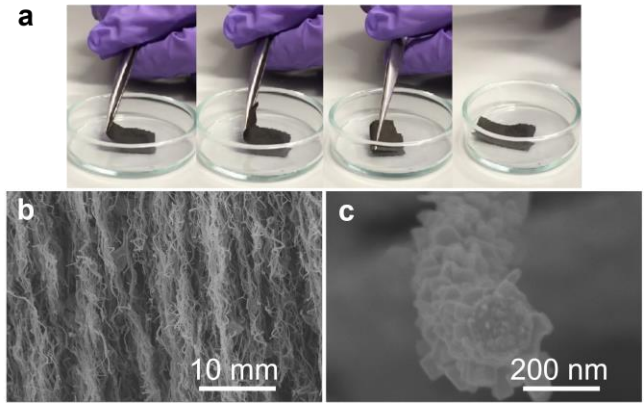

Figure 4-3 – Morphologies of TiO_2-CNF. **a**, Photographs demonstrating the appearance and flexibility of free-standing TiO_2-CNF. Cross-section SEM images of **b**, TiO_2-CNF mat and **c**, a single fibre.

The flexibility of the free-standing TiO_2-CNF interlayer was verified in a bending demonstration shown in Figure 4-3a. The springiness restoring force would elastically return the mat into its original flat configuration. With high TiO_2 loading of nearly 80 wt% (Figure 4-5b), it appeared to establish a combination of excellent mechanical properties compared to conventional brittle metal oxides, including stiffness (resistance to deformation), toughness (resistance to fracture) and pliability (response to bending or rolling). More SEM images taken from the cross-section of the film revealed its microstructure as well as its nanostructure. The hybrid material was

formed by layers of fibrous network and each fibre was decorated with polyhedral nanoparticles. The cross-section SEM image of a single fibre further revealed the embedded particulates are smaller than the ones on the surface distributed inside the CNFs. A size gradient for TiO_2 nanoparticles from less than 10 to 60 nm along the cross-section surface of the fibres was formed as expected. The unique electrospun 3D hierarchical felt implied a unique formation mechanism which was further investigated with TEM.

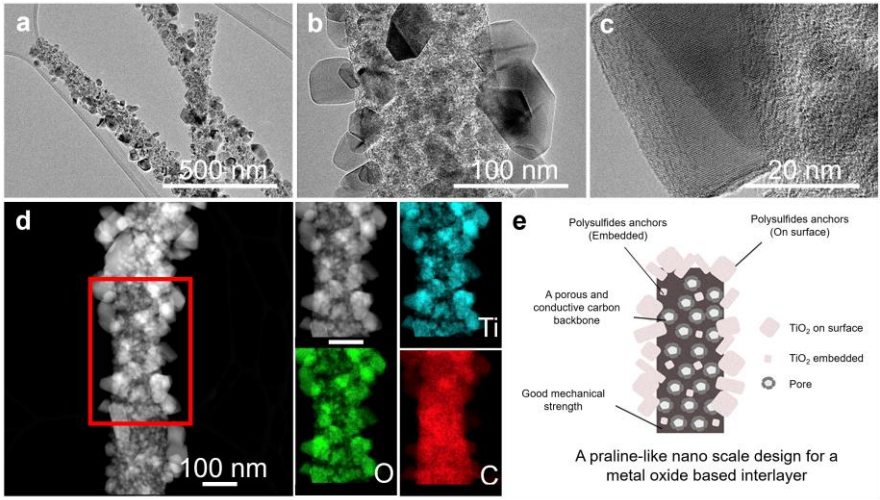

Figure 4-4 – Nanostructure of TiO_2-CNF. **a-c,** TEM images from low to high magnifications. **d,** STEM image and the corresponding elemental mappings. Cyan being Ti, green being O and red being C. The scale bar for all four is 100 nm. **e,** Schematic illustration.

From low to high magnifications, the TEM images revealed similar but additional findings in comparisons with images from the SEM study. Most of the particulates (average size ~58.2 nm) was anchored on the surface of the CNFs while smaller nanoparticles (<10 nm) were scattered inside the fibres. By studying the STEM images, the protruding nanoparticles were TiO_2 as confirmed by the elemental mapping where Ti and O were the main elements on the nanoparticles. Furthermore, a size gradient was clearly shown from the core of the carbon backbone, indicated in red colour, to the

surface. A lot of voids throughout carbon backbones were observed as well. These pores were created by PVP thermal decomposition as well as TiO_2 molecules reduction in size from localised sintering via mass transport.

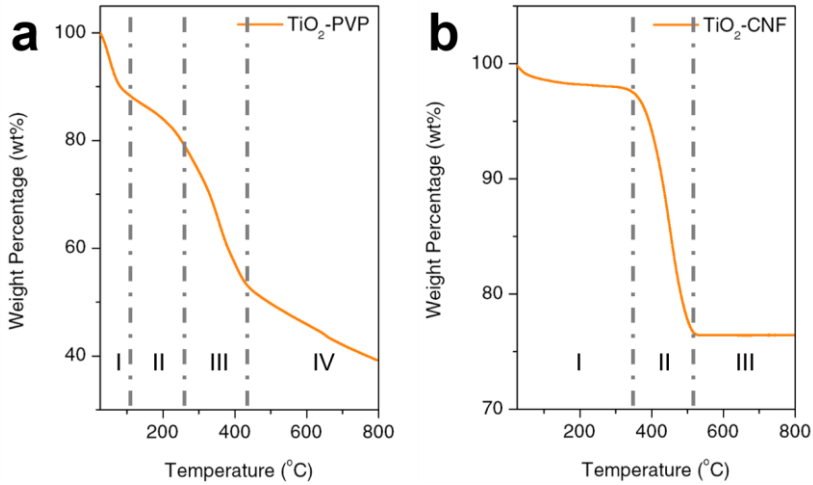

Figure 4-5 – TGA analyses. **a**, TiO_2-PVP and **b**, TiO_2-CNF. The analyses for was carried out **(a)** in N_2 and **(b)** in the air up to 800 °C at ramping rate 10 °C min^{-1}.

Further thermal analyses were carried out to investigate the compositions of TiO_2-PVP and TiO_2-CNF composites.

The results of TGA are presented in Figure 4-5. There are four thermal degradation steps of TiO_2-PVP composites as shown in Figure 4-5a. The first decomposition step between room temperature and 100 °C were the release of adsorbed water and trapped solvents. The second and third decomposition step covered the main temperature range between 100 and 420 °C for PVP decomposition where the side chain (pyrrolidone) broke off from the backbone through dehydration and sp^2 bond formed along the polymer backbone[255,256]. At the end of the third step, after continuous decomposition of PVP, amorphous CNFs were formed. The decomposition rate should be consistent in both stage II and III if the only reaction took place was PVP depolymerisation, nevertheless, the dramatic weight loss in the third step (from 250 °C)

suggested a second decomposition process. The temperature coincided with the beginning of TTIP decomposition[257,258]. This is taken as evidence for a proportion of un-hydrolysed TTIP to remain buried in the core of PVP fibres. In this step hydrocarbon molecules were released[258]. During the last step, TTIP continues to decompose into TiO_2 and further phase transformed from amorphous to anatase and eventually to rutile. At the same time, part of the carbonised PVP was combusted by the oxygen released during decomposition. The weight loss of ~40 wt% (excluding loss of moisture and solvent) in the sample during PVP decomposition temperature range shows PVP decomposition is the main cause for fibre diameter reduction. The carbon content in TiO_2-CNF composite was studied by TGA in air (Figure 4-5b). During the first step, moistures was released from the sample. Between 350 and 510 °C, a rapid drop in weight indicates carbon combustion. The carbon content was found to be 21.8 wt%.

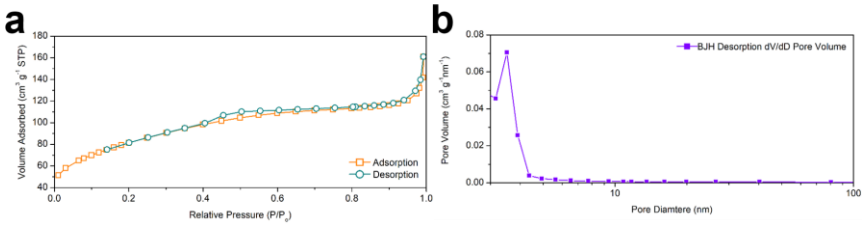

Figure 4-6 – Nitrogen adsorption-desorption analysis of TiO_2-CNF. **a**, isotherm and **b**, pore size distribution.

BET results showed the composite had a specific surface area at 289 $m^2\ g^{-1}$. The large specific surface area was attributed to the mesoporous carbon backbone as pure TiO_2 nanofibres only had a specific surface area roughly at 10 $m^2\ g^{-1}$. The adsorption-desorption curve indicated a Type IV isotherm. The small hysteresis suggested the composite had a mesoporous structure with a pore size (2.72 nm) close to micropores range (<2 nm)[259].

The formation mechanism behind this electrospun metal oxide-carbon composite was postulated in the following paragraph with thermal analyses and electron microscopy images as the basis for the theory. In the as-spun TiO_2-PVP composite, TiO_2 molecules

from hydrolysed TTIP were distributed uniformly throughout the PVP fibres with the majority of those located in the outer layers. The un-hydrolysed TTIP were mostly buried near the core of the PVP fibres. As the temperature went up, thermal decomposition and carbonisation of PVP started from the surface along with the thermal gradient imposed onto the matrix[260]. During PVP decomposition, pores were created. These pores allowed mass transport of TiO_2 molecules via surface and grain boundary migration. Therefore, during the early stage of carbonisation, TiO_2 molecules sintered and grew into nucleation sites for futher grain growth enriched at the surface to attract those small particulates buried inside the fibres. As the temperature continues to rise, the un-hydrolysed TTIP began to decompose into TiO_2 molecules at ~250 ^oC as suggested by the TGA analyses[257,258]. With sufficient driving force, the TiO_2 molecules migrated towards larger particles through the un-carbonised PVP matrix because of Ostwald ripening phenomenon. When the TiO_2 molecules stored inside the fibres reduced below a certain level, the buried TiO_2 molecules would lose their mobility to diffuse out since the immediate vicinity of TiO_2 attraction was too weak[261]. Thus, smaller and smaller particulates were left and formed near the core. On the contrary, the TiO_2 particles at the surface continued to agglomerate and sinter into larger particles to minimise surface energy. Eventually, the collaborative efforts of decomposition and molecule migration formed a hierarchical structure.

The results from SEM, TEM and STEM analyses confirmed an exceptional formation mechanism of the composite and a unique distribution of TiO_2 in the continuous CNFs felt, which was unprecedented in any previous report. It is worth stating that the mechanical strength of the structure since it remained intact after ultra-sonication during TEM sample preparation. The robust mechanical property and flexibility of the mat were proposed to be related to the size and volume content of TiO_2 particulates that were scattered within the CNFs[262]. The size of the particles are required to be small with no large TiO_2 nanoparticles that could break the inter-connection of carbon grains and/or block the twisting motion of graphitic carbon helped the mechanical stability of the structure. At the same time, the volume content cannot be high either for the same reason as with larger nanoparticles. On the other hand, the volume content cannot be too low as too many voids would be left behind, leading to fragile composites.

Crystallography information of the composite was obtained by XRD as shown in Figure 4-7a. The diffraction patterns closely matched to that of reported rutile phase (00-21-1276) suggesting a polycrystalline rutile phase throughout the sample. The lattice parameters calculated from the composite are a=4.58 Å and c=2.95 Å; the figures closely matched the reported values of a=4.59 Å and c=2.96 Å. Furthermore, the average size of the crystals was 27.7 nm as calculated by the Scherrer equation. Apart from the sharp peaks that matched the rutile phase, there was one broad peak at 26.6° which did not belong to the rutile structural fingerprint. The peak could be attributed to two very different materials: 1.) carbon materials presented in the composite or 2.) anatase phase from incomplete phase transformation. The grain size calculated was 5.8 nm. It would be very unlikely for the anatase phase to remain so small after heat treatment at elevated temperature. Therefore, more XRD analysis and Raman spectrometry were carried out.

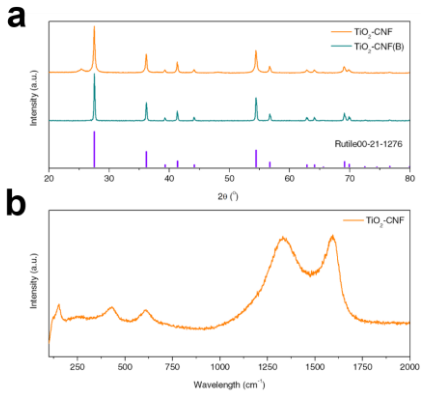

Figure 4-7 – **a**, XRD patterns for TiO_2-CNF and heat-treated 003T. **b**, Raman spectroscopy of 003TC.

TiO_2-CNF was heat treated to 800 °C in the air to burn off the carbon. The phase of the pure TiO_2 sample was analysed with XRD, denoted as TiO_2-CNF(B). All patterns remain the same as in Figure 4-7a, with one exception: the absence of a broad peak at 26.6°. This indicated that peak was attributed by the CNF in the hybrid material and

not unconverted anatase phase. Further information on the carbon was found from the Raman spectroscopy as shown in Figure 4-7b. In a typical partially graphitised carbon spectrum, there are D band at 1340 cm^{-1} and G band at 1600 cm^{-1}. D band represented disordered carbon atoms and defects in the matrix and G band originated from the in-plane vibration of sp^2 carbon atoms[101]. The size of graphitic carbon (La) is directly proportionate to the ratio between the area under the curve of D (I_D) and G (I_G) band with the empirical equation $La = 4.4(I_D/I_G)$ nm[263]. I_D/I_G was 1.27 for the composite. The corresponding graphitic carbon size is 5.6 nm and in agreement with the grain size (6.2 nm) obtained by the Scherrer equation from the XRD pattern. The existence of graphitic carbon suggested the composite would exhibit a certain level of electrical conductivity to assist electronic and ionic movements. The peaks at lower wavelengths (<750 cm^{-1}) were attributed to the rutile phase.

In summary, the electrospun TiO_2-CNF demonstrated three key features relevant to potential use as interlayer in Li-S batteries: 1.) extensive coverage of TiO_2 nanoparticles provided substantial amount of chemisorption anchor sites for polysulfides throughout the nanostructured framework, 2.) interconnected mesoporous conductive carbon backbone provided physisorption to host sulfide/polysulfide pores as re-utilisation sites, favoured electrolyte diffusion and facilitated fast electron movements and 3.) flexible and high strength interlayer to accommodate volume expansion upon lithiation-delithiation of sulfur species during re-utilisation process.

§ 4.2.2. Sulfur infiltrated MWCNT cathode

Sulfur was thermally infused into MWCNT (specific surface area 160-200 m^2 g^{-1}, diameter 10 to 30 nm, length >2 μm, purity >97%) to make core-shell structured MWCNT-S composite cathodes. MWCNT and S with weight ratio 3:7 was fully mixed and sealed in a polytetrafluoroethylene (PTFE) container under the protection of Ar gas followed by heat treatment at 155 °C for 24 hr to ensure full S infiltration into the interconnected MWCNT network. The S ratio was optimised for high energy density and sufficient electrical conductivity[95].

Having a high sulfur loading in the cathode was one main reason to incorporate interlayer into LSBs[119]. Herein an MWCNT-S cathode was chosen to pair with the TiO_2-CNF interlayer due to its capability of carrying large sulfur content, high electric and

ionic conductivity along its 1D path and mechanical strength. As previous research has demonstrated, that with 70% sulfur loading, MWCNT-S cathodes have limited capacity retention of 41.8% after 100 cycles[131]. This could be reasoned by their small specific surface area to accommodate sulfide/polysulfides and limited ability in trapping shuttling polysulfides. Therefore, it could be the most suitable platform to prove the functionality of incorporated interlayers in terms of mitigating the loss of active materials.

The interconnected fibrous morphology of the MWCNT-S mixture was revealed by SEM images. A uniform core-shell structure was achieved after sulfur infiltration. The MWCNT core served as the conductive backbone that provided a path for fast electron and ions movements in and out of the sulfur shell. The core-shell fibres had an average diameter of ~60 nm and length in the range of micrometres. The smooth surface and absence of sulfur agglomeration indicated intimate contact between sulfur and MWCNT due to the non-polar nature they shared.

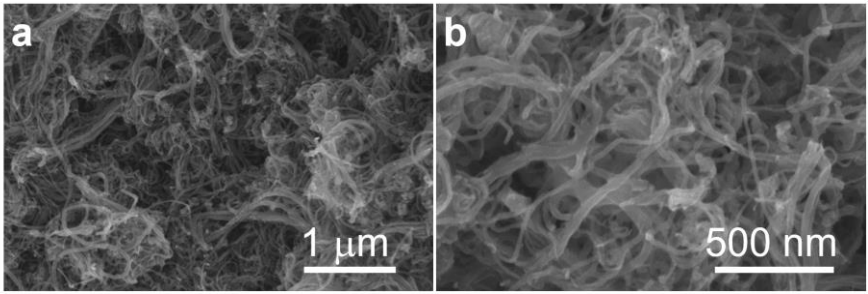

Figure 4-8 – SEM images of MWCNT-S mixture with **a**, small and **b**, large magnifications.

XRD techniques were carried out to examine the materials presented in the mixture. Sulfur powder and MWCNT powder were analysed separately and as a mixture. The sharp peaks from sulfur powder matched the reported elemental S_8 (01-78-1889) which had an orthorhombic structure with two main peaks at 23.1° and 27.7°. The spectrum for MWCNT powder exhibited a broad peak centered at 25.8° and two overlapping peaks at 42.8° and 44.2°. From the XRD spectrum of the mixture, the distinctive structural fingerprints of both materials overlaps resulted in a hump from ~20° to 30°.

The high sulfur loading and higher crystallinity made the intensity of sulfure peaks stronger in comparison to that of MWCNT. No new phases were presented indicating no phase transformation during thermal infusion.

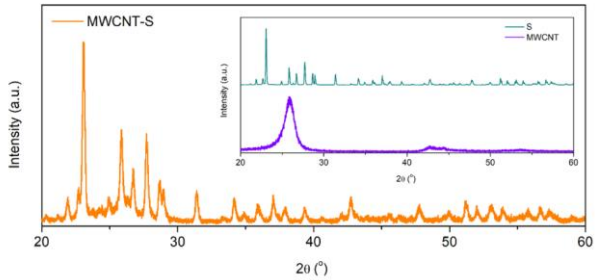

Figure 4-9 – XRD patterns for MWCNT, pristine elemental sulfur and MWCNT-S mixture.

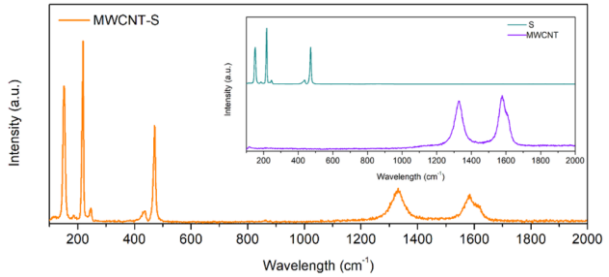

Figure 4-10 – Raman spectra for MWCNT, pristine elemental sulfur and MWCNT-S mixture.

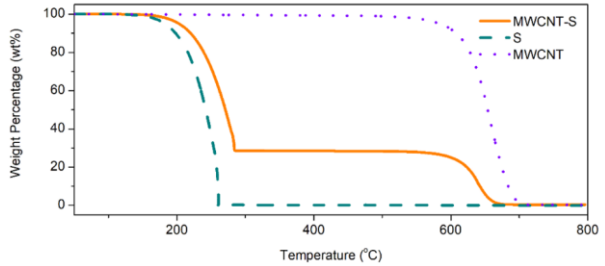

Figure 4-11 – TGA analyses for MWCNT, pristine elemental sulfur and MWCNT-S mixture.

To further investigate the chemical structures and physical phases of the composite, Raman spectrometry was employed to examine sulfur, MWCNT and MWCNT-S mixture. The spectrum for MWCNT had similar features compared to the carbon presented in TiO_2-CNF interlayer; with D band at 1340 cm^{-1} and G band at 1600 cm^{-1}. The I_D/I_G was close to unity, indicating MWCNT was partially graphitised. The S-S bond vibrations reflected several characteristic peaks below 500 cm^{-1} in sulfur powder. The spectrum for MWCNT-S was merely an overlap of sulfur and MWCNT spectra. This agreed with the XRD pattern proving there was no chemical reaction between sulfur and MWCNT.

Confirmed by the TGA study, the MWCNT-S cathode achieved a high sulfur loading of 70 wt%. The TGA curves comprised two stages of weight loss. The first one started from 150 °C and ended around 270 °C corresponded to the evaporation of sulfur. The combustion of MWCNT caused the second weight drop between 600 and 700 °C. sulfur evaporation began at a higher temperature in the mixture as compared to pure sulfur evidenced strong bonding between sulfur and MWCNT.

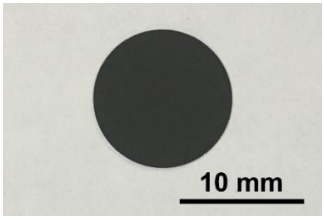

Figure 4-12 – Photos of MWCNT-S cathode.

The as-prepared MWCNT-S composite was mixed with carbon black and polyvinylidene fluoride (PVDF) binder at a weight ratio of 7:2:1 in N-methyl-2-pyrrolidinone (NMP) to prepare the cathode slurry. Carbon black was added to improve the electrical conductivity whereas PVDF worked as an adhesion agent between the sulfur cathode and aluminium current collector. The slurry was doctor bladed onto the aluminium current collector with 100 μm thickness and dried under vacuum at 60 °C for 24 hours to remove the solvents.

§ 4.3. Coin cell assembly and disassembly

Two-electrode coin cells (CR2025) were fabricated to test the electrochemical performance of the TiO_2-CNF interlayers by sandwiching them between separators and MWCNT-S cathodes. Cells without interlayers were fabricated as a controlled group.

The obtained TiO_2-CNF interlayers and dry MWCNT-S cathodes were cut into a small disk with a diameter of 11 mm and areal loading of 1.6 and 3.0 mg cm^{-2} respectively. The counter electrodes, anodes, were lithium metal plates. A commercial microporous separator, Celgard 2325, was dipped with electrolyte prepared by dissolving 1 M bis (trifluoromethane) sulfonimide lithium salt (LiTFSI) in a 1:1 (v/v) mixture of 1,2-Dimethoxyethane (DME) and 1,3-Dioxolane (DOL) with additional 2 wt% of $LiNO_3$. $LiNO_3$ is a common additive to the electrolyte to minimise polysulfides shuttle effect[134]. The last step was to assemble the cathodes, interlayers, separators, electrolyte and anodes into coin cells in an Ar-filled glove box with oxygen and moisture concentration kept below 0.1 ppm.

To understand the cell chemistry and study the dissolution of polysulfides during the electrochemical reactions, coin cells at various charging and discharging cycles were dissembled in the Ar-filled glove box to recover the active materials. The active materials were washed with DME to remove the residues and scraped off from the current collector. The collected materials were studied using TEM for both imaging and SAED. XPS analysis was conducted to study the valence state of transition metal.

§ 4.4. Results and discussion

To examine the performance of TiO_2-CNF interlayer, it was paired with an MWCNT-S cathode to make a cell and compared to a cell with bare MWCNT-S cathode through a series of electrochemical analyses.

The electrochemical performances were further studied under long cycle life testing. Deep cycling from 1.8 to 2.6 V at a current rate of 0.2C was applied to both cells. As opposed to the cell with bare MWCNT-S, the cell with an interlayer exhibited tremendous improvement in trapping and re-utilising the shuttling polysulfides as

indicated by the specific capacity and Coulombic efficiency results shown in Figure 4-13a. The cell delivered an initial discharge capacity of 1,238 mAh g^{-1}, which was 74% of the theoretical value (calculated based on active sulfur mass ~3.0 mg). The cell produced a high discharge capacity of 770.8 mAh g^{-1} even after cycling for 300 times with an average Coulombic efficiency of 99%. The incorporation of TiO_2-CNF interlayer greatly increased the electrochemical performances with 46% improvement in initial discharge capacity, 5% more in average Coulombic efficiency, 25% increase in capacity retention and 150% increase in reversible capacity after 300 cycles as compared to the cell without an interlayer.

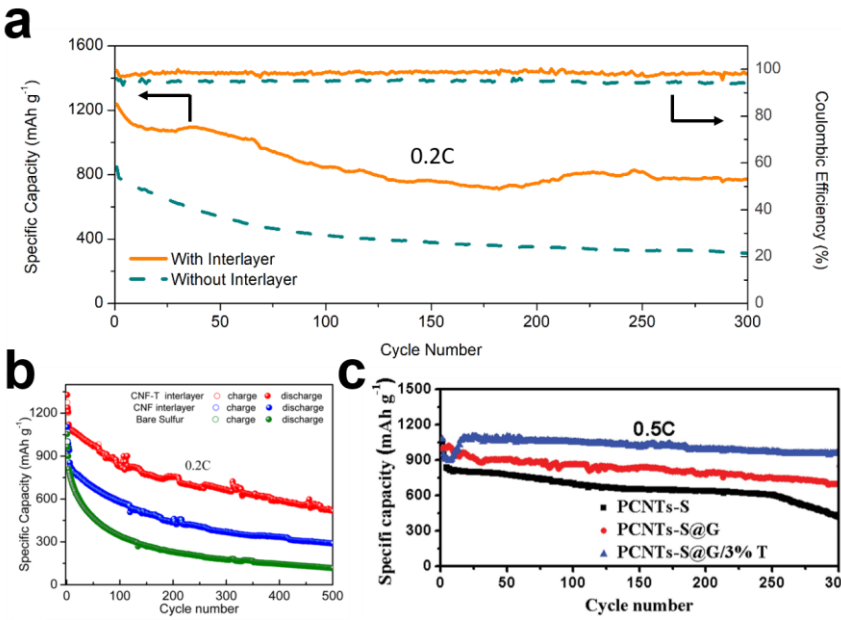

Figure 4-13 – Long cycle testing of different LSBs with and without interlayers. **a**, TiO_2-CNF interlayer. **b**, CNF-TiO_2 interlayer prepared by Liang et al[265]. **c**, Graphene-TiO_2 interlayer prepared by Xiao *et al*[266]. **(b) and (c)** are results from reported literature.

There was an increase in discharge capacity after the 30th cycle. This incremental phenomenon was associated with gradual Li^+ ions diffusion through electrolyte onto cathode since the interlayer impeded direct contact between active material and electrolyte. Therefore, not all sulfur was reacted in the early cycles[129]. Another feature appeared in the cycle life curve for interlayer incorporated cell was observed: the curve did not decay smoothly as compared to the cell with bare MWCNT-S cathode, instead, it bounced up and down throughout the testing. This was attributed to the excessively robust chemical affinity between TiO_2 and polysulfides that unpredictably prevented a proportion of polysulfides from oxidising back to elemental sulfur during re-utilisation. The process can be described as "sulfur locking" and "sulfur unlocking" during cycling. This was also reported in recent attempts to fabricate multifunctional interlayer with TiO_2 nanoparticles deposited onto CNF mat[265] (Figure 4-13b). A number of inevitable residues polysulfides bonded on to TiO_2 crystals may potentially be reduced by lowing the TiO_2 content. In Hunag's recent publication, the group deposited only 3 wt% of TiO_2 onto graphene interlayer[266]. As a result, the capacity decayed in a rather smooth manner as shown in Figure 4-13c, suggesting the amount of polysulfide anchor may directly affect the cycle stability of the cell. Apart from affecting cell stability, another practical reason to reduce the amount of TiO_2 is its weight. In the above deep cycling, the calculations for specific capacity did not take the weight of interlayer into consideration. If the calculations were based on the total weight of interlayer and active materials, the advantage of intercepting polysulfides with interlayer would be outweighed by its own weight during the first 10 cycles. Even at the end of 300 cycles, the overall improvements would be merely 36% in terms of discharge capacity. From these results, it is important for any future work to find the critical amount of polysulfide for effective trapping at the lowest possible weight.

After cycling, the cell was dissembled, and the interlayer was examined by STEM and EDS mapping to investigate the reason for the improvements. It is worth mentioning that the robust nanostructure remained intact after 300 deep cycles. From the enlarged STEM images, small nano dots (pointed by red arrows) were found to sit on the anchored TiO_2 nanoparticles. The elemental mapping not only confirmed those dots were sulfur species chemically adsorbed onto TiO_2 particles but also revealed the uniform distribution of sulfur species throughout the whole composite. Further large

area EDS mapping revealed sulfur species weren't only distributed uniformly on the cathode side but also the separator side of the cycled interlayer. Nevertheless, higher sulfur content was detected on the cathode facing side, suggesting effective polysulfide interception with the hybrid TiO_2-CNF interlayer.

Further chemical state at the cathode facing surface of cycled interlayer was investigated with XPS. Figure 4-15a compared the XPS spectra of Ti 2p before and after deep cycling. A shift and a drop in intensity in binding energy of characteristic Ti 2p peaks were observed after cycling was observed. The Ti $2p_{3/2}$ and Ti $2P_{1/2}$ shifted from 459.1 to 459.2 eV and 464.8 to 465.0 eV, respectively. The slight shift was caused by chemical interaction between the sulfur species and TiO_2 and the drop was attributed to sulfur species coating at TiO_2 surface. The peaks at 162.0 and 161.2 eV in the S 2p spectrum further confirmed the existence of Ti-S bond. Different types of sulfur species were identified in the S 2p XPS spectrum, including Li_2S_2 (163.5 eV), S_8 (165.0 eV), and polythionate complex (169.7 eV, 170.5 eV). The deposition of Li_2S_2 was predictable and inevitable due to its poor electrochemical reversibility. Polythionate complex is a polysulfide mediator formed by $LiNO_3$ oxidised polysulfides that can chemically restrain active loss. Chemisorption by TiO_2 particles was proved to be a feasible way to mitigate polysulfides migration.

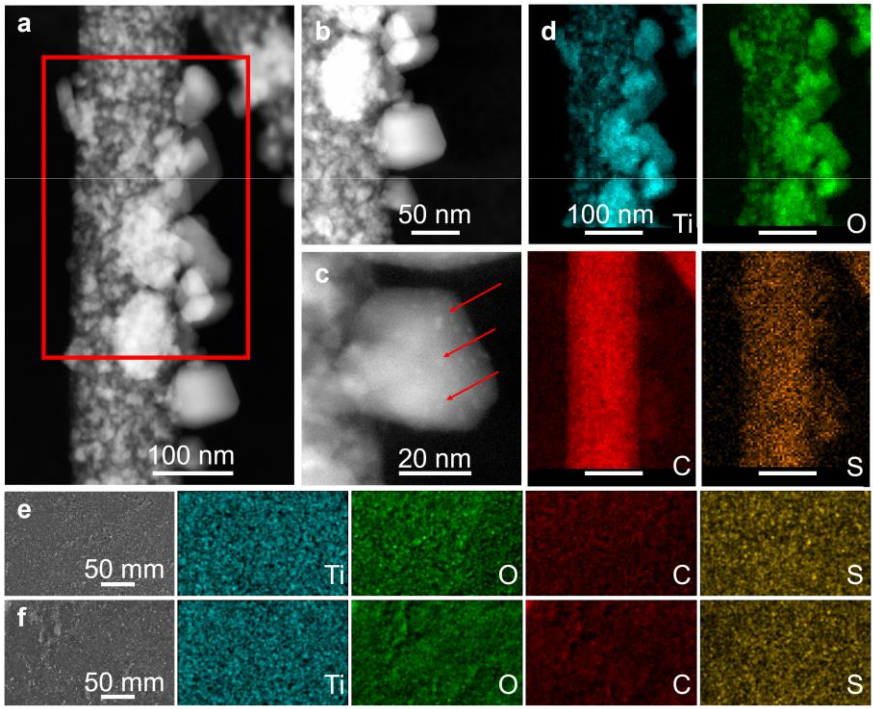

Figure 4-14 – Post mortem analysis on cycled LSBs with TiO_2-CNF interlayer. **a-c**, STEM image from low to high magnifications and the corresponding elemental mappings after cycling. Cyan being Ti, green being O, red being C and orange being S. The scale bar in elemental mapping for all four is 100 nm. Elemental mappings from EDS of SEM for **d**, cathode side and **e**, separator side of the TiO_2-CNF interlayer.

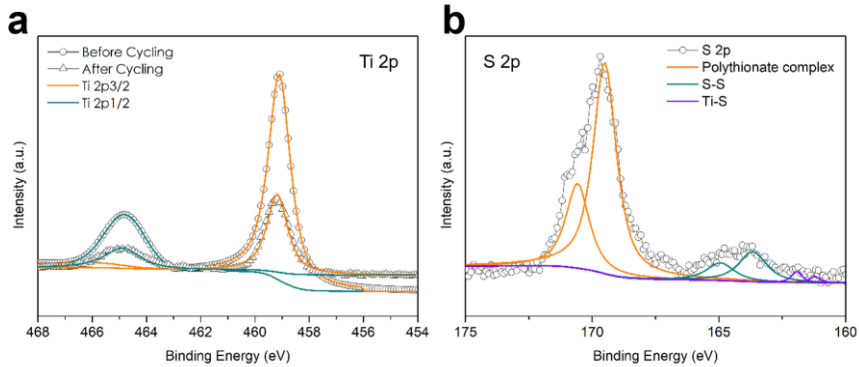

Figure 4-15 – Surface composition analysis via XPS. **a**, Ti 2p XPS spectrum of interlayer before and after cycling. **b**, S 2p XPS spectrum of interlayer after cycling.

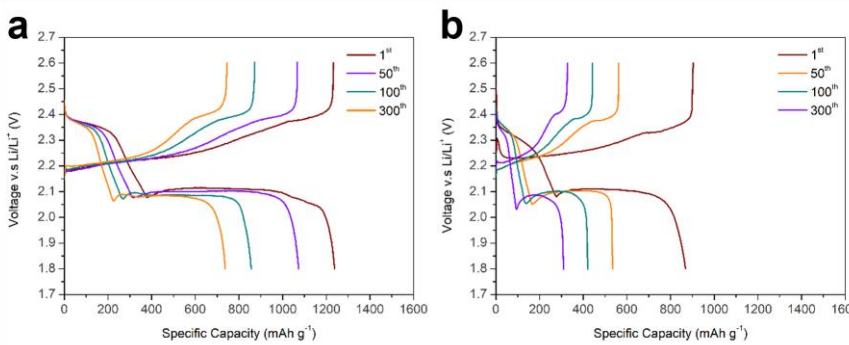

Figure 4-16 – Galvanostatic discharge-recharge curve of cell **a**, with and **b**, without a TiO_2-CNF interlayer at 1st, 50th 100th and 300th cycle under a current rate of 0.2C.

Galvanostatic discharge-charge profiles at 1st, 50th 100th and 300th cycle were shown to explore the discharge behaviour. With or without the interlayer, both cells exhibit two discharge plateaus at all discharge cycles. The high and steep plateau that took place from ~2.3 V corresponds to the formation of LCPs from initial cyclo-S_8 ring whereas the long and planar plateau represents further lithiation to eventually form Li_2S. Upon

recharging, the reverse process was carried out by oxidising Li_2S back to elemental sulfur. The discharge-charge profile proved the inserted interlayer did not interfere with the characterised electrochemical redox reaction taken place in LSBs.

Furthermore, the similar voltage plateau suggested that the addition of the interlayer did not produce a significant increase in internal resistance.

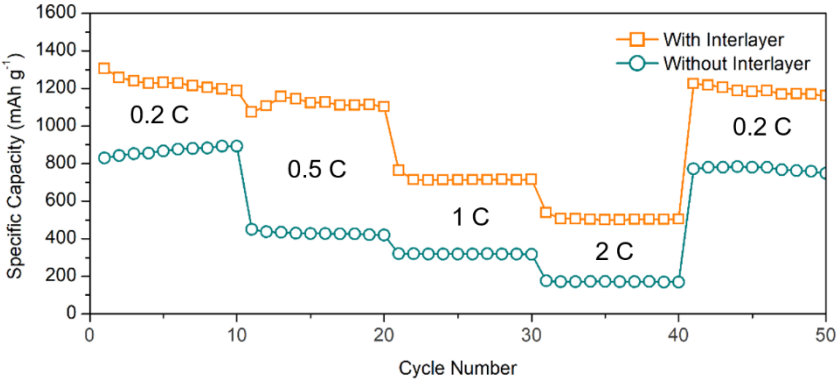

Figure 4-17 – Comparison of rate performance of cell with and without a TiO_2-CNF interlayer starting with a current rate of 0.2C, then increase step wise to 0.5, 1 and 2C and a drop back to 0.2C at the end.

Figure 4-17 shows rate capabilities of LSBs with and without TiO_2-CNF interlayer. The specific capacity of interlayer incorporated cell decayed at an obvious rate when the current was smaller (0.2 and 0.5C). This can be attributed to incomplete re-utilisation of active materials that bonded with TiO_2 since there was insufficient current to drive the redox reactions. In the first 10 cycles, the average capacity was high at 1,229.5 mAh g^{-1}, at the end of 10^{th} cycle for each current rate the discharge capacities were 1,102.3, 715.4, and 504.8 mAh g^{-1} respectively. When the current rate was reduced back to 0.2C, the system recovered a reversible capacity of 93.8%. This indicated the interlayer-cathode pair has stronger rate tolerance and structural stability. In the contrary, the cell without interlayer only recovered 86.5% of its initial discharge capacity under the same cycle conditions. Indicating a loss of active materials towards the anode and form shuttle tunnels between the electrodes during high rate cycling.

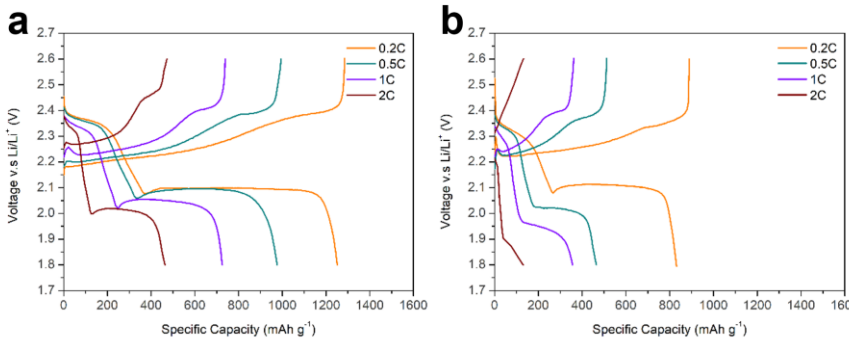

Figure 4-18 – Galvanostatic discharge-charge curve of cell **a**, with and **b**, without a TiO_2-CNF interlayer at different current rates.

The discharge and charge profiles were employed to examine the discharge behaviour at different current rates. The profiles for the cell with interlayer had merely subtle deviation in plateau potential at increasing rates, this suggested a stronger tolerance to the higher current rate. A potential plateau of 2.0 V was maintained even at 2C in the interlayer incorporated cell as opposed to a drop of potential below 1.9 V in the bare cathode cell. Both rate performance and discharge-charge profiles showed consistent results.

§ 4.5. Conclusions

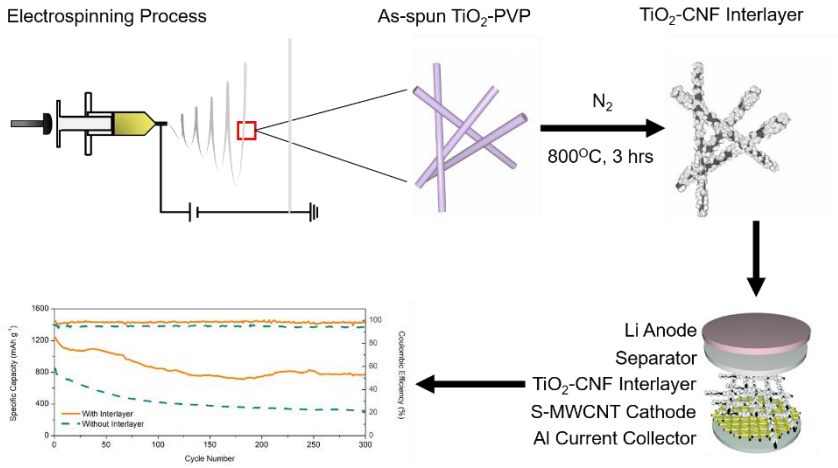

Figure 4-19 – Image summary. From the synthesis of TiO_2-CNF interlayer the assembly of LSBs and the results.

In this report, a flexible 3D hierarchical TiO_2-CNF interlayer was designed to perform both chemical and physical adsorption to mitigate polysulfides dissolution and shuttling. The multi-functional interlayer successfully improved the electrochemical performance owing to the followings: 1.) TiO_2 particles throughout the CNF backbone act as effective trapping and re-utilisation sites for polysulfides, 2.) the conductive network of mesoporous CNFs hosted sulfur species as redox reaction sites and enhanced the electrical conductivity and 3.) the springiness nature of CNF scaffold act as a buffer during the volume expansion. As a result, the TiO_2-CNF interlayer increased initial discharge capacity by 46%, prolonged the cycle life with 25% more capacity retention at the end of 300 cycles and improved the average Coulombic efficiency by 5% as compared to the cell without interlayer (calculated on the basis of active S mass). Nevertheless, the high weight percentage of TiO_2 had some adverse affects in cycle stability from the process of too much attraction to sulfur causing locking and unlocking instability; furthermore, the advantages of its polysulfide anchoring ability was outweighed by the mass in the short run. It is also important not to completely shut

down the shuttling mechanism as a small amount of shuttling can increase the safety of using lithium as an anode by reacting with the dendrites and breaking them down.

Regarding the unique design of the structure, the *in situ* grown TiO_2 nanoparticles decorated the CNF framework with a size gradient from the core to the surface. The robust mechanical structure comes from small TiO_2 particles buried inside to hold the whole structure together. The unique matting mechanism from PVP carbonisation and TiO_2 molecules diffusion at high-temperature pyrolysis of as-spun TiO_2-PVP mat-like felting. In the non-woven form, this electrospun composite with entangled nanofibres can provide a combination of excellent mechanical properties, including stiffness, toughness and pliability.

All in all, the TiO_2-CNF composite interlayer herald a single-step approach to structural design chemi-/physisorptive interlayers for advanced LSBs. Nevertheless, much still need to be done to further enhance the electrochemical role of interlayer regarding the areal density, the amount or the type of polysulfide anchors.

Chapter 5

Oxygen Defect Chemistry for the Reversible Transformation of Titanates for Sizeable Potassium Storage

Potassium-ion batteries (KIBs) are promising substitutes for lithium-ion batteries (LIBs) due to the Earth-abundancy of potassium[17,18]. However, practical KIB applications are hindered by slow diffusion kinetics and severe structural deterioration as the large cation is cycled in and out of the electrode, respectively leading to low specific capacity and short lifetime[213,267].

Here, an oxygen deficient loose-layered potassium titanate (LL-KTO) was reported to electrochemically store a large amount of potassium (201 mAh g^{-1}) over 1800 cycles via a stacked ↔ sliced structural transformation. Different from the rigid host in intercalation process, LL-KTO delaminates into titania nanosheets when potassium leaves the structure; in the reverse reaction, K^+ ions and titania nanosheets stack back layer-by-layer into the original LL-KTO. As a result, LL-TO exhibits specific capacities that are par with values for titanium-oxide based LIBs[148–150,161,162]. We further demonstrate Peukert's constant[268], fractal dimension[268] and inverse of cations per transition metal as matrices to evaluate the performance of electrodes and show LL-KTO with stacked ↔ sliced structural transformation could be a potential solution to push the kinetic boundary and approach the thermodynamic limit of ion batteries. This work provides an important guide to design future energy storage systems and a method to compare electrode materials across different systems.

Parts of the findings are reported in:

Cheng-Yen Lao†, Yingjun Liu†, Jun Hu, Neng Li, Giorgio Divitini, Wei (Alex) Wang*, Qiyao Yu*, Xingzhu Chen, R. Vasant Kumar*. Oxygen defect chemistry for the reversible transformation of titanates for sizeable potassium storage. (2019).

*Corresponding authors.

†These authors contributed equally.

C-Y.L., Y.L., W.W. and R.V.K. conceptualised the study and wrote the manuscript. C-Y.L. designed and performed the experiments. C-Y.L., Y.L. and R.V.K. analysed and interpreted data. G.D. contributed to the TEM acquisition. W.W. and Q.Y. supervised and J.H. performed the electrochemical testing and *ex situ* studies. N.L. supervised and X.C. performed the theoretical computations. All authors contributed to the overall discussions and edited the manuscript.

§ 5.1. Introduction

To our knowledge, this is the first time a new ion storing mechanism is designed to compete for the diffusion limit and structural deterioration specifically for KIBs. While different strategies were designed according to distinct ion transport behaviours – proton by Grotthuss hopping[269], lithium by solid diffusion and sodium by surface transition[270,271], all these strategies have, however, failed for potassium due to its large size.

As aforementioned in the literature review, large ions are intrinsically more difficult to store. Intercalation mechanism is yet the most practical mechanism as it endures minimum volume expansion when compared to conversion and alloying mechanism. One of the strategies to store large ions trough intercalation is to synthesis layered material with large enough interlayer space, nevertheless, the solvation radius of large ions may still have shielding effect that expands the layers while ions diffuse into host sites[213,272,273]. Based on previous work on amorphous structured[186,187,204] anodes for KIBs, a hypothesis of another ion storing mechanism is proposed. Instead of preparing a rigid-structured host, a loose-structured host will be synthesised and fabricated into an electrode layer.

In details: during charging, the layered host will be delaminated into 2D nanosheets when ions are extracted out of the structure; in the reverse reaction, these ions and 2D nanosheets will restack together back into the original layered host. A reversible stacked ↔ sliced structural transformation happened during charging and discharging.

Taking a tower parking system as an analogy to compare the named "stacked ↔ sliced structural transformation" and interaction mechanism, where tower parking system and cars represent layered material and ions respectively:

1. Intercalation mechanism is when the cars park into a ready-built rigid parking tower.
2. "Stacked ↔ sliced structural transformation" is when the cars park on the ground floor (2D nanosheet) and the first floor (another layer of 2D nanosheet) being built on top of the cars, so on and so forth. This parking tower system is built along with cars parking inside. In the reverse reaction, by removing the cars, the tower delaminates into individual floors, thus loose-structured.

The advantages of the proposed mechanism are: 1.) The ions will not experience slow solid diffusion within the layered structure, instead, they are deposited directly onto the 2D nanosheets in a liquid electrolyte. 2.) There will be net-zero volume expansion since the layer spacing is adjusted according to the ion size. This mechanism addresses issues of sluggish diffusion and severe structural deterioration associated with large ions[213,267].

To support this hypothesis, layered titanates as electrodes for KIBs were prepared to study the mechanism. Titanium-based materials have advantages in terms of high safety, large abundancy, low cost and low toxicity[212]. More importantly, reversible exfoliation and restacking of titanates have been reported with chemical and/or physical methods in order to accommodate organic and inorganic species[274–276]. Nevertheless, the repeatability and the stability of transformation are poor and most importantly, this process has not been realised in an electrochemical mode. While stacking 2D materials with guest ions, molecules or other 2D materials is a well-established technique to synthesising inclusion complexes[277–283], the processes are almost non-exclusively irreversible. Therefore, the crucial step is to make the layered host "loose" enough so that it will delaminate upon guest ion removal.

§ 5.2. Materials synthesis and characterisation

In this chapter, two different potassium titanates (LL-KTO and KTO) were prepared using oxygen deficient TiO_2 anatase nanoparticles ($Anatase_{2-\delta}$) as the starting material. $Anatase_{2-\delta}$ was synthesised by electrospinning technique with the same TiO_2-PVP electrospinning precursor in section § 4.2.1. Electrospun TiO2-CNF interlayer. After the electrospinning, the nanofibre mats were peeled off the aluminium foil and pyrolysed at 600 °C under an N_2 atmosphere for 3 hours to form $Anatase_{2-\delta}$. LL-KTO was prepared by chemically reacting $Anatase_{2-\delta}$ with 15M KOH_{aq} in a Teflon container in an oven at 80 °C for 48 hours and KTO was prepared by chemically reacting $Anatase_{2-\delta}$ with 15M KOH_{aq} in a Teflon-lined autoclave in a furnace at 200 °C for 20 hours. Both samples were washed with ethanol to remove excess KOH_{aq} and dried at 80 °C overnight.

$Anatase_{2-\delta}$ were formed *in situ* within the smooth CNFs while some of them protruded the surface of CNFs (indicated with yellow arrows) as observed in Figure 5-1a,b with SEM images. The CNFs had an average width of 108 ± 24 nm and served as a reduction agent to reduce the anatase. Its oxygen deficiency was confirmed with XPS and electron paramagnetic resonance (EPR) spectroscopy as shown in Figure 5-2. The average size of $Anatase_{2-\delta}$ was less than 5 nm as shown in the TEM image (Figure 5-1c). Furthermore, the element distribution of these nanofibres mapped by STEM in Figure 5-1d showed a uniform distribution of $Anatase_{2-\delta}$ within the CNFs.

Formation of LL-KTO is illustrated in Figure 5-3 and reflected by Equation 5-1. During the formation, OH^- ions selectively dissociated the longer Ti-O-Ti bonds (1.98 Å) to form intermediates that were rearranged into lepidocrocite structure under the electrostatic attraction of K^+ ions[284,285].

$$TiO_{2-\delta} + KOH_{aq} \rightarrow K(TiO_{2-y})_4OH \quad \text{Equation 5-1}$$

Figure 5-1 shows morphological contrast before and after the KOH_{aq} reaction. After the reaction, the surfaces of the CNFs were wrapped with highly cross-linked LL-KTO nanofibers with an average diameter of 6 nm as shown in Figure 5-1e,f. There was no change to the average width of CNFs (~108 nm) before and after the reaction. The TEM images of Figure 5-1g reveal the laminar structure of LL-KTO with an interlayer

spacing of 8.8 Å. The element distribution mapped by STEM (Figure 5-1h) confirms those thin nanofibres were LL-KTO and the thicker ones were CNF backbones. From the EPR in Figure 5-2b, oxygen vacancies were also presented in LL-KTO, as indicated by the symmetric paramagnetic signals with g-factor=2.003 [286]. Compared with Anatase$_{2-\delta}$, greater intensity and smaller peak-to-peak linewidth of LL-KTO indicated more oxygen vacancy sites that were also more uniformly distributed.

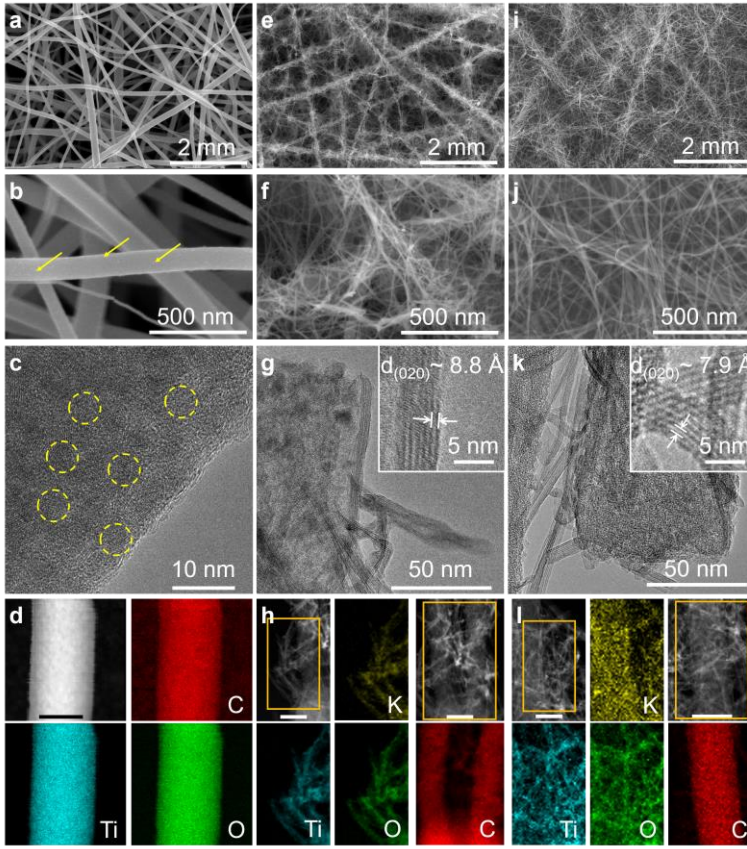

Figure 5-1 – Morphology and chemical distributions before and after the KOHaq reaction. SEM, TEM and STEM images and EDS elemental mapping of **a-d**, Anatase$_{2-\delta}$, **e-h**, LL-KTO,

i-l, KTO. The insets of **(g)** and **(k)** show the laminar structure and interlayer spacing of LL-KTO and KTO. The scale bar in elemental mapping for all four is 100 nm.

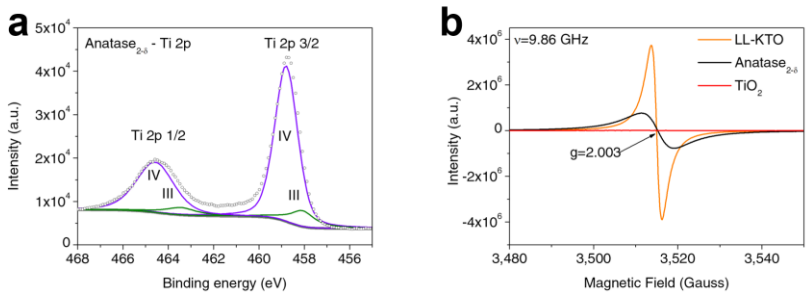

Figure 5-2 – Oxygen deficiency in Anatase$_{2-\delta}$ and LL-KTO. **a**, XPS spectra of Ti 2p in Anatase$_{2-\delta}$ shows Ti is composed of 12.9% Ti^{III} and 87.1% Ti^{IV} and suggests Anatase$_{2-\delta}$ has a chemical formula of $Ti^{III}_{0.13}Ti^{IV}_{0.87}O_{1.935}$. However, since the samples were exposed to air before XPS analysis, Ti^{III} may easily be oxidised during the process with somewhat misleading results. A general formula for Anatase$_{2-\delta}$, $TiO_{2-\delta}$, is used in this manuscript to present the nominal formula. **b**, EPR analysis of Anatase$_{2-\delta}$ LL-KTO and commercial TiO_2.

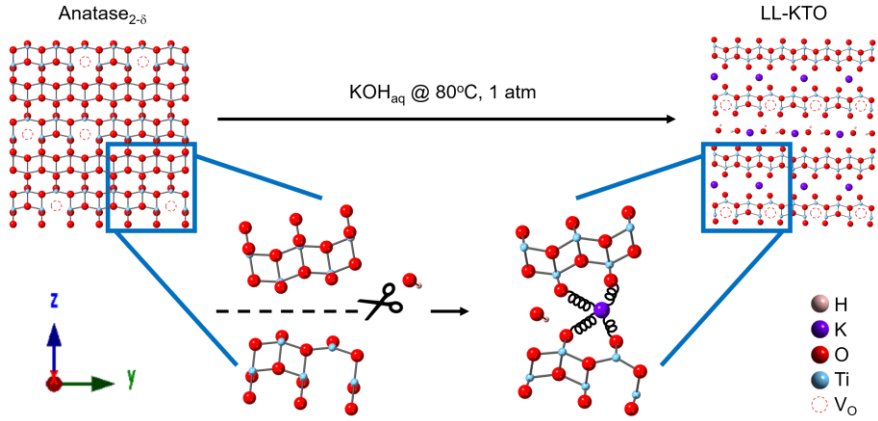

Figure 5-3 – Schematic illustration of the formation process of LL-KTO from Anatase$_{2-\delta}$.

A conventional KTO as the reference to LL-KTO was prepared by a hydrothermal method, a common method to make titanates[285,287–289]. The difference between this and the formation of LL-KTO could be considered as intense vs. mild KOH_{aq} treatment. The as-prepared KTO was dried at 80 °C overnight. It had similar morphology as compared to LL-KTO (Figure 5-1). The difference between LL-KTO and KTO was very subtle macroscopically with observable difference in terms of interlayer spacing with KTO's being 7.9 Å (Figure 5-1k). The larger interlayer distance in LL-KTO maybe key of indicating a "loose" layered structure that was expected to use to prove the "stacked ↔ sliced structural transformation" hypothesis.

XRD was performed to study the crystallography information of all three materials. The XRD data (Figure 5-4) show complete phase transformation from $Anatase_{2-\delta}$ into both LL-KTO and KTO. The distinctive (011) peak for the anatase phase was completely absent. Instead, clear (020) peaks at 10.1° and 10.9° featured the laminar structure were observed for LL-KTO and KTO, respectively. These corresponded to d-spacing of 8.76 and 8.01 Å, respectively, compatible with the values taken from TEM (Figure 5-1). The other diffraction peaks at 24.1° and 28.3° represented the in-plane structure of the titanate ((210) and (230), respectively)[282].

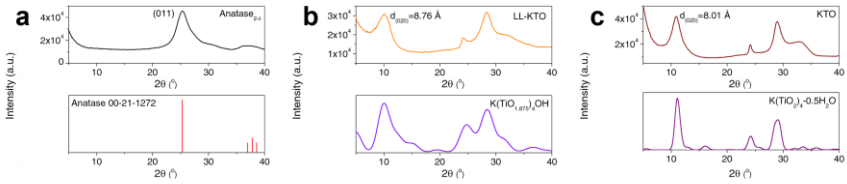

Figure 5-4 – XRD profiles of **a,** $Anatase_{2-\delta}$, **b,** LL-KTO and **c,** KTO. Top: Experimental. Bottom: Reference for $Anatase_{2-\delta}$ and calculated profile for LL-KTO and KTO.

The XRD data of LL-KTO and KTO could not be matched with any reported structure in our database. A list of possible candidates $K_m(TiO_{2-y})_p(OH)_m$ (m=1-3, y=0-0.25, p=2-4) were therefore screened using both CrystalMaker and density functional theory (DFT) study in order to determine the chemical formula of LL-KTO and KTO. The

results of the calculated XRD pattern based on the simulated structure were shown on the bottom half of Figure 5-4.

The screening process went as follows: 1.) crystal structures were constructed with CrystalMaker by me → 2.) these structures were refined by DFT calculations by N.L. and X.C. → 3.) XRD diffraction pattern of the refined structures were calculated using CrystalDiffract by me → 4.) based on the diffractions, further alternations to the structures were made with CrystalMaker by me → 2.) → 3.) → 4.). These processes were repeated for a few times until the least-difference between the experimental and calculated XRD patterns were reached.

Well-resolved Vienna Ab initio Simulation Package (VASP) was used for all DFT calculations[290–292]. The exchange–correlation functional was described by generalised gradient approximation of Perdew–Burke–Ernzerhof (GGA-PBE)[293]. To describe the van der Waals in this system, the DFT-D3 empirical correction of Grimme was carried out[294]. The energy cut-off was set to 450 eV. For geometry optimisation, quasi-Newton algorithm was used to relax the ions until the conditions of convergence, 10^{-5} eV per atom in energy and 0.02 eV $Å^{-1}$ in force, were reached. A Monkhorst–Pack special k-point $5 \times 1 \times 7$ mesh was used for sampling the Brillouin zone. The GGA+U (U = 4.2 eV) method was introduced to describe the strong intra-atomic interaction of the 3d electrons of the Ti element.

Below, in Figure 5-5, structural evolution that led to the confirmed structure of LL-KTO and KTO is presented along with the concepts explained. The detailed cell parameters of these structures are shown in Table 5-1. To begin with, lepidocrocite structure was found to be the closest structure after a thorough literature survey [149,150,284,285,287–289,295–303]. It has a laminar structure in which each 2D layer has TiO_6 octahedra linked with neighbouring octahedra via edge-sharing; in between the layers, there can be guest ions or nothing [149,150,285,287,288,296]. In the first step, lepidocrocite laminar structure with inserted K^+ and OH^- ions between the layers was constructed to form $K_4(TiO_2)_4(OH)_2$. It was a supercell with two layers of TiO_6 octahedra sandwiching the ions. In the second step, an oxygen vacancy was introduced to reflect the findings from EPR spectroscopy (Figure 5-2b) and $K_4(TiO_{1.75})_4(OH)_2$ was formed. The structure at this point contained excess of potassium. Therefore, in the next step, one potassium

atom was removed to make $K_3(TiO_{1.75})_4(OH)_2$. The XRD patterns had not deviated from the original one so far. To shift the (020) peak to the right (decreasing the d-spacing/interlayer spacing of the structure), one OH molecule was removed and resulted in the c axis to dramatically decrease from 21.79 Å to 18.56 Å. Since it was still potassium in excess, one potassium atom was further removed to make $K_2(TiO_{1.75})_4OH$. In the next step, the supercell size was doubled the to 2 x 1 x 1 with one more potassium atom removed but all the oxygen atoms inserted back (to prevent the structure collapsing during refinement) to construct $K(TiO_2)_4OH$, as illustrated in Figure 5-5c. To finally obtain structures for LL-KTO and KTO, two oxygen atoms, circled in orange and brown were removed separately. By removing the oxygen atom circled in orange, $K(TiO_{1.875})_4OH$ that closely matched experimental data of LL-KTO was obtained; on the other hand, by removing the oxygen atom circled in brown, $K(TiO_2)_4{\cdot}0.5H_2O$ that closely matched experimental data of KTO was obtained. The calculated profiles in Figure 5-4b,c were based on the calculated XRD peaks for a grain size of 3.3 nm and 5.0 nm for $K(TiO_{1.875})_4OH$ and $K(TiO_2)_4{\cdot}0.5H_2O$, respectively. The selected grain sizes were calculated by Scherrer equation[304] based on the experimental data of LL-KTO and KTO.

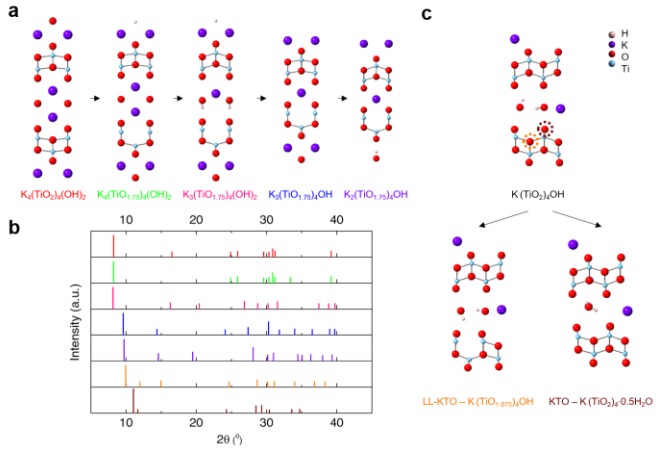

Figure 5-5 – Screening sequence of the possible structure for LL-KTO and KTO. **a**, Schematic illustrations of simulated structures of lepidocrocite-type layered $K_4(TiO_2)_4(OH)_2$,

$K_4(TiO_{1.75})_4(OH)_2$, $K_3(TiO_{1.75})_4(OH)_2$, $K_3(TiO_{1.75})_4OH$ and $K_2(TiO_{1.75})_4OH$. **b**, the corresponding XRD patterns of above structures and LL-KTO and KTO as coded in colours. **c**, Transformation from $K(TiO_2)_4OH$ to LL-KTO and KTO.

Table 5-1 – Cell parameters for simulated structures.

Structures	Lattice Constant (Å)			Angles (°)		
	a	b	c	α	β	γ
$K_4(TiO_2)_4(OH)_2$	3.92	21.48	3.02	87.00	90.00	90.00
$K_4(TiO_{1.75})_4(OH)_2$	3.83	21.95	3.00	87.00	90.00	90.00
$K_3(TiO_{1.75})_4(OH)_2$	3.73	21.79	3.02	86.05	90.00	90.00
$K_3(TiO_{1.75})_4OH$	3.84	18.56	3.00	83.43	90.00	90.00
$K_2(TiO_{1.75})_4OH$	3.73	18.35	3.02	82.66	90.00	90.00
$K(TiO_{1.875})_4OH$ – LL-KTO	7.40	17.91	3.01	82.88	89.94	91.07
$K(TiO_2)_4 \cdot 0.5H_2O$ – KTO	7.58	16.19	3.01	81.29	89.88	91.60

One interesting thing to point out for LL-KTO synthesis process was that the reaction temperature at 80 °C was the lowest ever reported for forming titanates[150,285,289,303,305]. Applying the same reaction to other forms of TiO_2, however, only led to negligible LL-KTO formation (Figure 5-6). Commercial anatase nanoparticles, oxygen deficient anatase-carbon composite granular from pyrolysed electrospun precursor and rutile-CNF composite from pyrolysed electrospun PVP-TiO_2 nanofibres were tried. These observations suggest the oxygen vacancies that concentrated at the surface of $Anatase_{2-\delta}$[306] and the accessibility of KOH_{aq} to the titanium source were the key prerequisite for thorough LL-KTO formation.

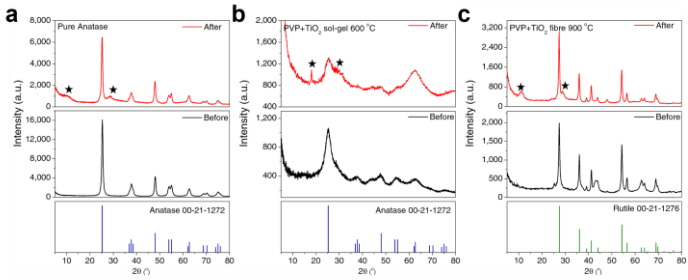

Figure 5-6 – XRD spectra of other forms of TiO_2 before and after the same KOHaq reaction. a, Anatase nanoparticles less than 10 nm (Sigma-Aldrich). b, Pyrolysed TiO_2 – PVP sol-gel. c, Pyrolysed electrospun PVP – TiO_2 nanofibre. Star indicates the LL-KTO phase.

Apart from the titanium-based material prepared, the CNFs in all three samples were examined. Using TGA, the weight percentage of CNFs in each sample were calculated. There were about 4 regions of weight drop that can be observed from the TGA curves (Figure 5-7). Region I represented the immediate weight loss of water molecules adsorbed on the surface. For Anatase$_{2-\delta}$ and KTO, region II was an extension of the region I where adsorbed water was continual being released from the pores. For LL-KTO, however, this region corresponded to the release of OH surface groups as well (indicated by the green box)[300]. Between ~280 and 480 °C, a rapid drop in weight indicated carbon combustion for all three samples. However, the blue box indicated a separate reaction happened for LL-KTO and KTO, the oxidation of potassium titanates. Since this side reaction was inevitable, it was impossible to determine the exact CNFs-to-titanates ratio, rather an estimated ratio was being calculated and presented in Table 5-2.

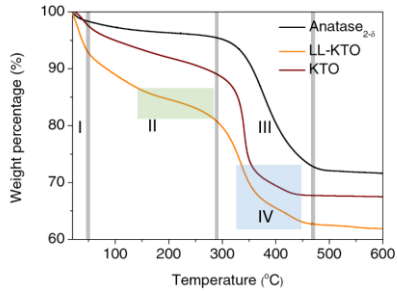

Figure 5-7 – TGA analysis of Anatase$_{2-\delta}$, LL-KTO and KTO in air up to 600 °C at a ramping rate of 10 °C per minute. All samples are dried at 100 °C for 24 hrs prior to the analysis.

Table 5-2 – Estimated percentages of CNFs in Anatase$_{2-\delta}$, LL-KTO and KTO.

Samples	CNFs (wt%)	Titania/titanates (wt%)
Anatase$_{2-\delta}$	24.4	75.6
LL-KTO	24.9	75.1
KTO	23.3	76.7

The nature of carbon was studied using Raman spectroscopy and deconvolutions of the obtained curves to distinguish between D band, A band and G band (Figure 5-8). D band indicates the disorder of graphitic carbon while G band indicates the ordered graphitic ring, they both consist mainly sp^2 bonds[307]. A band is quite different from these two, it indicates disordered carbon with mainly sp^3 bonds linking the planes of the graphite rings[308]. These types of carbon are found at *ca.* 1360, 1500 and 1560 cm^{-1} [309,310]. The proportion of each type of carbon was summarised in Table 5-3. From $Anatase_{2-\delta}$ to LL-KTO and KTO, the proportions of A band decreased while D band and G band both increased. This suggested the KOH_{aq} treatment reconfigures some of the dangling sp^3 bonds into sp^2 bonds often found in graphitic rings or chains. If the KOH_{aq} treatment were more intense (i.e. hydrothermal method used to make KTO), the change was more.

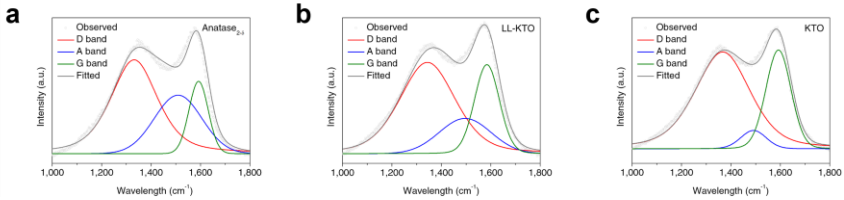

Figure 5-8 – Raman spectroscopy for **a**, $Anatase_{2-\delta}$, **b**, LL-KTO and **c**, KTO from 1000 to 1800 cm^{-1}. The curves are deconvoluted into D band, A band and G band.

Table 5-3 – Area ratio of different types of carbon band in $Anatase_{2-\delta}$, LL-KTO and KTO.

Samples	D Band	A band	G Band
$Anatase_{2-\delta}$	56.7%	28.9%	14.5%
LL-KTO	58.9%	18.1%	23.0%
KTO	67.0%	5.2%	27.8%

XPS analysis was used to further study the nature of carbon bonding. The surveys for different elements in all three materials were shown in Figure 5-9. The specific spectra for C 1s and the deconvolutions were in Figure 5-10. With stronger KOH_{aq} treatment, the amount of sp^2 bonding increased while sp^3 bonding decreased. This coincided to the findings from Raman spectroscopy where A band (sp^3 dominated) was replaced by

D band and G band (sp^2 dominated). Apart from the change of bonding character of C-C bonds. The spectra also showed increases for both O-C=O and C-O-C bond that could be attributed to OH surface functional groups adsorbed onto the surface of the carbon. The decrease in sp^2 bond and increase in other carbon bonds was yet again by a larger margin when the hydrothermal method was applied. The Raman spectroscopy and XPS study showed that the CNFs in KTO were more conductive due to the higher content of the G band and sp^2 bonding.

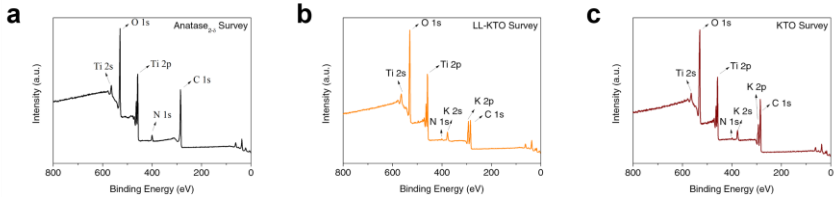

Figure 5-9 – XPS survey of **a**, Anatase$_{2-\delta}$, **b**, LL-KTO and **c**, KTO. The emergence of both a peak in the K 2s and 2p spectra at 387 and 293 eV, respectively, as compared to Anatase$_{2-\delta}$ indicates K is indeed introduced into the titania system.

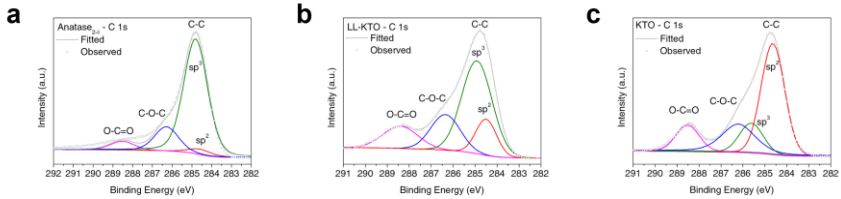

Figure 5-10 – XPS spectra of **a**, Anatase$_{2-\delta}$, **b**, LL-KTO and **c**, KTO for C 1s.

Table 5-4 – Area ratio of different types of carbon bonding in Anatase$_{2-\delta}$, LL-KTO and KTO.

Samples	O-C=O	C-O-C	sp^3	sp^2
Anatase$_{2-\delta}$	5.7%	15.8%	75.04%	3.5%
LL-KTO	14.4%	19.4%	52.3%	13.9%
KTO	12.1%	21.9%	13.8%	52.1%

Combing the findings from the presented characterisation results, two potassium layered titanates with distinctive structures were prepared: 1.) LL-KTO had an

assumingly “loose” layered titanate structure and less conductive CNFs. 2.) KTO had an allegedly more rigid layered structure and a more conductive CNF. They had similar CNFs-to-titanates ratio at about 1-to-3. It would be interesting to know which material works better, kinetically and thermodynamically, as an electrode for KIBs. If they both stored ions via intercalation, KTO seemed to be a better electrode due to the higher conductivity of its electron pathway[311,312]. However, if LL-KTO stored ions via stacked ↔ sliced structural transformation that avoids the drawbacks of the intercalation mechanism, the results may show be reversed.

§ 5.3. Coin cell assembly and disassembly

The electrochemical properties of LL-KTO and KTO were studied as positive electrodes with respect to K at a potential window of 0.01 - 2.5 V vs K/K^+.

Electrochemical tests were carried out using two-electrode coin cells, CR2032, which were assembled in an Ar-filled glovebox with oxygen and moisture concentrations kept below 0.1 ppm. Working electrodes were fabricated by coating slurries that contain active materials onto aluminium current collectors. These slurries were made by mixing LL-KTO and KTO with PVDF at a weight ratio of 85:15 in NMP. The working electrodes were dried thoroughly at 80 °C under vacuum. Potassium foil flattened from potassium ingot was used as counter electrodes and separated from the working electrode using a glass microfiber filter (Whatman, GF/D). The electrolyte used was 0.8M KPF_6 in a 1:1 (v/v) mixture of ethylene carbonate (EC) and diethyl carbonate (DEC) for KIBs.

To understand the storing mechanism process during the electrochemical reactions, coin cells at various charging and discharging cycles were dissembled in the Ar-filled glove box to recover the active materials. The active materials were washed with DME to remove the residues and scraped off from the current collector. The collected materials were studied using TEM for both imaging and SAED. XPS analysis was conducted to study the valance state of titanium.

§ 5.4. Results and discussion

Results from testing over 1,800 cycles of LL-KTO and KTO are shown in Figure 5-11. For LL-KTO, at current densities of 100 and 500 mA g^{-1}, reversible capacities of 201 and 183 mAh g^{-1} were maintained, respectively (Figure 5-11a,b). At the same rates, the reversible capacities for KTO after 1,800 cycles were only 104 and 34 mAh g^{-1}, respectively. Rate cyclabilities for both samples were further performed. LL-KTO had reversible capacities of 209, 181, 164 and 134 mAh g^{-1} at distinct current densities and a recovery rate of 94.7% (198 mAh g^{-1}) when the current density was decreased. As for KTO, it has reversible capacities of 86, 66, 51 and 41 mAh g^{-1} and a recovery rate of 93.7% (81 mAh g^{-1}) when the current density was reduced. It is obvious LL-KTO performs much better than KTO. These capacities of LL-KTO and KTO correspond up to approximately 0.62 and 0.36 K^+ per transition metal (TM). LL-KTO achieved an improvement from 160% compared with reported potassium titanates in which only 0.14~0.38 K^+/TM are stored[150–154], while KTO was similar to these results.

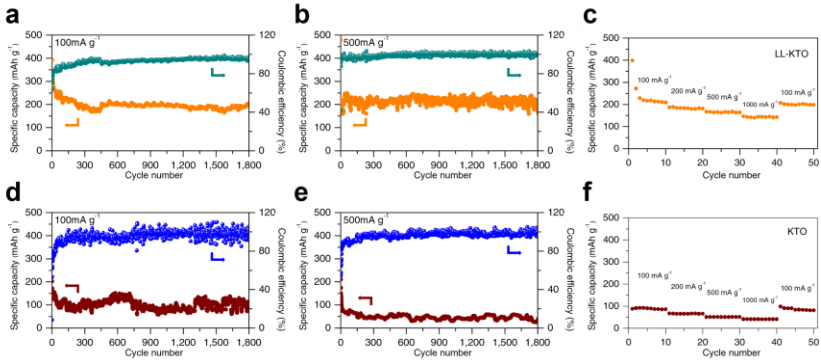

Figure 5-11 – Cycling performance comparison at current densities of 100 and 500 mA g^{-1} and rate performance starting with a current density of 100 mA g^{-1}, then increase step wise to 200, 500 and 1,000 mA g^{-1} and a drop back to 100 mA g^{-1} at the end. 10 cycles ran for each current density. **a-c**, LL-KTO and **d-f**, KTO.

The capabilities of LL-KTO and KTO were further compared with representative titanium-oxide based KIBs, NIBs and LIBs (Figure 5-12). While most KIBs are in the

low-performance corner on the chart, LL-KTO outperforms NIBs and is comparable to the best LIBs. KTO, on the other hand, has electrochemical performances like other conventional titanates.

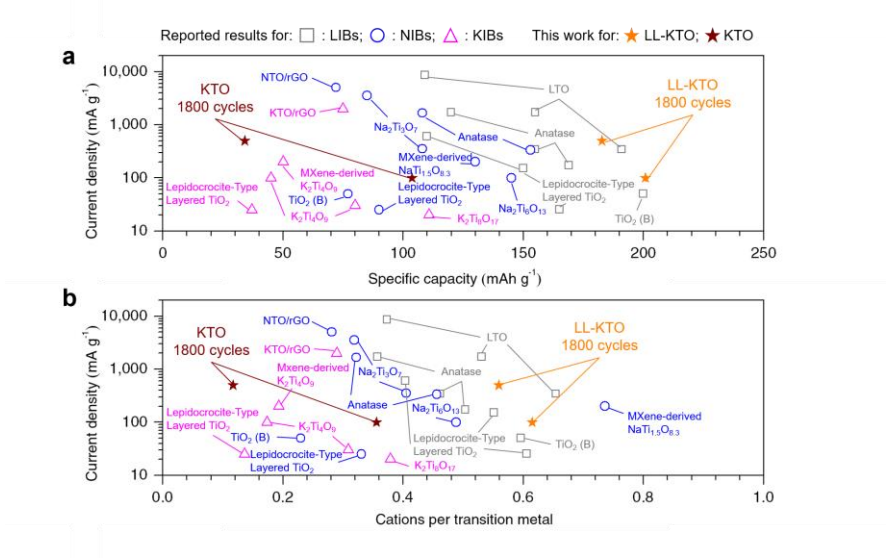

Figure 5-12 – Performance comparison of LL-KTO and KTO with other titanium oxide-based materials for KIBs[150–154], NIBs[150–152,156–159] and LIBs[148–150,161,162]. (Grey: LIBs; Blue: NIBs; Pink: KIBs; Orange: KIBs with LL-KTO; Brown: KIBs with KTO). **a**, Specific capacity comparison. **b**, Number of cations stored per transition metal comparison. See Table 5-5 for expanded data sheet including reported electrode materials and references.

Table 5-5 – Long cycle performance and number of cations stored per transition metal.

Systems	Materials	Cycling capacity (mAh g^{-1}) / Current density (mA g^{-1}) / Cycle number	Cations per TM	Ref.
Ours	LL-KTO	201 / 100 / 1800	0.62	This work
		183 / 500 / 1800	0.56	
	KTO	104 / 100 / 1800	0.36	
		34 / 500 / 1800	0.12	

KIBs	Potassium titanate /rGO	75 / 2000 / 2000	0.29	[152]
	MXene-derived $K_2Ti_4O_9$	50 / 200 / 900	0.19	[151]
	$K_2Ti_4O_9$	80 / 30 / 30	0.31	[153]
		45 / 100 / 10	0.17	
	$K_2Ti_8O_{17}$	110.7 / 20 / 50	0.38	[154]
	Lepidocrocite-Type Layered TiO_2	37 / 25 / 45	0.14	[150]
NIBs	Sodium titanate/rGO	72 / 5000 / 10000	0.28	[152]
	MXene-derived $NaTi_{1.5}O_{8.3}$	130 / 200 / 150	0.74	[151]
	Lepidocrocite-Type Layered TiO_2	90 / 25 / 45	0.33	[150]
	$Na_2Ti_6O_{13}$	145 / 100 / 200	0.49	[158]
	Anatase	153 / 335 / 1000	0.46	[157]
		108 / 1675 / 1000	0.32	
	$Na_2Ti_3O_7$	108 / 354 / 1200	0.41	[159]
		85 / 3540 / 10000	0.32	
	TiO_2 (B)	77 / 50 /100	0.23	[156]
LIBs	Lepidocrocite-Type Layered TiO_2	165 / 25 / 45	0.61	[150]
		150 / 150 / 50	0.55	[149]
		110 / 600 / 50	0.40	
	LTO	191 / 340/ 15	0.65	[148]
		155 / 1700 / 150	0.53	
	TiO_2 (B)	200 / 50 / 100	0.60	[162]
	Anatase	169 / 170 / 100	0.50	[161]
		155 / 340 / 100	0.46	
		120 / 1700 / 100	0.36	

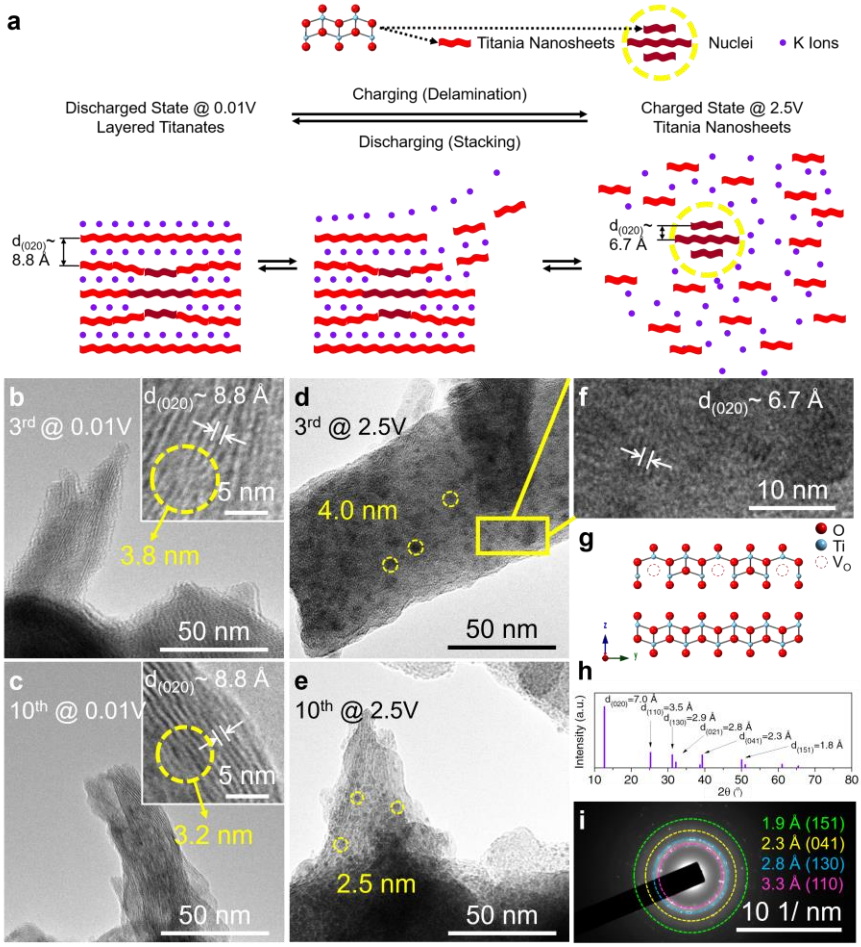

Figure 5-13 – Investigation of the potassium-storing mechanism of LL-KTO. **a**, Conceptual representations of titania nanosheets, nuclei and K and schematic illustration of "stacked ↔ sliced structural transformation". **b-e**, *Ex situ* TEM images at 3rd and 10th cycle. In the discharged state (**b**,**c**), the laminar structure was observed, with nuclei circled in yellow in the inset. In the charged state (**d**,**e**), isolated nuclei (nanodots) were observed. **f-i**, Structures of nuclei. Experimental results: higher magnification view (**f**) of image (**d**) shows the nuclei with

laminar structure. SAED patterns (**i**) from the experimental observation. Calculated results: simulated structure (**g**) and the corresponding XRD patterns (**h**).

To review the reason on why LL-KTO performed so much better than other titanates used in KIBs, structural analysis of discharged and charged LL-KTO after the 3rd and 10th cycles were studied using *ex situ* TEM and selected area electron diffraction (SAED) (Figure 5-13). Figure 5-13b-e show that most of the laminar structure from the discharged state was converted to nanodots upon charging, with these nanodots reverting to the laminar structure upon discharging. These nanodots shared a similar laminar structure to LL-KTO but a smaller d-spacing of 6.7 Å which was because of the absence of K^+ and OH^- ions (Figure 5-13f). An oxygen deficient lepidocrocite-type layered titania was constructed as an evidence (Figure 5-13g). This structure had a (020) d-spacings of 7.0 Å and characteristic crystal planes (110), (130), (041) and (151) that matched the experimental TEM and SAED (Figure 5-13f-i). These nanodots were believed to be nuclei for the growth of the surrounding LL-KTO, shown as low-contrast areas (lattice mismatch) circled in yellow in the insets of Figure 5-13b,c. They were presence in both charged and discharged state. These observations of the preservation of titania nuclei and the reversible assembly of the laminar LL-KTO indicated a potassium-storing mechanism different from intercalation: instead of a rigid intercalation host, LL-KTO went through complete structural transformation.

The designation "stacked ↔ sliced structural transformation" is herein proposed as illustrated in Figure 5-13a. During charging, the repulsion force gradually delaminates the layered titanates into titania nanosheets as K^+ ions leave the structure. Some of the titania nanosheets self-aggregates through interlayer attractions and forms nuclei that appear as nanodots[313]. In the subsequent discharging process, potassium is stored onto titania nanosheets through liquid-diffusion while they stack back layer-by-layer into layered titanates[282] around the nuclei. In short, potassium is stored between the titania nanosheets through a stacked ↔ sliced structural transformation. The absence of a plateau (monotonic voltage decay) in the discharge-charge curve of the 3rd and 10th cycle (Figure 5-14) suggested a two-phase electrochemical reaction since there was a smooth variation of the chemical potential of potassium as the titania nanosheets transform into layered titanates. The process could be described as a continuous

growth of discharged materials into a larger laminar structure until all the active material was consumed.

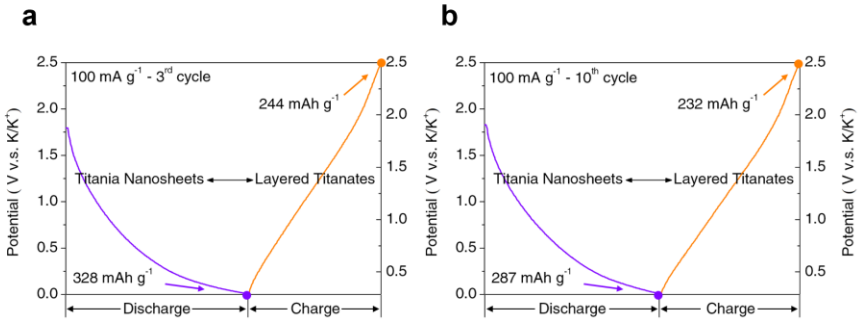

Figure 5-14 – Discharge-charge curve of LL-KTO at **a**, 3rd and **b**, 10th cycle. Current density of 100 mA g^{-1}. The discharge capacities at 3rd and 10th cycle are 328 and 287 mAh g^{-1}, respectively.

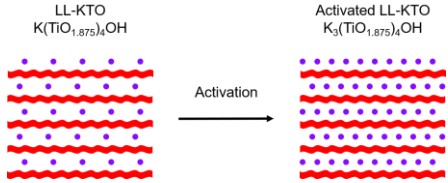

Figure 5-15 – Schematic illustrations of activation of LL-KTO.

Although the storing mechanism for LL-KTO was different from intercalation, this had not yet suggested why it achieved much higher capacity than KTO and other titanates. One of the contributing factors had been deduced as an activation discharge before cycling. During which, the electrodes were activated by electrochemically inserting extra potassium into the laminar structure to form $K_3(TiO_{1.875})_4OH$ (Equation 5-2 and Figure 5-15).

$$K(TiO_{1.875})_4OH + 2K^+ + 2e^- \rightarrow K_3(TiO_{1.875})_4OH \quad \text{Equation 5-2}$$

During cycling, the valence state of Ti would change between III and IV. The Ti^{IV}/Ti^{III} single redox couple was confirmed by *ex situ* XPS analysis as shown in Figure 5-16. The

peaks at the binding energy of 458.8 and 464.4 eV at charge state were attributed to the Ti^{IV} 2p 3/2 and Ti^{IV} 2p 1/2, respectively. At discharged stage, chemical shifts of the binding energy for Ti^{IV} 2p 3/2 and Ti^{IV} 2p 1/2 were observed and moved to 458.6 and 464.2 eV. Two new peaks were observed at the binding energy of 457.8 and 462.8 eV for Ti^{III} 2p 3/2 and Ti^{III} 2p 1/2, respectively.

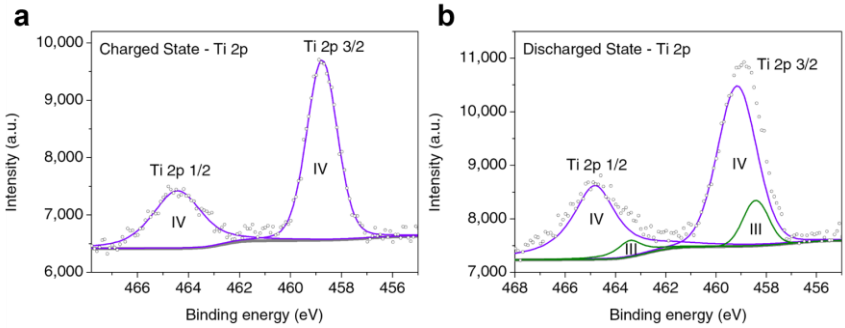

Figure 5-16 – *Ex situ* XPS spectra of LL-KTO for Ti 2p at charged and discharged state. **a,** Charged state. **b,** Discharged state.

Taken all the experimental evidence together, the overall reaction is shown in Equation 5-3.

$$n[(TiO_{1.875})_4{\cdot}OH + 3K^+ + 3e^-] \leftrightarrow n[K_3(TiO_{1.875})_4OH] \quad \text{Equation 5-3}$$

There are two advantages of stacked ↔ sliced structural transformation over intercalation: 1.) More accessible storage sites since K^+ ions are stored on the entire surface of titania nanosheets through surface reaction during stacking and therefore prevent slow solid-diffusion. More K^+ ions are stored because of the energy barrier for surface reaction being much lower than diffusion. 2.) Net-zero structural deterioration as evidenced by the similar interlayer spacing of pristine LL-KTO and 3rd and 10th discharged state (Figure 5-1g and Figure 5-13b,c). These advantages both directly derive from the stacking potassium-storing dynamics. To the best of our knowledge, this is the first time a stacked ↔ sliced structural transformation is achieved through an electrochemical process.

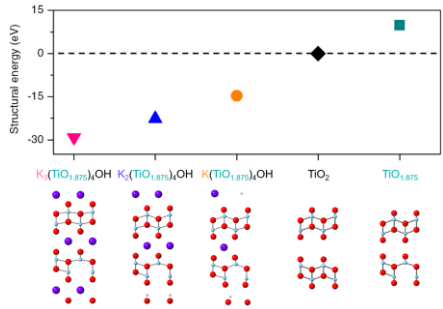

Figure 5-17 – Structural energy of various stages between charge and discharge state. **Top**: DFT calculated structural energy of various lepidocrocite-type layered titanates against stoichiometric lepidocrocite-type layered TiO_2. **Bottom:** from left to right, corresponding structural representations of lepidocrocite-type layered $K_3(TiO_{1.875})_4OH$, $K_2(TiO_{1.875})_4OH$, $K(TiO_{1.875})_4OH$, TiO_2 and $TiO_{1.875}$. Stoichiometric layered TiO_2 is used as a reference to define the zero-energy level. Stability of stoichiometric layered TiO_2 was confirmed by a previous report[284]. Systems with energies above 0 eV are unstable.

To understand the energetics of stacked ↔ sliced structural transformation, DFT calculations were used to compare structural energies of five lepidocrocite-type layered structures at different charging stages: $K_3(TiO_{1.875})_4OH$ (discharged state for LL-KTO), $K_2(TiO_{1.875})_4OH$, $K(TiO_{1.875})_4OH$, TiO_2 and $TiO_{1.875}$ (charged state for LL-KTO). They have structural energies of –29.1, –22.6, –14.7, 0.0 and 9.9 eV, respectively. From the calculations, a single oxygen vacancy had an energy of ~10 eV. Figure 5-17 shows positive structural energy of layered $TiO_{1.875}$ as compared to TiO_2, which meant that oxygen vacancy made the structure metastable, and therefore susceptible to delamination that could be stabilised as nanosheets or nanodots (the nuclei). On the other hand, the increase of K^+ ions concentration in the titanate structures resulted in more negative structural energy (vs TiO_2); this suggested the K^+ ions could stabilise the laminar structure. This calculation demonstrated that the interplay of oxygen vacancy and K^+ ions were crucial to the stacked ↔ sliced structural transformation of LL-KTO.

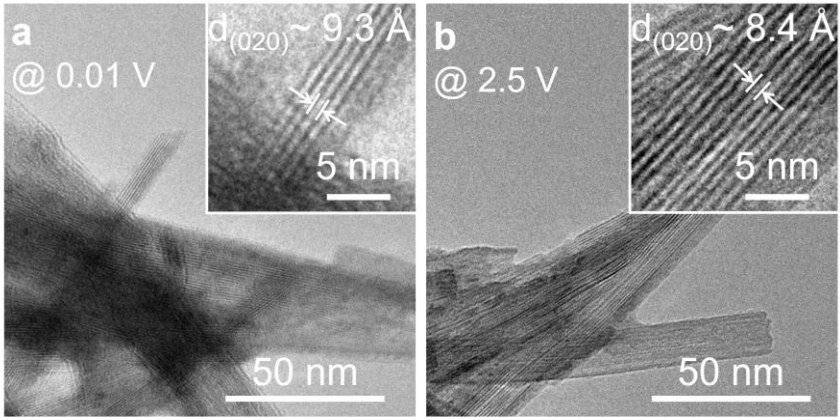

Figure 5-18 – *Ex situ* TEM analysis of KTO at discharged and charged state. **a,** Discharged sate showing laminar structure with d-spacing of 9.3 Å. **b,** Charged sate showing laminar structure with d-spacing of 8.4 Å.

In contrast to the structural transformation mechanism of LL-KTO, structural analysis by *ex situ* TEM images showed intercalation took place for KTO (Figure 5-18). The laminar structure was observed in both charge and discharge state without any nanodots (titania nuclei). Furthermore, the increase in d-spacing after discharging (8.4 to 9.3 Å) indicated the intercalation of K^+ ions into the laminar structure. Without oxygen deficiency, KTO could not be delaminated upon complete removal of potassium in the charged state (stoichiometric TiO_2) as suggested by the calculations in Figure 5-17. As a result, its electrochemical performances were like other conventional potassium titanates (Figure 5-12).

To elucidate the nature of stacked ↔ sliced structural transformation, a plot correlating Peukert's constant (k), fractal dimension (d) and inverse of cations per transition metal (r) is presented in Figure 5-19. Peukert's law describes the inverse dependence of capacity (C) and discharge current (I) of an energy storage system with a formula, CI^k=constant[268]. When k is at two extremes, 0 and 1, a system shows ideal surface-control and diffusion-control behaviour, respectively. The Peukert's constant has its physical origin from electrode fractality, that is characterised by fractal dimension

d=k+2[268]. When d is 2 and 3, pure 2D and 3D nature of electrode structures are implied respectively. By investigating the storing mechanism of KIBs, NIBs and LIBs based on host-guest paradigm, we found the inverse of cations per transition metal is a useful governing index to characterise the chemistry of capacity. With r=1, a single host transition metal ion can accommodate one alkali cation, the theoretical limit for single-electron redox couple (r=0.5 for double-electron redox couple). Figure 5-19b shows LL-KTO (k=0.16, d=2.16, r=1.61) clustered with NIBs and LIBs electrodes and pushed the kinetic boundary (k=0, d=2) and approached the thermodynamic limit (r=1). KTO (k=0.32, d=2.32, r=3.45) was again on the corner of poor performance Figure 5-19c.

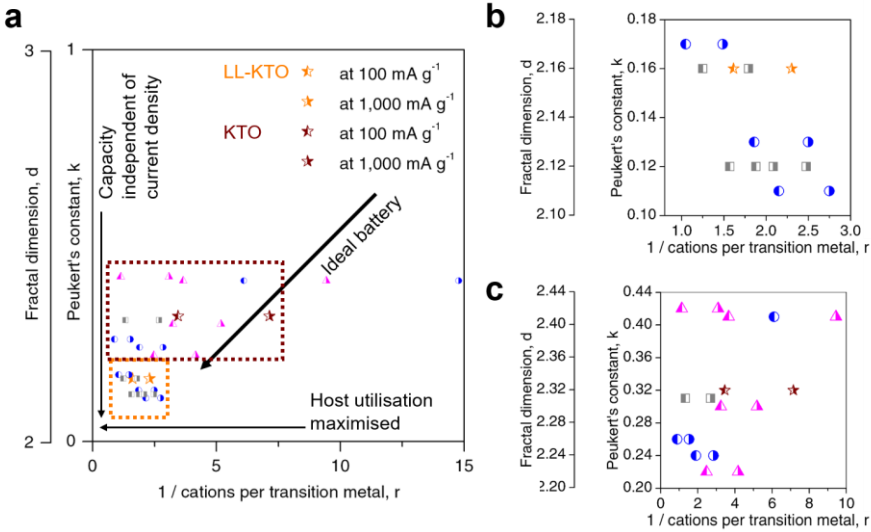

Figure 5-19 – Plot of Peukert's constant (k), fractal dimension (d) and inverse of cations per transition metal (r) to compare LL-KTO and KTO with other electrodes in KIBs[150–154], NIBs[150–152,156–159] and LIBs[148–150,161,162]. (Left filled symbols: data at 100 mA g^{-1}; Right filled symbols: data at 1,000 mA g^{-1}) See expanded dataset including reported electrode materials and references in Table 5-6 and Table 5-7. **a**, Overall comparison. **b**, Enlarged area of orange square for a closer look on LL-KTO. **c**, Enlarged area of brown square for a closer look on KTO.

Table 5-6 – Rate performance.

Systems	Materials	Rate capacities (mAh g^{-1}) / Current density (mA g^{-1})	Ref.
Ours	LL-KTO	207-180-163-142 / 100-200-500-1000	This work
	KTO	86-66-51-41 / 100-200-500-1000	
KIBs	Potassium titanate /rGO	228-162-116-84 / 100-200-500-1000	[152]
	MXene-derived $K_2Ti_4O_9$	150-119-105-97-89-81 / 20-50-100-150-200-300	[151]
	$K_2Ti_4O_9$	97-80-65-56-50-42-20 / 30-100-250-500-1000-1500-2000	[153]
	$K_2Ti_8O_{17}$	175-105-90-80-75-60-50-40 / 20-40-80-100-150-200-400-500	[154]
NIBs	Sodium titanate/rGO	302-226-197-174-147-127-97 / 100-200-500-1000-2000-3000-5000	[152]
	MXene-derived $NaTi_{1.5}O_{8.3}$	196-169-153-134-119-109-101 / 50-100-200-500-1000-1500-2000	[151]
	$Na_2Ti_6O_{13}$	160-145-133-123-119 / 100-200-400-800-1000	[158]
	Anatase	180-177-174-158-132-108-84-68-52 / 34-85-170-340-850-1700-3400-5100-8500	[157]
	$Na_2Ti_3O_7$	108-100-90-85 / 354-885-1770-3540	[159]
	TiO_2 (B)	77-55-42-33 / 50-100-200-400	[156]
LIBs	Lepidocrocite-Type Layered TiO_2	170-150-130-110 / 20-150-300-600	[149]
	LTO	191-170-135-125 / 340-850-3400-5100	[148]
	TiO_2 (B)	200-155-125-100-85 / 200-500-1000-2000-3000	[162]
	Anatase	224-192-170-150 / 85-170-850-1700	[161]

Table 5-7 – Peukert's constant (k), fractal dimension (d) and inverse of cations per transition metal (r) at 100 and 1,000 mA g^{-1} based on Table 5-6 using Peukert's law[268].

Systems	Materials	k	d	Cations/TM at 100 mA g^{-1}	r at 100 mA g^{-1}	Cations/TM at 1000 mA g^{-1}	r at 1000 mA g^{-1}	Ref.
Ours	LL-KTO	0.16	2.16	0.62	1.61	0.43	2.30	This work
	KTO	0.32	2.32	0.29	3.45	0.14	7.14	
KIBs	Potassium titanate /rGO	0.42	2.42	0.88	1.14	0.32	3.09	[152]
	MXene-derived $K_2Ti_4O_9$	0.22	2.22	0.41	2.47	0.24	4.16	[151]
	$K_2Ti_4O_9$	0.30	2.30	0.31	3.24	0.19	5.18	[153]
	$K_2Ti_8O_{17}$	0.41	2.41	0.27	3.66	0.11	9.44	[154]
NIBs	Sodium titanate /rGO	0.26	2.26	1.13	0.88	0.65	1.53	[152]
	MXene-derived $NaTi_{1.5}O_{8.3}$	0.17	2.17	0.96	1.05	0.67	1.48	[151]
	$Na_2Ti_6O_{13}$	0.13	2.13	0.54	1.86	0.40	2.50	[158]
	Anatase	0.24	2.24	0.53	1.90	0.35	2.84	[157]
	$Na_2Ti_3O_7$	0.11	2.11	0.47	2.15	0.36	2.75	[159]
	TiO_2 (B)	0.41	2.41	0.16	6.10	0.07	14.78	[156]
LIBs	Lepidocrocite-Type Layered TiO_2	0.12	2.12	0.53	1.88	0.40	2.47	[149]
	LTO	0.16	2.16	0.80	1.25	0.56	1.79	[148]
	TiO_2 (B)	0.31	2.31	0.75	1.33	0.37	2.68	[162]
	Anatase	0.12	2.12	0.64	1.57	0.48	2.08	[161]

§ 5.5. Conclusions

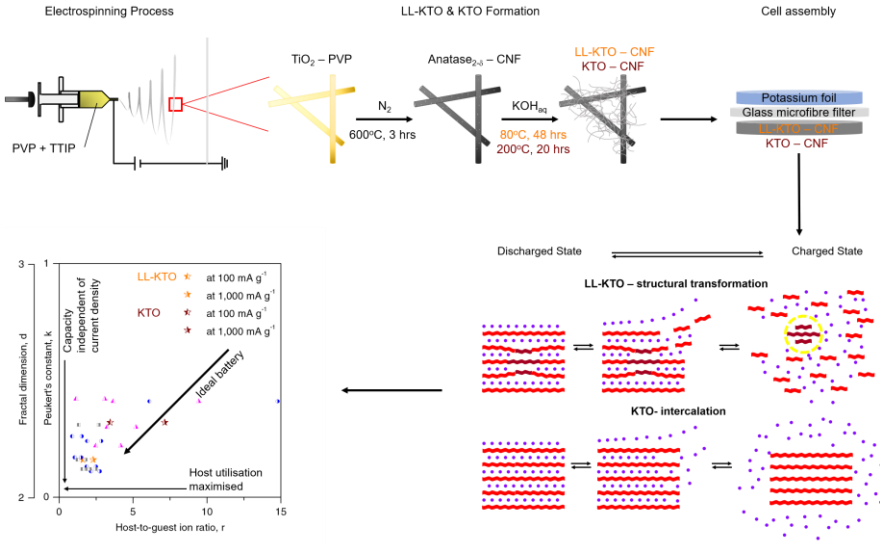

Figure 5-20 – Image summary. From the synthesis of LL-KTO and KTO to their ion storing mechanism and results.

In this chapter, the disadvantages of large ion storage were addressed and a new ion storing mechanism "stacked ↔ sliced structural transformation" was developed. It can achieve large storage of K^+ ions with net-zero structural deterioration in cycling that effectively overcomes the disadvantage of large K^+ ions. LL-KTO was synthesised using a low temperature and pressure chemical bath to demonstrate this mechanism. Direct evidence presented using high resolution imaging and structural analysis that unlike a rigid intercalation host, LL-KTO delaminated and restacked with K^+ ions upon charging and discharging. Furthermore, the oxygen vacancies - purposely introduced - allow layered titania to delaminate under strong electrostatic interaction and thus lowering the energy barrier. As a result, a high reversible specific capacity of 201 mAh g^{-1} after 1,800 cycles at a current density of 100 mA g^{-1} was achieved, comparable to values for titanium-oxide based LIBs. This capacity corresponded up to an average of

0.62 K^+/TM, an improvement from 160% compared with other potassium titanates. Making KIBs with good specific capacity and stability on par with LIBs is challenging, nevertheless, on top of achieving that, an entirely new mechanism with net-zero structural deterioration was demonstrated. LL-KTO is by far the highest capacity KIBs electrode reported for titanate materials and potentially may have future application prospect in the low-cost grid-scale energy storage or long-life power supply.

Furthermore, new matrices, Peukert's constant, fractal dimension and inverse of cations per transition metal, correlating structure, chemistry and performance were suggested to evaluate electrodes across different systems that can serve as future guidance to develop ion batteries and storing mechanisms. These findings showed that LL-KTO pushed the kinetic boundary and approached the thermodynamic limit.

The demonstrated reversible structural control not only provides an important guide to design future energy storage systems but may also encourage considerable research attention in other fields, such as environmental remediation, catalysis and sensors.

Chapter 6

Stacked ↔ Sliced Structural Transformation in Sodium Storage?

Similar to potassium-ion batteries (KIBs), sodium-ion batteries (NIBs) are promising substitutes for lithium-ion batteries (LIBs) as well[314]. However, unlike lithium and potassium, sodium does not intercalate easily with graphite material[191,201], therefore anodes with materials other than carbon are essential for NIBs. Furthermore, similar K^+ ions, Na^+ ions with size 1.02 Å are also larger than Li^+. Storing them through intercalation might pulverised electrodes after long cycles.

Here, a layered sodium titanate synthesised at low temperature and pressure, L-NTO, was used as NIBs anode to examine whether stacked ↔ sliced structural transformation could be applied to sodium storing. If this were observed, a non-carbon anode with the ability to store a large amount of sodium with net-zero structural deterioration could be realised. Unfortunately, L-NTO did not store Na^+ ions via the newly discovered mechanism as suggested by the low performance it delivered. A reversible capacity of only 156 mAh g^{-1} at 100 mA g^{-1} was recorded after 500 cycles. This was worse than the performance of LL-KTO in KIBs. L-NTO was further applied as the intercalating anode for KIBs and showed worse results than LL-KTO in KIBs as well. In short, L-NTO as intercalation anodes for both NIBs and KIBs had capacitates lower than LL-KTO in KIBs. This suggested stacked ↔ sliced structural transformation was a more suitable mechanism than intercalation for large K^+ ion storage but was not observed in storing Na^+ ions.

C-Y.L., Y.L., W.W. and R.V.K. conceptualised the study. C-Y.L. designed and performed the experiments. C-Y.L. analysed and interpreted data. G.D. contributed to the TEM

acquisition. W.W. and Q.Y. supervised and J.H. performed the electrochemical testing and *ex situ* studies.

§ 6.1. Introduction

In Chapter 5, a new ion storing mechanism based on reversible delamination and stacking of 2D titanate nanosheets for K^+ ions was reported. Here, sodium titanates made from both low and high temperature/pressure, indexed L-NTO and H-NTO, were prepared to study whether a similar mechanism can be found for sodium storage.

§ 6.2. Materials synthesis and characterisation

Using the same precursor, L-NTO and H-NTO were prepared by chemically reacting $Anatase_{2-\delta}$ with 5M $NaOH_{aq}$. The reaction took place in a Teflon container in an oven at 80 °C for 48 hours and in a Teflon-lined autoclave in a furnace at 160 °C for 20 hours for L-NTO and H-NTO, respectively. Both samples were washed with ethanol to remove excess $NaOH_{aq}$ and are dried at 80 °C overnight.

The morphologies of L-NTO and H-NTO were examined with SEM at different magnifications (Figure 6-1). Different from the nanofibres of potassium titanates seen in Figure 5-1, these sodium titanates were ribbon-like. SEM and TEM images (Figure 6-2a,c) validated these nanoribbons had a width from 5 to 60 nm and thickness of few nm. The enlarged TEM images of L-NTO and H-NTO showed both materials had laminar structures with interlayer spacing of 8.5 and 7.2 Å, respectively. Similarly, these layered materials were confirmed by XRD patterns (Figure 6-3). Both materials showed well-developed (020) peaks at 9.6° and 9.0° that reflected the laminar structure[282]. Furthermore, the in-plane structure of titanates was indicated by the peaks at 24° and 28°. The XRD patterns were well indexed to layered $Na_2Ti_2O_4(OH)_2$ (00-57-0123). From the elemental mappings in Figure 6-2b, d, Na, Ti and O were distributed mainly on the nanoribbons while C was only visualised on the backbone. The presence of these elements was also disclosed by XPS survey with C 1s, Ti 2p, Na 1s, O 1s and Ti 2s signals at 285, 464, 495, 530 and 565 eV, respectively (Figure 6-4a,d).

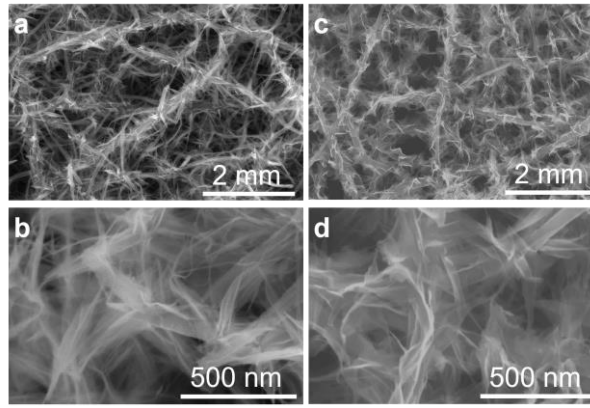

Figure 6-1 – SEM images of titanates prepared at low and high temperature/pressure. **a,b**, L-NTO. **c,d**, H-NTO.

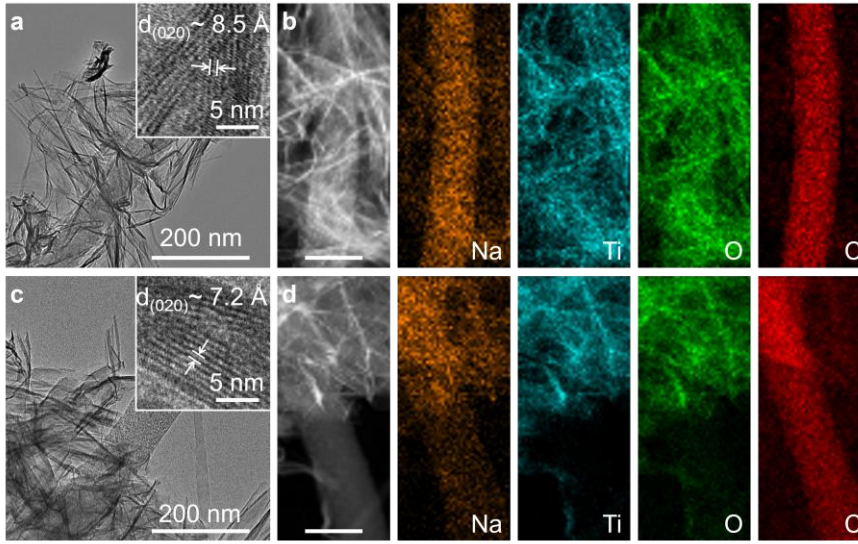

Figure 6-2 – Morphology and chemical distributions of titanates prepared at low and high temperature/pressure. TEM and STEM images and EDS elemental mapping of **a,b**, L-NTO

and **c,d,** H-NTO. The insets of **(a)** and **(c)** show the laminar structure and interlayer spacing of L-NTO and H-NTO. The scale bar in elemental mapping for all four is 100 nm.

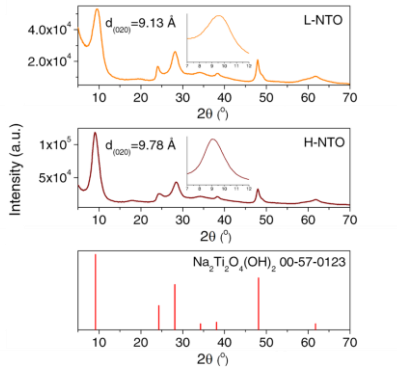

Figure 6-3 – XRD profiles of **top:** L-NTO, **middle:** H-NTO and **bottom:** reference.

The chemical and physical properties of carbon in both materials were examined using XPS, Raman spectroscopy and TGA. In the XPS C 1s and the deconvoluted spectra (Figure 6-4c,f), O-C=O, C-O-C, sp^3 and sp^2 bonds of carbon were revealed. The nature of these bonds was explained in detail in § 5.2. Materials synthesis and characterisation. Like the KOH_{aq} treatment, more intense reactions with $NaOH_{aq}$ induced by higher temperature/pressure has transformed the CNFs in $Anatase_{2-\delta}$ to a more conducting form with a greater content of sp^2 bonding (Table 6-1) at the expense of sp^3 bonding. Nevertheless, while L-NTO had similar content of sp^2 as compared to LL-KTO, H-NTO did not have sp^2 content as high as KTO even though the reaction conditions were the same.

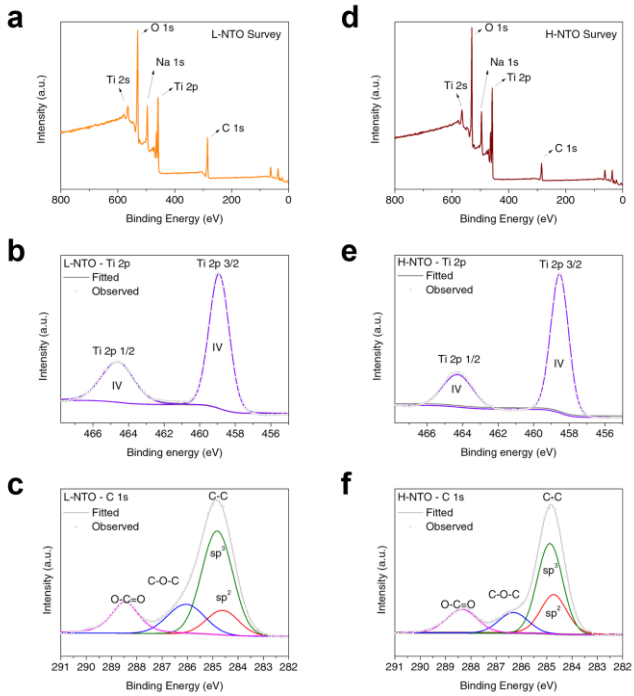

Figure 6-4 – XPS spectra of **a-c**, L-NTO and **d-f**, H-NTO. **a,d**, Survey of the binding energy from 0 to 800 eV. **b,e**, Binding energy of Ti 2p. **c,f**, Binding energy of C 1s and deconvolution of the bands showing the binding nature.

Table 6-1 – Area ratio of different types of carbon bonding in L-NTO and H-NTO.

Samples	O-C=O	C-O-C	sp^3	sp^2
L-NTO	16.6%	17.7%	52.7%	13.0%
H-NTO	15.7%	12.7%	48.3%	23.2%

Raman spectroscopy was used to study the nature of C-C bonding. In Figure 6-5, the deconvoluted wavelength spectrum between 1000 to 1800 cm^{-1} was shown. The bonding nature of D, A and G band was explained in § 5.2. Materials synthesis and characterisation. The proportion of each type of carbon are summarised in Table 6-2. Similar to the results for KOH_{aq} treatment (Table 5-4), more intense reaction will lead

to more transformation of A band carbon into D and G band carbon. This suggested the $NaOH_{aq}$ treatment also reconfigured some of the dangling sp^3 bonds (dominates A band) into sp^2 bonds (dominates D and G band).

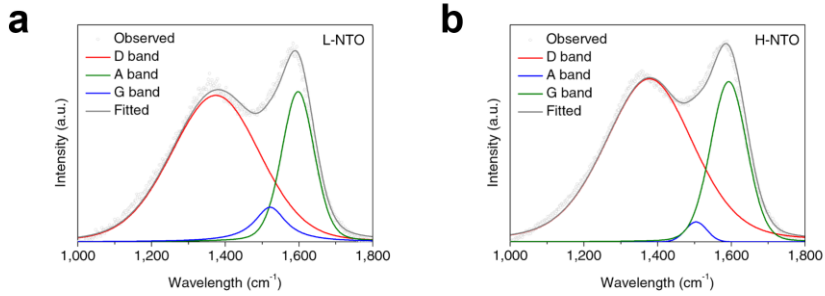

Figure 6-5 – Raman spectroscopy for **a**, L-NTO and **b**, H-NTO from 1000 to 1800 cm^{-1}. The curves are deconvoluted into D band, A band and G band.

Table 6-2 – Area ratio of different types of carbon band in L-NTO and H-NTO.

Samples	D Band	A band	G Band
L-NTO	65.8%	7.6%	26.6%
H-NTO	69.5%	2.0%	28.5%

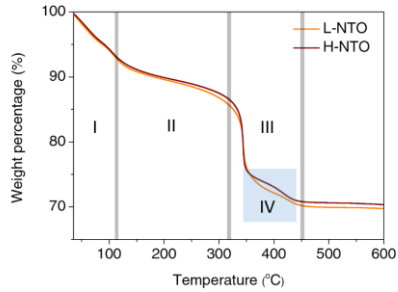

Figure 6-6 – TGA analysis of L-NTO and H-NTO in air up to 600 °C at a ramping rate of 10 °C per minute.

Table 6-3 – Estimated percentages of CNFs in L-NTO and H-NTO.

Samples	CNFs	Titania/titanates
L-NTO	18.2 wt%	81.8 wt%
H-NTO	17.7 wt%	82.3 wt%

Proportions of CNFs in L-NTO and H-NTO were determined using TGA. Similar to potassium titanates in Chapter *5*, there were 4 regions of weight drop that can be observed from the TGA curves (Figure 6-6). Region I represented the immediate weight loss of water molecules adsorbed on the surface. Region II was an extension where adsorbed water was continued to be released from the pores. The gas adsorption-desorption analysis of L-NTO showed it having a majority of the mesopores (Figure 6-7). In the third region between ~320 and 450 °C, a rapid drop in weight indicates carbon combustion. Within this region, a separate reaction indicated by the blue box was happening, the oxidation of sodium-titanates. Since there was this inevitable side reaction in oxygen, it was impossible to calculate the exact CNFs weight percentage, rather an estimated ratio being calculated and present in Table 6-3.

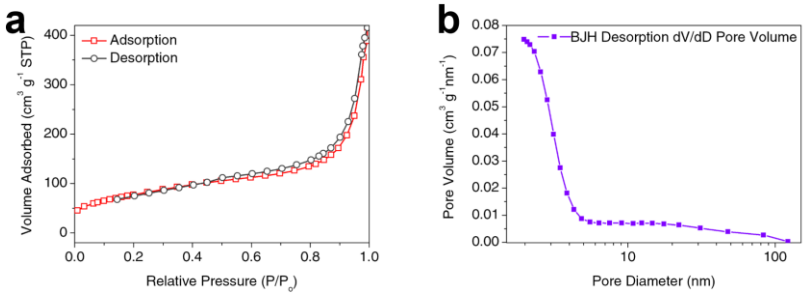

Figure 6-7 – Nitrogen adsorption-desorption analysis of L-NTO. **a**, isotherm and **b**, pore size distribution.

The atomic ratios collected from the EDS and XPS are listed in Table 6-4. Based on these ratios, the fact that only Ti^{IV} was present in both L-NTO and H-NTO (Figure 6-4b,e) and the XRD patterns being indexed to $Na_2Ti_2O_4(OH)_2$, the chemical formula of the two sodium-titanate could be written as $Na_{2-x}Ti_2O_4(OH)_{2-x}$. The value x represented the sodium deficiency presented in both L-NTO and H-NTO.

Table 6-4 – Elemental ratio of Na, Ti and O collected from EDS and XPS.

	EDS			XPS		
Samples	Na	Ti	O	Na	Ti	O
L-NTO	12.4%	17.2%	70.4%	15.4%	24.1%	60.5%
H-NTO	12.4%	18.8%	68.8%	14.8%	27.3%	57.9%

§ 6.3. Coin cell assembly

The electrochemical properties of L-NTO were studied as potential positive electrodes with respect to K at a potential window of 0.01 - 2.5 V vs K/K^+ in the first part and respect to Na at a potential window of 0.01 - 2.5 V vs Na/Na^+ in the second part. Applying L-NTO as an electrode for potassium storage was to compare its performance with LL-KTO since they were both prepared at low temperature/pressure. The second part was to examine whether the newly discovered "stacked ↔ sliced structural transformation" can be found in sodium storage as well.

Electrochemical tests were carried out using two-electrode coin cells, CR2032, which were assembled in an Ar-filled glovebox with oxygen and moisture concentrations kept below 0.1 ppm. Working electrodes were fabricated by coating slurries that contain active materials onto aluminium current collectors. These slurries were made by mixing as-prepared materials with PVDF at a weight ratio of 85:15 in NMP. The working electrodes were dried thoroughly at 80 °C under vacuum. Potassium (or sodium) foil flattened from potassium (or sodium) ingot was used as counter electrodes and separated from the working electrode using a glass microfiber filter (Whatman, GF/D). The electrolyte used is 0.8M KPF_6 (or 1M $NaPF_6$) in a 1:1 (v/v) mixture of EC and DEC for KIBs (or NIBs).

§ 6.4. Results and discussion

L-NTO was first examined as KIBs anode. It's cycling performances at different current densities were shown in Figure 6-8a-c. At 100 mA g^{-1}, it had an initial discharge capacity of 300 mAh g^{-1} and dropped rapidly to 168 mAh g^{-1} at the 10^{th} cycle. Afterwards, the capacity decays at a very low rate of 0.076% per cycle to a reversible capacity of 105 mAh g^{-1} at 500^{th} cycles. The capacities decay per cycle at 500 and 1,000 mA g^{-1} from 10^{th} to 500^{th} cycle were 0.087% and 0.081%, respectively, similar to that of at 100 mA g^{-}

[1]. The cycle stabilities were able to be extended 3,000 and 5,000 cycles for capacity decays of 0.018% and 0.015% per cycle, respectively. At the end of the thousands of cycles, the reversible capacities were 59 and 41 mAh g^{-1}. Rate capabilities of L-NTO were displayed in Figure 6-8d. The discharge capacities at the end of the 10th cycle for each current density from 50, 100, 200, 500 to 1,000 mA g^{-1} were 159, 132, 113, 91 and 76 mAh g^{-1}, respectively, before the discharging rate dropped to 50 mA g^{-1} with a recovered capacity of 125 mAh g^{-1} (79% recovery).

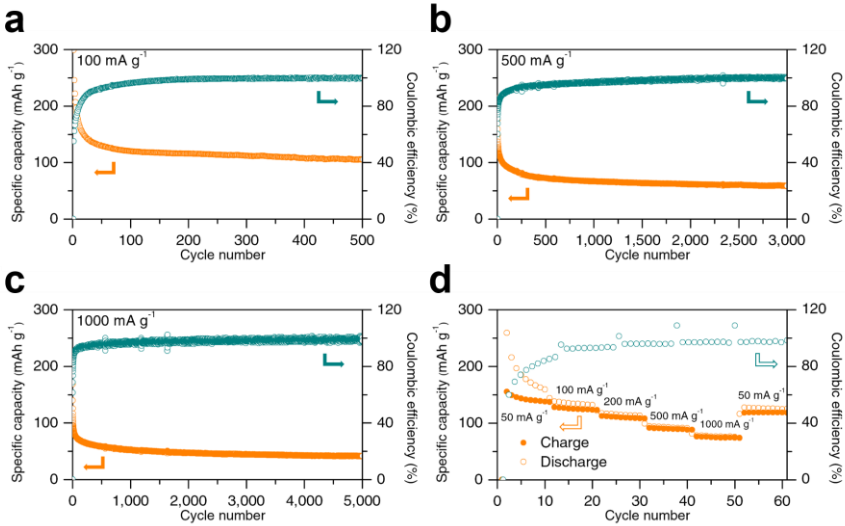

Figure 6-8 – Cycling performance of L-NTO in KIBs at current densities of **a**, 100, b, 500 and **c**, 1,000 mA g^{-1} and **d**, rate performance starting with current density of 50 mA g^{-1}, then increase step wise to 100, 200, 500 and 1,000 mA g^{-1} and a drop back to 50 mA g^{-1} at the end. 10 cycles ran for each current density.

Regardless of the larger interlayer spacing of L-NTO as compared to LL-KTO, its specific capacities and cyclabilities were worse than that of LL-KTO (Figure 5-11a-c). This again proves that "stacked ↔ sliced structural transformation" seems to be a more suitable storing mechanism for large K^+ ions.

When L-NTO was applied to NIBs, it showed better electrochemical performances in terms of capacity, stability and cycle life as compared to when it was an electrode for KIBs (Figure 6-9). At 100, 500 and 1,000 mA g^{-1}, it achieved reversible capacities of 156, 113 and 115 mAh g^{-1}, respectively, after 500 cycles. The long cycle stabilities were shown as well. From 10 to 3,000 cycles at 500 mA g^{-1}, the capacity decayed 0.012% per cycle; and from 10 to 5,000 cycles at 1,000 mA g^{-1}, the capacity decayed 0.006% per cycle. At the end of the thousands of cycles, the reversible capacities were 96 and 103 mAh g^{-1}, respectively. In terms of rate capabilities (Figure 6-9d), L-NTO in NIBS had discharge a capacity retention rate of 97%, much higher when it was a KIBs anode (79%).

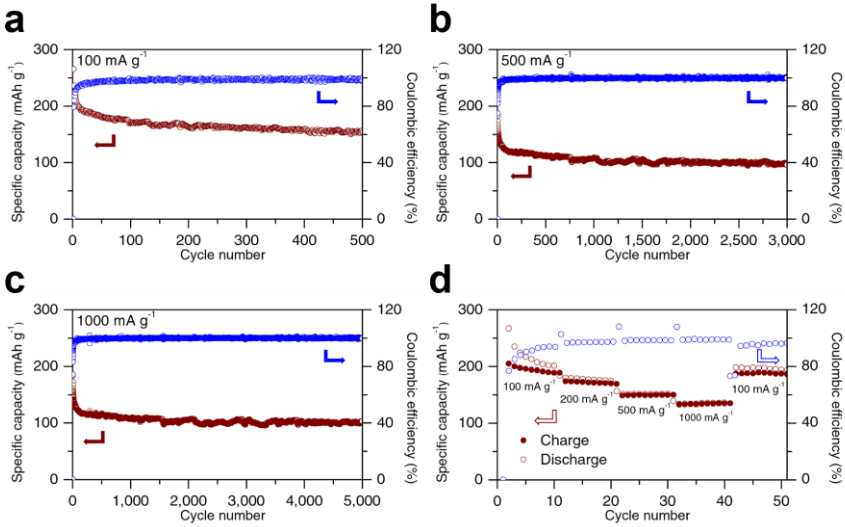

Figure 6-9 – Cycling performance of L-NTO in NIBs at current densities of **a**, 100, b, 500 and **c**, 1,000 mA g^{-1} and **d**, rate performance starting with current density of 100 mA g^{-1}, then increase step wise to 200, 500 and 1,000 mA g^{-1} and a drop back to 100 mA g^{-1} at the end. 10 cycles ran for each current density.

Below, the electrochemical performances of L-NTO in KIBs and NIBs were compared to with representative titanium-oxide based KIBs, NIBs and LIBs using the standard

current density vs. capacity comparison and the "Peukert's constant (k), fractal dimension (d) and inverse of cations per transition metal (r)" comparison.

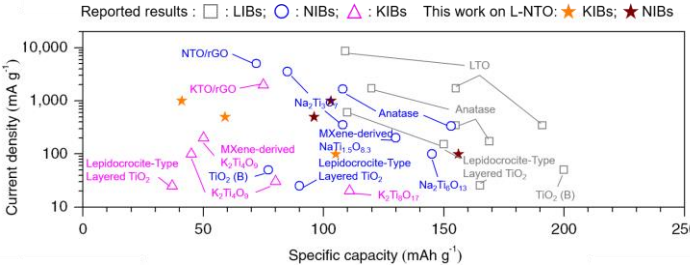

Figure 6-10 – Specific capacity comparison of L-NTO as electrode for KIBs and NIBs with other titanium oxide-based materials for KIBs[150–154], NIBs[150–152,156–159] and LIBs[148–150,161,162]. (Grey: LIBs; Blue: NIBs; Pink: KIBs; Orange: KIBs with L-NTO; Brown: NIBs with L-NTO). See Table 6-*5* for expanded data sheet for L-NTO.

When L-NTO was applied as an electrode for KIBs, the results fall into the regions where other KIBs were. Although, it still showed better results due to the lighter weight of sodium titanates as compared to potassium titanates (sodium weight less than potassium) that were used in the selected literature. L-NTO showed average performance as NIBs anode when it was compared to other NIBs electrodes. This suggested L-NTO did not store sodium via "stacked ↔ sliced structural transformation", otherwise, the performance would have been much better. Instead, same as all the other layered titanates, L-NTO could only store sodium via intercalation mechanism.

Table 6-*5* – Long cycle performance and number of cations stored per transition metal.

Systems	Materials	Cycling capacity (mAh g^{-1}) / Current density (mA g^{-1}) / Cycle number
KIBs	L-NTO	105 / 100 / 500 59 / 500 / 3000 41 / 1000 / 5000
NIBs	L-NTO	156 / 100 / 500 96 / 500 / 3000 103 / 1000 / 5000

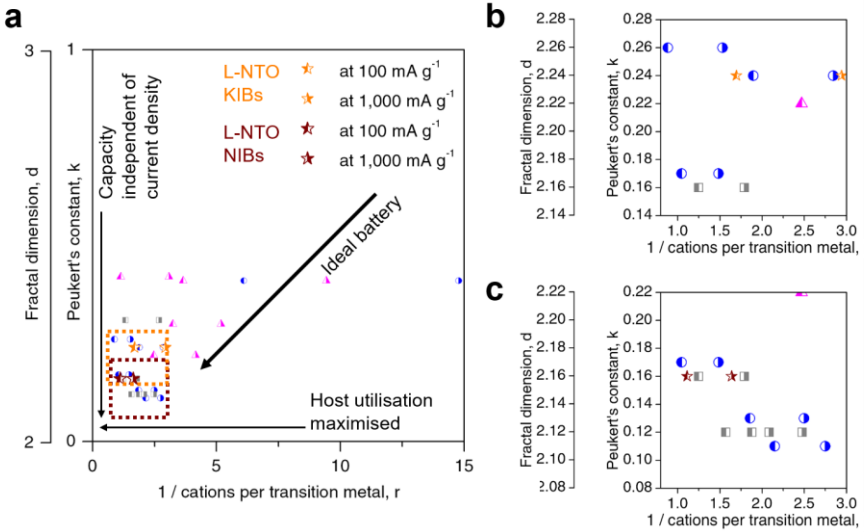

Figure 6-11 – Plot of Peukert's constant (k), fractal dimension (d) and inverse of cations per transition metal (r) to compare L-NTO as electrode for KIBs and NIBs with other electrodes in KIBs[150–154], NIBs[150–152,156–159] and LIBs[148–150,161,162]. (Left filled symbols: data at 100 mA g^{-1}; Right filled symbols: data at 1,000 mA g^{-1}) See expanded dataset for L-NTO in Table 6-6 and Table 6-7. **a**, Overall comparison. **b**, Enlarged area of orange square for a closer look on L-NTO as an electrode for KIBs. **c**, Enlarged area of brown square for a closer look on L-NTO as an electrode for NIBs.

A plot correlating Peukert's constant (k), fractal dimension (d) and inverse of cations per transition metal (r) in Figure 6-11 was presented for L-NTO as KIBs and NIBs electrode. Figure 6-11a,b showed L-NTO in KIBs (k=0.24, d=2.24, r=1.69) was closer to the ideal battery as compared to other KIBs. This coincided with the superior capacity performance shown in Figure 6-10. Furthermore, in Figure 6-11c, L-NTO as NIBs electrode (k=0.16, d=2.16, r=1.11) clustered with other NIBs and LIBs. Although it pushed the kinetic boundary (k=0, d=2) and approached the thermodynamic limit (r=1), the performances were not outstanding.

Table 6-6 – Rate performances.

Systems	Materials	Cycling capacity (mAh g^{-1}) / Current density (mA g^{-1}) / Cycle number
KIBs	L-NTO	159-132-113-91-76 / 50-100-200-500-1000
NIBs	L-NTO	201-175-152-136 / 100-200-500-1000

Table 6-7 – Peukert's constant (k), fractal dimension (d) and inverse of cations per transition metal (r) at 100 and 1,000 mA g^{-1} based on Table 6-6 using Peukert's law[268].

Systems	Materials	Cycling capacity (mAh g^{-1}) / Current density (mA g^{-1}) / Cycle number
KIBs	L-NTO	159-132-113-91-76 / 50-100-200-500-1000
NIBs	L-NTO	201-175-152-136 / 100-200-500-1000

Table 6-8 – Peukert's constant (k), fractal dimension (d) and inverse of cations per transition metal (r) at 100 and 1,000 mA g-1 based on Supplementary Table 2 using Peukert's law[268].

Systems	Materials	k	d	Cations/TM at 100 mA g^{-1}	r at 100 mA g^{-1}	Cations/TM at 1000 mA g^{-1}	r at 1000 mA g^{-1}
KIBs	L-NTO	0.24	2.24	0.59	1.69	0.34	2.94
NIBs	L-NTO	0.16	2.16	0.90	1.11	0.61	1.64

§ 6.5. Conclusions

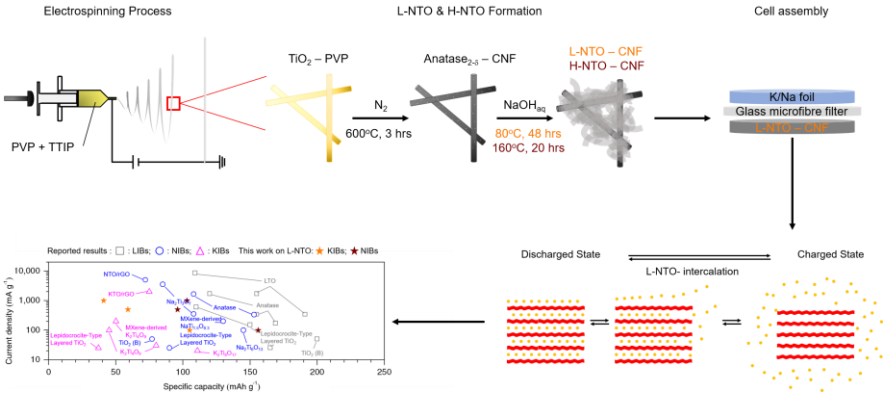

Figure 6-12 – Image summary. From the synthesis of L-NTO and H-NTO to the ion storing mechanism and results.

In this chapter, two layered sodium titanates, L-NTO and H-NTO were prepared at low and high temperature/pressure chemical reaction, respectively. Both titanates had chemical compositions and formulas of $Na_{2-x}Ti_2O_4(OH)_{2-x}$ as deduced from XRD, EDS, XPS and TGA. L-NTO was examined to find evidence for "stacked ↔ sliced structural transformation" mechanism for electrochemical sodium storing but failed.

L-NTO was first used as the intercalating KIBs electrode as a direct comparison to LL-KTO. Based on the Peukert's constant (k), fractal dimension (d) and inverse of cations per transition metal (r) parameter, LL-KTO with (k=0.16, d=2.16, r=1.61) was superior to L-NTO (k=0.24, d=2.24, r=1.69) regardless of the larger interlayer spacing and the smaller molar mass of L-NTO. This proved that "stacked ↔ sliced structural transformation" mechanism was a better ion storage mechanism than intercalation chemistry.

In the next part, L-NTO was used as the NIBs electrode to examine whether "stacked ↔ sliced structural transformation" mechanism could be observed for sodium storing. Nevertheless, as deduced by the average electrochemical performance as compared to

other titanates in the literature, there seems to be no evidence of "stacked ↔ sliced structural transformation" mechanism for sodium storing using L-NTO.

Although L-NTO did not have surprisingly good electrochemical properties. It showed long life cycles with small capacity decay. In KIBs, at current density of 500 and 1,000 mA g^{-1}, the capacity decays per cycle were 0.018% and 0.015% from 10-to-3,000 cycles and 10-to-5,000 cycles, respectively. In NIBs, it performed better with only 0.012% and 0.006% capacity decay per cycle at 500 and 1,000 mA g^{-1} after 3,000 and 5,000 cycles, respectively.

In short, the "stacked ↔ sliced structural transformation" mechanism was not been found in sodium storing with low temperature/pressure synthesised L-NTO, nevertheless, it was still a moderate electrode material.

Chapter 7

Conclusions

This chapter summarises the overall conclusions of the research conducted in this dissertation on the topic of *"Beyond lithium-ion technology: lithium-sulfur and potassium-ion for better and cheaper batteries",*

- A flexible carbon nanofibre interlayer with highly mounted TiO_2 polysulfide anchors (TiO_2-CNF interlayer) was prepared by electrospinning of a polymer precursor followed by pyrolysis. TiO_2 nanoparticles were *in situ* integrated onto the carbon nanofibre. The combined chemical and physical adsorption properties from TiO_2 and carbon nanofibre, respectively, effectively mitigate the polysulfides dissolution and shuttling as evidenced by SEM, theoretical calculations and electrochemical performance. As a result, the TiO_2-CNF interlayer increased initial discharge capacity by 46%, prolonged the cycle life with 25% more capacity retention at the end of 300 cycles and improved the average Coulombic efficiency by 5% as compared to the cell without interlayer (calculated based on sulfur mass). This proved that an extra interlayer between sulfur cathode and separator can bring positive outcome to the performance of LSBs. In reality, however, the weight penalty by the extra layer must be taken into account, which can be a disadvantage in the first few cycles. Furthermore, TiO_2 may cause too strong an attraction to sulfur species causing locking and unlocking instability. The TiO_2-CNF composite interlayer herald a single-step approach to structural design chemi-/physisorptive interlayers for advanced LSBs. Light weighting the interlayer will be the future direction to further develop high energy density and high stability LSBs.

- A loose-layered titanate (LL-KTO) was prepared by low temperature chemical bath between oxygen deficient anatase nanoparticles and KOH_{aq}. With this unique loose-structural designed material, a new ion storing mechanism to compete for the structural deterioration caused by K^+ ions cycling in and out of the electrode material is developed. To name it "stacked ↔ sliced structural transformation". It can store a large amount of K^+ ions in the electrode with net-zero structural deterioration during cycling. As a result, it achieved a capacity corresponds up to an average of 0.62 K^+/TM, an improvement from 160% compared with other potassium titanates. Making KIBs with good specific capacity and stability on par with LIBs. Direct evidence from TEM showed that unlike a rigid intercalation host, LL-KTO delaminates and restacks with K^+ ions upon charging and discharging. A phenomenon never reported before. Furthermore, new matrices, Peukert's constant, fractal dimension and inverse of cations per transition metal, correlating structure, chemistry and performance are suggested to evaluate electrodes across different systems that can serve as future guidance to develop ion batteries and storing mechanisms. LL-KTO pushes the kinetic boundary and approaches the thermodynamic limit. The work on reversible structural control provides an important guide to design future energy storages. Preparing materials with similar properties will be essential to establish a sound and clear theory for this new mechanism. Most importantly, this suggested us to think outside the box while designing electrode materials for KSBs where volume expansion will be a tricky challenge as well.
- A sodium titanates, L-NTO, prepared at low temperature/pressure was used as an anode for NIBs to examine whether sodium could be stored via "stacked ↔ sliced structural transformation". The normal electrochemical performance, however, did not suggest that. Storing mechanism for L-NTO was intercalation, similar to other reported sodium titanates. L-NTO was also employed as the intercalating anode for KIBs to compare its performance with the LL-KTO. The results showed LL-KTO had better performance, in terms capacity, cycle stability and reversibility. The superior performance of LL-KTO suggested "stacked ↔ sliced structural transformation" mechanism to be a more suitable ion storage mechanism for large ions as compared to intercalation.

Chapter 8

Future Work

This final chapter outlines the future direction on designing KSBs based on the research work carried out in this PhD. KSBs have the advantage of both high energy density and low cost. They, however, share the same drawbacks of both sulfur-based and potassium-based electrochemistry. Fortunately, many fundamental ideas have been tested on LSBs and KIBs in this PhD. A clear roadmap for KSBs development is suggested as follows:

1. Finding a sweet spot to balance the effect and weight of interlayer:
   To compensate for the reverse effect on overall capacity caused by the heavy TiO_2-CNF interlayer, TiO_2 will be replaced with lighter MgO or SiO_2 subjects to whether these oxides can be integrated *in situ* with CNF via electrospinning technique. The weight ratio between the oxides and CNF and the weight ratio between interlayer and cathode will be tuned to determine a sweet spot to maximise the chemical adsorption ability of the interlayer and minimise the weight effect and the locking effect.
2. Completing the new ion storing mechanism:
   To establish the newly discovered "stacked ↔ sliced structural transformation" ion storing mechanism, loose-layered manganate, niobate and vanadate will be synthesised to examine whether the same electrochemistry behaviour can be found on these similarly structured materials. Furthermore, *in situ* characterisation techniques and theoretical calculations will be combined to analyse correlations between the structural change and energy state during cycling.
3. Synthesising suitable cathodes (sulfur host) for KSBs:

To prepare KSBs cathodes, amorphous-like porous carbon will be the starting material. Although K^+ and Li^+ ions have similar chemistry, the size difference makes their storing mechanism completely different. While crystal structures with high rigidity and crystallinity may enhance the performance of LIBs or LSBs, the same approach does not work for KIBs or KSBs. Structures with high enough flexibility and tolerance are required. They need to be able to shape shift when ions are stored and released to ensure minimal structural deterioration during a full discharge-charge cycle. This is an essential requirement for longer battery life.

4. Testing KSBs with the interlayer-cathode couple:
   To achieve the best possible performance of KSBs, an interlayer will be incorporated to mitigate the inevitable polysulfide dissolution and migration. Here, the oxide-carbon interlayer developed during LSBs research will be applied. While some fine tuning of the oxide content may be required, the interlayer-cathode couple is believed to be a promising development direction to achieve low cost KSBs with high energy density and long cycle life for large-scale energy storage.
5. Replacing potassium metal anode in KSBs:
   To ensure the safety of KSBs, it is necessarily to replace the explosive and reactive potassium metal with a safer anode. LL-KTO is a promising material since it is a non-explosive oxide. Furthermore, its net-zero structural deterioration will be suitable for long cycle life expected in KSBs. Finally, the capacity can be boosted by replacing the heavy titanate with lighter manganate or silicate.

References

1. van Ruijven, B. J., De Cian, E. & Sue Wing, I. Amplification of future energy demand growth due to climate change. *Nat. Commun.* **10**, 2762 (2019).
2. Hernandez, R. R. *et al.* Techno–ecological synergies of solar energy for global sustainability. *Nat. Sustain.* **2**, 560–568 (2019).
3. Bogdanov, D. *et al.* Radical transformation pathway towards sustainable electricity via evolutionary steps. *Nat. Commun.* **10**, 1077 (2019).
4. Fares, R. L. & Webber, M. E. The impacts of storing solar energy in the home to reduce reliance on the utility. *Nat. Energy* **2**, 17001 (2017).
5. Armand, M. & Tarascon, J. M. Building better batteries. *Nature* **451**, 652–657 (2008).
6. Dunn, B., Kamath, H. & Tarascon, J.-M. Electrical energy storage for the grid: A battery of choices. *Science (80-.).* **334**, 928–935 (2011).
7. Tarascon, J. M. & Armand, M. Issues and challenges facing rechargeable lithium batteries. *Nature* **414**, 359–367 (2001).
8. Palacin, M. R. Recent advances in rechargeable battery materials: a chemist's perspective. *Chem. Soc. Rev.* **38**, 2565–2575 (2009).
9. Goodenough, J. B. & Kim, Y. Challenges for rechargeable Li batteries. *Chem. Mater.* **22**, 587–603 (2010).
10. Goodenough, J. B. & Park, K.-S. The Li-ion rechargeable battery: A perspective. *J. Am. Chem. Soc.* **135**, 1167–1176 (2013).
11. Nitta, N., Wu, F., Lee, J. T. & Yushin, G. Li-ion battery materials: Present

and future. *Mater. Today* **18**, 252–264 (2015).

12. Choi, J. W. & Aurbach, D. Promise and reality of post-lithium-ion batteries with high energy densities. *Nat. Rev. Mater.* **1**, 16013 (2016).

13. Seh, Z. W., Sun, Y., Zhang, Q. & Cui, Y. Designing high-energy lithium-sulfur batteries. *Chem. Soc. Rev.* **45**, 5605–5634 (2016).

14. Manthiram, A., Chung, S.-H. & Zu, C. Lithium–sulfur batteries: Progress and prospects. *Adv. Mater.* **27**, 1980–2006 (2015).

15. Evers, S. & Nazar, L. F. New approaches for high energy density lithium–sulfur battery cathodes. *Acc. Chem. Res.* **46**, 1135–1143 (2013).

16. Chen, R., Zhao, T. & Wu, F. From a historic review to horizons beyond: lithium-sulphur batteries run on the wheels. *Chem. Commun.* **51**, 18–33 (2015).

17. Pramudita, J. C., Sehrawat, D., Goonetilleke, D. & Sharma, N. An initial review of the status of electrode materials for potassium-ion batteries. *Adv. Energy Mater.* **7**, 1602911 (2017).

18. Hwang, J.-Y., Myung, S.-T. & Sun, Y.-K. Recent progress in rechargeable potassium batteries. *Adv. Funct. Mater.* **28**, 1802938 (2018).

19. Rand, D. A. J. A journey on the electrochemical road to sustainability. *J. Solid State Electrochem.* **15**, 1579–1622 (2011).

20. Armand, M. B. & Steele, B. C. H. *Fast Ion Transport in Solids*. (North-Holland Amsterdam, 1973).

21. Mizushima, K., Jones, P. C., Wiseman, P. J. & Goodenough, J. B. Li_xCoO_2 (0<x<-1): A new cathode material for batteries of high energy density. *Mater. Res. Bull.* **15**, 783–789 (1980).

22. Mohri, M. *et al.* Rechargeable lithium battery based on pyrolytic carbon as a negative electrode. *J. Power Sources* **26**, 545–551 (1989).

23. Rozier, P. & Tarascon, J. M. Review—Li-rich layered oxide cathodes for

next-generation Li-ion batteries: Chances and challenges. *J. Electrochem. Soc.* **162**, A2490–A2499 (2015).

24. Amatucci, G. G., Tarascon, J. M. & Klein, L. C. CoO_2, the end member of the $LixCoO_2$ solid solution. *J. Electrochem. Soc.* **143**, 1114–1123 (1996).

25. Reimers, J. N. & Dahn, J. R. Electrochemical and in situ x-ray diffraction studies of lithium intercalation in Lix CoO_2. *J. Electrochem. Soc.* **139**, 2091–2097 (1992).

26. Yamada, S., Fujiwara, M. & Kanda, M. Synthesis and properties of $LiNiO_2$ as cathode material for secondary batteries. *J. Power Sources* **54**, 209–213 (1995).

27. Rougier, A., Gravereau, P. & Delmas, C. Optimization of the composition of the $Li_{1-z}Ni_{1+z}O_2$ electrode materials: Structural, magnetic, and electrochemical studies. *J. Electrochem. Soc.* **143**, 1168–1175 (1996).

28. Arai, H., Okada, S., Sakurai, Y. & Yamaki, J. Thermal behavior of $Li_{1-y}NiO_2$ and the decomposition mechanism. *Solid State Ionics* **109**, 295–302 (1998).

29. Armstrong, A. R. & Bruce, P. G. Synthesis of layered $LiMnO_2$ as an electrode for rechargeable lithium batteries. *Nature* **381**, 499 (1996).

30. Gu, M. *et al.* Formation of the spinel phase in the layered composite cathode used in Li-ion batteries. *ACS Nano* **7**, 760–767 (2013).

31. Ma, X., Chen, H. & Ceder, G. Electrochemical properties of monoclinic $NaMnO_2$. *J. Electrochem. Soc.* **158**, A1307–A1312 (2011).

32. B., A. & J., P. Novel lithium-ion cathode materials based on layered manganese oxides. *Adv. Mater.* **13**, 943–956 (2001).

33. Yabuuchi, N. & Ohzuku, T. Novel lithium insertion material of $LiCo_{1/3}Ni_{1/3}Mn_{1/3}O_2$ for advanced lithium-ion batteries. *J. Power Sources* **119–121**, 171–174 (2003).

34. Zhuang, G. V *et al.* Li_2CO_3 in $LiNi_{0.8}Co_{0.15}Al_{0.05}O_2$ cathodes and its effects on capacity and power. *J. Power Sources* **134**, 293–297 (2004).

35. Delmas, C., Saadoune, I. & Rougier, A. The cycling properties of the $Li_xNi_{1-y}Co_yO_2$ electrode. *J. Power Sources* **44**, 595–602 (1993).

36. Chen, C. H. *et al.* Aluminum-doped lithium nickel cobalt oxide electrodes for high-power lithium-ion batteries. *J. Power Sources* **128**, 278–285 (2004).

37. Olivetti, E. A., Ceder, G., Gaustad, G. G. & Fu, X. Lithium-Ion Battery Supply Chain Considerations: Analysis of Potential Bottlenecks in Critical Metals. *Joule* **1**, 229–243 (2017).

38. Yamada, A., Chung, S. C. & Hinokuma, K. Optimized $LiFePO_4$ for lithium battery cathodes. *J. Electrochem. Soc.* **148**, A224–A229 (2001).

39. Whittingham, M. S. Lithium batteries and cathode materials. *Chem. Rev.* **104**, 4271–4302 (2004).

40. von Hagen, R., Lorrmann, H., Möller, K.-C. & Mathur, S. Electrospun $LiFe_{1-y}MnyPO_4$/C nanofiber composites as self-supporting cathodes in Li-ion batteries. *Adv. Energy Mater.* **2**, 553–559 (2012).

41. Lloris, J. M., Pérez Vicente, C. & Tirado, J. L. Improvement of the electrochemical performance of $LiCoPO_4$ 5 V material using a novel synthesis procedure. *Electrochem. Solid-State Lett.* **5**, A234–A237 (2002).

42. Zaghib, K., Simoneau, M., Armand, M. & Gauthier, M. Electrochemical study of $Li_4Ti_5O_{12}$ as negative electrode for Li-ion polymer rechargeable batteries. *J. Power Sources* **81–82**, 300–305 (1999).

43. Wagemaker, M. *et al.* A kinetic two-phase and equilibrium solid solution in spinel $Li_{4+x}Ti_5O_{12}$. *Adv. Mater.* **18**, 3169–3173 (2006).

44. Griffith, K. J., Wiaderek, K. M., Cibin, G., Marbella, L. E. & Grey, C. P. Niobium tungsten oxides for high-rate lithium-ion energy storage. *Nature* **559**, 556–563 (2018).

45. Park, C.-M., Kim, J.-H., Kim, H. & Sohn, H.-J. Li-alloy based anode materials for Li secondary batteries. *Chem. Soc. Rev.* **39**, 3115–3141 (2010).

46. Larcher, D. *et al.* Recent findings and prospects in the field of pure metals

as negative electrodes for Li-ion batteries. *J. Mater. Chem.* **17**, 3759–3772 (2007).

47. Thackeray, M. M., Vaughey, J. T. & Fransson, L. M. L. Recent developments in anode materials for lithium batteries. *JOM* **54**, 20–23 (2002).

48. Zhang, W.-J. A review of the electrochemical performance of alloy anodes for lithium-ion batteries. *J. Power Sources* **196**, 13–24 (2011).

49. Chan, C. K. *et al.* High-performance lithium battery anodes using silicon nanowires. *Nat. Nanotechnol.* **3**, 31 (2007).

50. Wen, C. J. & Huggins, R. A. Chemical diffusion in intermediate phases in the lithium-silicon system. *J. Solid State Chem.* **37**, 271–278 (1981).

51. Goward, G. R., Taylor, N. J., Souza, D. C. S. & Nazar, L. F. The true crystal structure of $Li_{17}M_4$ (M=Ge, Sn, Pb)–revised from $Li_{22}M_5$. *J. Alloys Compd.* **329**, 82–91 (2001).

52. Nelson, P. A. *High-performance batteries for off-peak energy storage and electric-vehicle propulsion*. (1976).

53. Sharma, R. A. & Seefurth, R. N. Thermodynamic properties of the lithium-silicon system. *J. Electrochem. Soc.* **123**, 1763–1768 (1976).

54. Seefurth, R. N. & Sharma, R. A. Investigation of lithium utilization from a lithium-silicon electrode. *J. Electrochem. Soc.* **124**, 1207–1214 (1977).

55. Kasavajjula, U., Wang, C. & Appleby, A. J. Nano- and bulk-silicon-based insertion anodes for lithium-ion secondary cells. *J. Power Sources* **163**, 1003–1039 (2007).

56. Wu, H. & Cui, Y. Designing nanostructured Si anodes for high energy lithium ion batteries. *Nano Today* **7**, 414–429 (2012).

57. Feng, K. *et al.* Ilicon-based anodes for lithium-ion batteries: from fundamentals to practical applications. *Small* **14**, 1702737 (2018).

58. Liu, N. *et al.* A yolk-shell design for stabilized and scalable Li-ion battery alloy anodes. *Nano Lett.* **12**, 3315–3321 (2012).

59. Wu, H. *et al.* Stable cycling of double-walled silicon nanotube battery anodes through solid-electrolyte interphase control. *Nat Nano* **7**, 310–315 (2012).

60. Zhang, W.-M. *et al.* Tin-nanoparticles encapsulated in elastic hollow carbon spheres for high-performance anode material in lithium-ion batteries. *Adv. Mater.* **20**, 1160–1165 (2008).

61. Xu, Y. *et al.* Uniform Nano-Sn/C Composite Anodes for Lithium Ion Batteries. *Nano Lett.* **13**, 470–474 (2013).

62. Wang, G. *et al.* Sn/graphene nanocomposite with 3D architecture for enhanced reversible lithium storage in lithium ion batteries. *J. Mater. Chem.* **19**, 8378–8384 (2009).

63. Chan, C. K., Zhang, X. F. & Cui, Y. High capacity Li ion battery anodes using Ge nanowires. *Nano Lett.* **8**, 307–309 (2008).

64. Liu, X. H. *et al.* Reversible nanopore formation in Ge nanowires during lithiation–delithiation cycling: An in situ transmission electron microscopy study. *Nano Lett.* **11**, 3991–3997 (2011).

65. Obrovac, M. N. & Chevrier, V. L. Alloy negative electrodes for Li-ion batteries. *Chem. Rev.* **114**, 11444–11502 (2014).

66. China battery giant CATL achieves 304Wh/kg in new battery cells. (2019). http://www.chinadaily.com.cn/a/201903/20/WS5c921ba0a3104842260b1a79.html.

67. Wu, F. & Yushin, G. Conversion cathodes for rechargeable lithium and lithium-ion batteries. *Energy Environ. Sci.* **10**, 435–459 (2017).

68. Jordi, C., Laure, M., Dominique, L. & Rosa, P. M. Beyond intercalation-based Li-ion batteries: The state of the art and challenges of electrode materials reacting through conversion reactions. *Adv. Mater.* **22**, E170–

E192 (2010).

69. Poizot, P., Laruelle, S., Grugeon, S., Dupont, L. & Tarascon, J.-M. Nano-sized transition-metal oxides as negative-electrode materials for lithium-ion batteries. *Nature* **407**, 496–499 (2000).

70. Gao, X.-P. & Yang, H.-X. Multi-electron reaction materials for high energy density batteries. *Energy Environ. Sci.* **3**, 174–189 (2010).

71. Badway, F., Cosandey, F., Pereira, N. & Amatucci, G. G. Carbon metal fluoride nanocomposites: High-capacity reversible metal fluoride conversion materials as rechargeable positive electrodes for Li batteries. *J. Electrochem. Soc.* **150**, A1318–A1327 (2003).

72. Ebner, M., Marone, F., Stampanoni, M. & Wood, V. Visualization and quantification of electrochemical and mechanical degradation in Li-ion batteries. *Science (80-.).* **342**, 716–720 (2013).

73. Yu, H.-C. *et al.* Designing the next generation high capacity battery electrodes. *Energy Environ. Sci.* **7**, 1760–1768 (2014).

74. Li, C. *et al.* An $FeF_3{\cdot}0.5H_2O$ polytype: A microporous framework compound with intersecting tunnels for Li and Na batteries. *J. Am. Chem. Soc.* **135**, 11425–11428 (2013).

75. Wang, X. *et al.* Carbon nanotube–CoF_2 multifunctional cathode for lithium ion batteries: Effect of electrolyte on cycle stability. *Small* **11**, 5164–5173 (2015).

76. Kim, S.-W., Seo, D.-H., Gwon, H., Kim, J. & Kang, K. Fabrication of FeF_3 nanoflowers on CNT branches and their application to high power lithium rechargeable batteries. *Adv. Mater.* **22**, 5260–5264 (2010).

77. Ma, R. *et al.* Large-scale fabrication of graphene-wrapped FeF_3 nanocrystals as cathode materials for lithium ion batteries. *Nanoscale* **5**, 6338–6343 (2013).

78. Luo, Y.-R. *Comprehensive handbook of chemical bond energies*. (CRC Press,

2007).

79. Yu, H.-C., Wang, F., Amatucci, G. G. & Thornton, K. A phase-field model and simulation of kinetically asymmetric ternary conversion-reconversion transformation in battery electrodes. *J. Phase Equilibria Diffus.* **37**, 86–99 (2016).

80. Wang, F. *et al.* Ternary metal fluorides as high-energy cathodes with low cycling hysteresis. *Nat. Commun.* **6**, 6668 (2015).

81. Zhou, Y.-N. *et al.* $FeO_{0.7}F_{1.3}$/C nanocomposite as a high-capacity cathode material for sodium-ion batteries. *Adv. Funct. Mater.* **25**, 696–703 (2015).

82. Shi, Y.-L. *et al.* Electrochemical impedance spectroscopy investigation of the FeF_3/C cathode for lithium-ion batteries. *Solid State Ionics* **222–223**, 23–30 (2012).

83. Hua, X. *et al.* Comprehensive study of the CuF_2 conversion reaction mechanism in a lithium ion battery. *J. Phys. Chem. C* **118**, 15169–15184 (2014).

84. Sun, Y., Liu, N. & Cui, Y. Promises and challenges of nanomaterials for lithium-based rechargeable batteries. *Nat. Energy* **1**, 16071 (2016).

85. Wu, F. *et al.* Lithium iodide as a promising electrolyte additive for lithium–sulfur batteries: mechanisms of performance enhancement. *Adv. Mater.* **27**, 101–108 (2015).

86. Xiong, S., Xie, K., Diao, Y. & Hong, X. Properties of surface film on lithium anode with LiNO3 as lithium salt in electrolyte solution for lithium–sulfur batteries. *Electrochim. Acta* **83**, 78–86 (2012).

87. Gu, W. *et al.* Lithium–iron fluoride battery with in situ surface protection. *Adv. Funct. Mater.* **26**, 1507–1516 (2016).

88. Bruce, P. G., Freunberger, S. A., Hardwick, L. J. & Tarascon, J.-M. Li-O_2 and Li-S batteries with high energy storage. *Nat Mater* **11**, 19–29 (2012).

89. Zhao, Q., Hu, Y., Zhang, K. & Chen, J. Potassium–sulfur batteries: A new

member of room-temperature rechargeable metal–sulfur batteries. *Inorg. Chem.* **53**, 9000–9005 (2014).

90. Lu, X., Bowden, M. E., Sprenkle, V. L. & Liu, J. A low cost, high energy density, and long cycle life potassium–sulfur battery for grid-scale energy storage. *Adv. Mater.* **27**, 5915–5922 (2015).

91. Hwang, J.-Y., Kim, H. M., Yoon, C. S. & Sun, Y.-K. Toward high-safety potassium–sulfur batteries using a potassium polysulfide catholyte and metal-free anode. *ACS Energy Lett.* **3**, 540–541 (2018).

92. Hwang, J.-Y., Kim, H. M. & Sun, Y.-K. High performance potassium–sulfur batteries based on a sulfurized polyacrylonitrile cathode and polyacrylic acid binder. *J. Mater. Chem. A* **6**, 14587–14593 (2018).

93. Xiong, P. *et al.* Room-temperature potassium–sulfur batteries enabled by microporous carbon stabilized small-molecule sulfur cathodes. *ACS Nano* **13**, 2536–2543 (2019).

94. Yang, Y., Zheng, G. & Cui, Y. Nanostructured sulfur cathodes. *Chem. Soc. Rev.* **42**, 3018–3032 (2013).

95. Ji, X., Lee, K. T. & Nazar, L. F. A highly ordered nanostructured carbon-sulphur cathode for lithium-sulphur batteries. *Nat Mater* **8**, 500–506 (2009).

96. Zheng, G., Yang, Y., Cha, J. J., Hong, S. S. & Cui, Y. Hollow carbon nanofiber-encapsulated sulfur cathodes for high specific capacity rechargeable lithium batteries. *Nano Lett.* **11**, 4462–4467 (2011).

97. Han, S.-C. *et al.* Effect of multiwalled carbon nanotubes on electrochemical properties of lithium/sulfur rechargeable batteries. *J. Electrochem. Soc.* **150**, A889–A893 (2003).

98. Yuan, L., Yuan, H., Qiu, X., Chen, L. & Zhu, W. Improvement of cycle property of sulfur-coated multi-walled carbon nanotubes composite cathode for lithium/sulfur batteries. *J. Power Sources* **189**, 1141–1146 (2009).

99. Wang, Z. *et al.* First principles prediction of nitrogen-doped carbon nanotubes as a high-performance cathode for Li-S batteries. *RSC Adv.* **3**, 16775–16780 (2013).

100. Peng, H.-J. *et al.* Strongly coupled interfaces between a heterogeneous carbon host and a sulfur-containing guest for highly stable lithium-sulfur batteries: Mechanistic insight into capacity degradation. *Adv. Mater. Interfaces* **1**, 1400227–1400236 (2014).

101. Chen, R. *et al.* Graphene-based three-dimensional hierarchical dsandwich-type architecture for high-performance Li/S batteries. *Nano Lett.* **13**, 4642–4649 (2013).

102. Du, W.-C. *et al.* Wet chemistry synthesis of multidimensional nanocarbon–sulfur hybrid materials with ultrahigh sulfur loading for lithium–sulfur batteries. *ACS Appl. Mater. Interfaces* **8**, 3584–3590 (2016).

103. Evers, S. & Nazar, L. F. Graphene-enveloped sulfur in a one pot reaction: A cathode with good coulombic efficiency and high practical sulfur content. *Chem. Commun.* **48**, 1233–1235 (2012).

104. Sun, H. *et al.* A composite material of uniformly dispersed sulfur on reduced graphene oxide: Aqueous one-pot synthesis, characterization and excellent performance as the cathode in rechargeable lithium-sulfur batteries. *Nano Res.* **5**, 726–738 (2012).

105. Wang, H. *et al.* Graphene-wrapped sulfur particles as a rechargeable lithium–sulfur battery cathode material with high capacity and cycling stability. *Nano Lett.* **11**, 2644–2647 (2011).

106. Wang, B., Alhassan, S. M. & Pantelides, S. T. Formation of large polysulfide complexes during the lithium-sulfur battery discharge. *Phys. Rev. Appl.* **2**, 34004 (2014).

107. Zu, C. & Manthiram, A. Hydroxylated graphene–sulfur nanocomposites for high-rate lithium–sulfur batteries. *Adv. Energy Mater.* **3**, 1008–1012

(2013).

108. Park, M.-S. *et al.* One-step synthesis of a sulfur-impregnated graphene cathode for lithium-sulfur batteries. *Phys. Chem. Chem. Phys.* **14**, 6796–6804 (2012).

109. Zhang, F., Zhang, X., Dong, Y. & Wang, L. Facile and effective synthesis of reduced graphene oxide encapsulated sulfur via oil/water system for high performance lithium sulfur cells. *J. Mater. Chem.* **22**, 11452–11454 (2012).

110. Song, M.-S. *et al.* Effects of nanosized adsorbing material on electrochemical properties of sulfur cathodes for Li/S secondary batteries. *J. Electrochem. Soc.* **151**, A791–A795 (2004).

111. Wei, S. Z. *et al.* Sulphur–TiO_2 yolk–shell nanoarchitecture with internal void space for long-cycle lithium–sulphur batteries. *Nat Commun* **4**, 1331 (2013).

112. Tao, X. *et al.* Strong sulfur binding with conducting Magnéli-phase TinO2n–1 nanomaterials for improving lithium–sulfur batteries. *Nano Lett.* **14**, 5288–5294 (2014).

113. Liang, X., Garsuch, A. & Nazar, L. F. Sulfur cathodes based on conductive MXene nanosheets for high-performance lithium–sulfur batteries. *Angew. Chemie Int. Ed.* **54**, 3907–3911 (2015).

114. Naoi, K., Kawase, K. & Inoue, Y. A new energy storage material: Organosulfur compounds based on multiple sulfur-sulfur bonds. *J. Electrochem. Soc.* **144**, L170–L172 (1997).

115. Wang, J., Yang, J., Xie, J. & Xu, N. A novel conductive polymer–sulfur composite cathode lithium batteries. *Adv. Mater.* **14**, 963–965 (2002).

116. Wu, F. *et al.* Sulfur/polythiophene with a core/shell structure: Synthesis and electrochemical properties of the cathode for rechargeable lithium batteries. *J. Phys. Chem. C* **115**, 6057–6063 (2011).

117. Zhou, W., Yu, Y., Chen, H., DiSalvo, F. J. & Abruña, H. D. Yolk–shell structure of polyaniline-coated sulfur for lithium–sulfur batteries. *J. Am. Chem. Soc.* **135**, 16736–16743 (2013).

118. Li, W. *et al.* Understanding the role of different conductive polymers in improving the nanostructured sulfur cathode performance. *Nano Lett.* **13**, 5534–5540 (2013).

119. Manthiram, A., Fu, Y., Chung, S.-H., Zu, C. & Su, Y.-S. Rechargeable lithium–sulfur batteries. *Chem. Rev.* **114**, 11751–11787 (2014).

120. Peng, H.-J., Huang, J.-Q., Cheng, X.-B. & Zhang, Q. Review on high-Loading and high-energy lithium–sulfur batteries. *Adv. Energy Mater.* 260–313 (2017).

121. Su, Y.-S. & Manthiram, A. A new approach to improve cycle performance of rechargeable lithium-sulfur batteries by inserting a free-standing MWCNT interlayer. *Chem. Commun.* **48**, 8817–8819 (2012).

122. Zu, C., Su, Y.-S., Fu, Y. & Manthiram, A. Improved lithium-sulfur cells with a treated carbon paper interlayer. *Phys. Chem. Chem. Phys.* **15**, 2291–2297 (2013).

123. Chung, S.-H. & Manthiram, A. A natural carbonized leaf as polysulfide diffusion inhibitor for high-performance lithium–sulfur battery cells. *ChemSusChem* **7**, 1655–1661 (2014).

124. Chung, S.-H. & Manthiram, A. A hierarchical carbonized paper with controllable thickness as a modulable interlayer system for high performance Li-S batteries. *Chem. Commun.* **50**, 4184–4187 (2014).

125. Yao, H. *et al.* Improved lithium-sulfur batteries with a conductive coating on the separator to prevent the accumulation of inactive S-related species at the cathode-separator interface. *Energy Environ. Sci.* **7**, 3381–3390 (2014).

126. Chang, C.-H., Chung, S.-H. & Manthiram, A. Effective stabilization of a high-loading sulfur cathode and a lithium-metal anode in Li-S batteries

utilizing SWCNT-modulated separators. *Small* **12**, 174–179 (2016).

127. Su, Y.-S. & Manthiram, A. Lithium–sulphur batteries with a microporous carbon paper as a bifunctional interlayer. *Nat Commun* **3**, 1166 (2012).

128. Su, Y.-S., Fu, Y., Guo, B., Dai, S. & Manthiram, A. Fast, reversible lithium storage with a sulfur/long-chain-polysulfide redox couple. *Chem. – A Eur. J.* **19**, 8621–8626 (2013).

129. Ma, G. *et al.* Enhanced cycle performance of Li–S battery with a polypyrrole functional interlayer. *J. Power Sources* **267**, 542–546 (2014).

130. Ma, G. *et al.* Enhanced performance of lithium sulfur battery with self-assembly polypyrrole nanotube film as the functional interlayer. *J. Power Sources* **273**, 511–516 (2015).

131. Zhao, T. *et al.* Advanced lithium–sulfur batteries enabled by a bio-inspired polysulfide adsorptive brush. *Adv. Funct. Mater.* **26**, 8418–8426 (2016).

132. Zhang, K. *et al.* Nickel foam as interlayer to improve the performance of lithium–sulfur battery. *J. Solid State Electrochem.* **18**, 1025–1029 (2014).

133. Mikhaylik, Y. V & Akridge, J. R. Polysulfide shuttle study in the Li/S battery system. *J. Electrochem. Soc.* **151**, A1969–A1976 (2004).

134. Aurbach, D. *et al.* On the surface chemical aspects of very high energy density, rechargeable Li–sulfur batteries. *J. Electrochem. Soc.* **156**, A694–A702 (2009).

135. Zhang, S. S. Liquid electrolyte lithium/sulfur battery: Fundamental chemistry, problems, and solutions. *J. Power Sources* **231**, 153–162 (2013).

136. Lin, Z., Liu, Z., Fu, W., Dudney, N. J. & Liang, C. Phosphorous pentasulfide as a novel additive for high-performance lithium-sulfur batteries. *Adv. Funct. Mater.* **23**, 1064–1069 (2013).

137. Huang, C. *et al.* Manipulating surface reactions in lithium–sulphur batteries using hybrid anode structures. *Nat Commun* **5**, (2014).

138. Jing, H.-K., Kong, L.-L., Liu, S., Li, G.-R. & Gao, X.-P. Protected lithium anode with porous Al_2O_3 layer for lithium-sulfur battery. *J. Mater. Chem. A* **3**, 12213–12219 (2015).

139. Ma, G. *et al.* A lithium anode protection guided highly-stable lithium-sulfur battery. *Chem. Commun.* **50**, 14209–14212 (2014).

140. Zhang, W., Liu, Y. & Guo, Z. Approaching high-performance potassium-ion batteries via advanced design strategies and engineering. *Sci. Adv.* **5**, eaav7412 (2019).

141. Larcher, D. & Tarascon, J.-M. Towards greener and more sustainable batteries for electrical energy storage. *Nat. Chem.* **7**, 19 (2014).

142. Vaalma, C., Buchholz, D., Weil, M. & Passerini, S. A cost and resource analysis of sodium-ion batteries. *Nat. Rev. Mater.* **3**, 18013 (2018).

143. Komaba, S., Hasegawa, T., Dahbi, M. & Kubota, K. Potassium intercalation into graphite to realize high-voltage/high-power potassium-ion batteries and potassium-ion capacitors. *Electrochem. commun.* **60**, 172–175 (2015).

144. Du, G. *et al.* Superior stability and high capacity of restacked molybdenum disulfide as anode material for lithium ion batteries. *Chem. Commun.* **46**, 1106–1108 (2010).

145. Zhu, C., Mu, X., van Aken, P. A., Yu, Y. & Maier, J. Single-layered ultrasmall nanoplates of MoS_2 embedded in carbon nanofibers with excellent electrochemical performance for lithium and sodium storage. *Angew. Chemie* **126**, 2184–2188 (2014).

146. Xie, K. *et al.* Superior potassium ion storage via vertical MoS_2 "Nano-Rose" with expanded interlayers on graphene. *Small* **13** 1701471-1701478 (2017).

147. Liu, J., Xia, H., Xue, D. & Lu, L. Double-shelled nanocapsules of V_2O_5-based composites as high-performance anode and cathode materials for Li ion batteries. *J. Am. Chem. Soc.* **131**, 12086–12087 (2009).

148. Liu, J., Chen, J. S., Wei, X., Lou, X. W. & Liu, X.-W. Sandwich-like, stacked

ultrathin titanate nanosheets for ultrafast lithium storage. *Adv. Mater.* **23**, 998–1002 (2010).

149. Ma, J. *et al.* Layered lepidocrocite type structure isolated by revisiting the sol–gel chemistry of anatase TiO_2: A new anode material for batteries. *Chem. Mater.* **29**, 8313–8324 (2017).

150. Reeves, K. G. *et al.* Insights into Li^+, Na^+, and K^+ intercalation in lepidocrocite-type layered TiO_2 structures. *ACS Appl. Energy Mater.* **1**, 2078–2086 (2018).

151. Dong, Y. *et al.* Ti_3C_2 MXene-derived sodium/potassium titanate nanoribbons for high-performance sodium/potassium ion batteries with enhanced capacities. *ACS Nano* **11**, 4792–4800 (2017).

152. Zeng, C. *et al.* Ultrathin titanate nanosheets/graphene films derived from confined transformation for excellent Na/K ion storage. *Angew. Chemie Int. Ed.* **57**, 8540–8544 (2018).

153. Kishore, B., G, V. & Munichandraiah, N. $K_2Ti_4O_9$: A promising anode material for potassium ion batteries. *J. Electrochem. Soc.* **163**, A2551–A2554 (2016).

154. Han, J. *et al.* Exploration of $K_2Ti_8O_{17}$ as an anode material for potassium-ion batteries. *Chem. Commun.* **52**, 11274–11276 (2016).

155. Prakash, A. S. *et al.* Solution-combustion synthesized nanocrystalline $Li_4Ti_5O_{12}$ as high-rate performance Li-ion battery anode. *Chem. Mater.* **22**, 2857–2863 (2010).

156. Huang, J. P. *et al.* Electrochemical sodium storage of TiO_2(B) nanotubes for sodium ion batteries. *RSC Adv.* **3**, 12593–12597 (2013).

157. Yang, X. *et al.* Anatase TiO_2 nanocubes for fast and durable sodium ion battery anodes. *J. Mater. Chem. A* **3**, 8800–8807 (2015).

158. Cao, K. *et al.* $Na_2Ti_6O_{13}$ Nanorods with dominant large interlayer spacing exposed facet for hgh-performance Na-ion batteries. *Small* **12**, 2991–2997

(2016).

159. Wang, W. *et al.* Microspheric $Na_2Ti_3O_7$ consisting of tiny nanotubes: an anode material for sodium-ion batteries with ultrafast charge–discharge rates. *Nanoscale* **5**, 594–599 (2013).

160. Pan, H. *et al.* Sodium storage and transport properties in layered $Na_2Ti_3O_7$ for room-temperature sodium-ion batteries. *Adv. Energy Mater.* **3**, 1186–1194 (2013).

161. Chen, J. S. *et al.* Constructing hierarchical spheres from large ultrathin anatase TiO_2 nanosheets with nearly 100% exposed (001) facets for fast reversible lithium storage. *J. Am. Chem. Soc.* **132**, 6124–6130 (2010).

162. Armstrong, A. R., Armstrong, G., Canales, J., García, R. & Bruce, P. G. Lithium-ion intercalation into TiO_2-B nanowires. *Adv. Mater.* **17**, 862–865 (2005).

163. Zhang, J. *et al.* Development status and future prospect of non-aqueous potassium ion batteries for large scale energy storage. *Nano Energy* **60**, 340–361 (2019).

164. Xu, Y.-S. *et al.* Recent developments in electrode materials for potassium-ion batteries. *J. Mater. Chem. A* **7**, 4334–4352 (2019).

165. Eftekhari, A. Potassium secondary cell based on Prussian blue cathode. *J. Power Sources* **126**, 221–228 (2004).

166. Wessells, C. D., Peddada, S. V, Huggins, R. A. & Cui, Y. Nickel hexacyanoferrate nanoparticle electrodes for aqueous sodium and potassium ion batteries. *Nano Lett.* **11**, 5421–5425 (2011).

167. Padigi, P. *et al.* Prussian green: A high rate capacity cathode for potassium ion batteries. *Electrochim. Acta* **166**, 32–39 (2015).

168. He, G. & Nazar, L. F. Crystallite size control of prussian white analogues for nonaqueous potassium-ion batteries. *ACS Energy Lett.* **2**, 1122–1127 (2017).

169. Wessells, C. D., Huggins, R. A. & Cui, Y. Copper hexacyanoferrate battery electrodes with long cycle life and high power. *Nat. Commun.* **2**, 550 (2011).

170. Li, W., Dahn, J. R. & Wainwright, D. S. Rechargeable lithium batteries with aqueous electrolytes. *Science (80-.).* **264**, 1115 LP – 1118 (1994).

171. Xue, L. *et al.* Low-cost high-energy potassium cathode. *J. Am. Chem. Soc.* **139**, 2164–2167 (2017).

172. Shadike, Z. *et al.* Long life and high-rate Berlin green $FeFe(CN)_6$ cathode material for a non-aqueous potassium-ion battery. *J. Mater. Chem. A* **5**, 6393–6398 (2017).

173. Ling, C., Chen, J. & Mizuno, F. First-principles study of alkali and alkaline earth ion intercalation in iron hexacyanoferrate: The important role of ionic radius. *J. Phys. Chem. C* **117**, 21158–21165 (2013).

174. Piernas-Muñoz, M. J., Castillo-Martínez, E., Bondarchuk, O., Armand, M. & Rojo, T. Higher voltage plateau cubic Prussian White for Na-ion batteries. *J. Power Sources* **324**, 766–773 (2016).

175. Hironaka, Y., Kubota, K. & Komaba, S. P2- and P3-K_xCoO_2 as an electrochemical potassium intercalation host. *Chem. Commun.* **53**, 3693–3696 (2017).

176. Delmas, C., Fouassier, C. & Hagenmuller, P. Les bronzes de cobalt K_xCoO_2 ($x < 1$). L'oxyde $KCoO_2$. *J. Solid State Chem.* **13**, 165–171 (1975).

177. Taniguchi, H., Ebina, Y., Takada, K. & Sasaki, T. Synthesis and soft-chemical reactivity of layered potassium cobalt oxide. *Solid State Ionics* **176**, 2367–2370 (2005).

178. Kim, H. *et al.* K-ion batteries based on a P2-type $K_{0.6}CoO_2$ cathode. *Adv. Energy Mater.* **7**, 1700098 (2017).

179. Deng, T. *et al.* Self-templated formation of P2-type $K_{0.6}CoO_2$ microspheres for high reversible potassium-ion batteries. *Nano Lett.* **18**, 1522–1529 (2018).

180. Vaalma, C., Giffin, G. A., Buchholz, D. & Passerini, S. Non-aqueous k-ion battery based on layered $K_{0.3}MnO_2$ and hard carbon/carbon black. *J. Electrochem. Soc.* **163**, A1295–A1299 (2016).

181. Kim, H. *et al.* Investigation of potassium storage in layered P3-type $K_{0.5}MnO_2$ cathode. *Adv. Mater.* **29** (2017).

182. Wang, X. *et al.* Earth abundant Fe/Mn-based layered oxide interconnected nanowires for advanced K-ion full batteries. *Nano Lett.* **17**, 544–550 (2017).

183. Kim, H. *et al.* Stoichiometric layered potassium transition metal oxide for rechargeable potassium batteries. *Chem. Mater.* **30**, 6532–6539 (2018).

184. Deng, L. *et al.* Layered potassium vanadate $K_{0.5}V_2O_5$ as a cathode material for nonaqueous potassium ion batteries. *Adv. Funct. Mater.* **28**, 1800670 (2018).

185. Yakubovich, O. V, Massa, W. & Dimitrova, O. V. A new type of anionic framework in microporous potassium iron(ii) phosphate $K[Fe(PO_4)]$. *Zeitschrift für Anorg. und Allg. Chemie* **631**, 2445–2449 (2005).

186. Liu, Y. *et al.* Porous amorphous $FePO_4$ nanoparticles connected by single-wall carbon nanotubes for sodium ion battery cathodes. *Nano Lett.* **12**, 5664–5668 (2012).

187. Mathew, V. *et al.* Amorphous iron phosphate: potential host for various charge carrier ions. *Npg Asia Mater.* **6**, e138 (2014).

188. Han, J. *et al.* Investigation of $K_3V_2(PO_4)_3$/C nanocomposites as high-potential cathode materials for potassium-ion batteries. *Chem. Commun.* **53**, 1805–1808 (2017).

189. Lin, X., Huang, J., Tan, H., Huang, J. & Zhang, B. $K_3V_2(PO_4)_2F_3$ as a robust cathode for potassium-ion batteries. *Energy Storage Mater.* **16**, 97–101 (2019).

190. Recham, N. *et al.* Preparation and characterization of a stable $FeSO_4F$-based framework for alkali ion insertion electrodes. *Chem. Mater.* **24**,

4363–4370 (2012).

191. Jian, Z., Luo, W. & Ji, X. Carbon electrodes for K-ion batteries. *J. Am. Chem. Soc.* **137**, 11566–11569 (2015).

192. Schleede, V. A. & Wellmann, M. Notiz über die herstellung eines lindemannglases für kapillaren zwecks aufnahme von luftempfindlichen substanzen mit langwelliger röntgenstrahlung. *Z. Krist. Cryst. Mater.* **83**, 148–149 (1932).

193. Rüdorff, W. & Schulze, E. Über Alkaligraphitverbindungen. *Zeitschrift für Anorg. und Allg. Chemie* **277**, 156–171 (1954).

194. Matuyama, E. Successive stages of a graphite–potassium compound and its thermal expansion. *Nature* **193**, 61 (1962).

195. Parry, G. S. & Nixon, D. E. Order–disorder transformation in potassium graphite. *Nature* **216**, 909–910 (1967).

196. Nixon, D. E. & Parry, G. S. Formation and structure of the potassium graphites. *J. Phys. D. Appl. Phys.* **1**, 291–298 (1968).

197. Nixon, D. E. & Parry, G. S. The expansion of the carbon-carbon bond length in potassium graphites. *J. Phys. C Solid State Phys.* **2**, 1732–1741 (1969).

198. Wang, Z., Selbach, S. M. & Grande, T. Van der Waals density functional study of the energetics of alkali metal intercalation in graphite. *RSC Adv.* **4**, 4069–4079 (2014).

199. Ge, P. & Fouletier, M. Electrochemical intercalation of sodium in graphite. *Solid State Ionics* **28–30**, 1172–1175 (1988).

200. Asher, R. C. & Wilson, S. A. Lamellar compound of sodium with graphite. *Nature* **181**, 409–410 (1958).

201. Luo, W. *et al.* Potassium ion batteries with graphitic materials. *Nano Lett.* **15**, 7671–7677 (2015).

202. Jian, Z., Xing, Z., Bommier, C., Li, Z. & Ji, X. Hard carbon microspheres:

Potassium-ion anode versus sodium-ion anode. *Adv. Energy Mater.* **6** (2016).

203. Jian, Z. *et al.* Hard–soft composite carbon as a long-cycling and high-rate anode for potassium-ion batteries. *Adv. Funct. Mater.* **27**, 1700324 (2017).

204. Wei, W. *et al.* Short-range order in mesoporous carbon boosts potassium-ion battery performance. *Adv. Energy Mater.* **8**, 1701648 (2017).

205. Share, K., Cohn, A. P., Carter, R., Rogers, B. & Pint, C. L. Role of nitrogen-doped graphene for improved high-capacity potassium ion battery anodes. *ACS Nano* **10**, 9738–9744 (2016).

206. Xie, Y. *et al.* Ultra-high pyridinic N-doped porous carbon monolith enabling high-capacity K-ion battery anodes for both half-cell and full-cell applications. *Adv. Mater.* (2017).

207. Yang, J. *et al.* Enhanced capacity and rate capability of nitrogen/oxygen dual-doped hard carbon in capacitive potassium-ion storage. *Adv. Mater.* **30** (2018).

208. Ju, Z. *et al.* Direct synthesis of few-layer F-doped graphene foam and its lithium/potassium storage properties. *ACS Appl. Mater. Interfaces* **8**, 20682–20690 (2016).

209. Xu, Y. *et al.* Highly nitrogen doped carbon nanofibers with superior rate capability and cyclability for potassium ion batteries. *Nat. Commun.* **9**, 1720 (2018).

210. Han, K. *et al.* High-throughput fabrication of 3D N-doped graphenic framework coupled with Fe_3C@porous graphite carbon for ultrastable potassium ion storage. *Energy Storage Mater.* (2019).

211. Wang, H., Maiyalagan, T. & Wang, X. Review on recent progress in nitrogen-doped graphene: Synthesis, characterization, and its potential applications. *ACS Catal.* **2**, 781–794 (2012).

212. Wang, N. *et al.* Comprehensive new insights and perspectives into Ti-

based anodes for next-generation alkaline metal (Na^+, K^+) ion batteries. *Adv. Energy Mater.* **8**, 1801888 (2018).

213. Pham, T. A., Kweon, K. E., Samanta, A., Lordi, V. & Pask, J. E. Solvation and dynamics of sodium and potassium in ethylene carbonate from *ab Initio* molecular dynamics simulations. *J. Phys. Chem. C* **121**, 21913–21920 (2017).

214. Liu, Z. *et al.* Zero-strain $K_{0.6}Mn_1F_{2.7}$ hollow nanocubes for ultrastable potassium ion storage. *Energy Environ. Sci.* **11**, 3033–3042 (2018).

215. Sultana, I., Rahman, M. M., Chen, Y. & Glushenkov, A. M. Potassium-ion battery anode materials operating through the alloying–dealloying reaction mechanism. *Adv. Funct. Mater.* **28**, 1703857 (2018).

216. Sultana, I., Rahman, M. M., Chen, Y. & Glushenkov, A. M. Potassium-ion battery anode materials operating through the alloying–dealloying reaction mechanism. *Adv. Funct. Mater.* **28**, 1703857 (2018).

217. Sultana, I., Ramireddy, T., Rahman, M. M., Chen, Y. & Glushenkov, A. M. Tin-based composite anodes for potassium-ion batteries. *Chem. Commun.* **52**, 9279–9282 (2016).

218. Huang, K. *et al.* Direct synthesis of 3D hierarchically porous carbon/Sn composites via in situ generated NaCl crystals as templates for potassium-ion batteries anode. *J. Mater. Chem. A* **6**, 434–442 (2018).

219. Zheng, J. *et al.* Extremely stable antimony–carbon composite anodes for potassium-ion batteries. *Energy Environ. Sci.* **12**, 615–623 (2019).

220. Liu, Q. *et al.* Super long-life potassium-ion batteries based on an antimony@carbon composite anode. *Chem. Commun.* **54**, 11773–11776 (2018).

221. Lei, K. *et al.* A porous network of bismuth used as the anode material for high-energy-density potassium-ion batteries. *Angew. Chemie Int. Ed.* **57**, 4687–4691 (2018).

222. Zheng, J. *et al.* Extremely stable antimony–carbon composite anodes for potassium-ion batteries. *Energy Environ. Sci.* **12**, 615–623 (2019).

223. Liu, Q. *et al.* Super long-life potassium-ion batteries based on an antimony@carbon composite anode. *Chem. Commun.* **54**, 11773–11776 (2018).

224. Sultana, I. *et al.* K-ion and Na-ion storage performances of Co_3O_4–Fe_2O_3 nanoparticle-decorated super P carbon black prepared by a ball milling process. *Nanoscale* **9**, 3646–3654 (2017).

225. Yu, Q. *et al.* Metallic octahedral $CoSe_2$ threaded by N-doped carbon nanotubes: A flexible framework for high-performance potassium-ion batteries. *Adv. Sci.* **5**, 1800782 (2018).

226. Wang, W. *et al.* Pistachio-shuck-like $MoSe_2$/C core/shell nanostructures for high-performance potassium-ion storage. *Adv. Mater.* **30**, 1801812 (2018).

227. Liu, Y. *et al.* Boosting potassium-ion batteries by few-layered composite anodes prepared via solution-triggered one-step shear exfoliation. *Nat. Commun.* **9**, 3645 (2018).

228. Ge, J. *et al.* $MoSe_2$/N-doped carbon as anodes for potassium-ion batteries. *Adv. Energy Mater.* **8**, 1801477 (2018).

229. Jia, B. *et al.* Bamboo-like hollow tubes with MoS_2/N-doped-C interfaces boost potassium-ion storage. *Adv. Funct. Mater.* **28**, 1803409 (2018).

230. Bai, J. *et al.* One-step construction of N,P-codoped porous carbon sheets/CoP hybrids with enhanced lithium and potassium storage. *Adv. Mater.* **30**, 1802310 (2018).

231. Yang, C. *et al.* Metallic graphene like VSe_2 ultrathin nanosheets: Superior potassium-ion storage and their working mechanism. *Adv. Mater.* **30**, 1800036 (2018).

232. Chu, J. *et al.* Deeply nesting zinc sulfide dendrites in tertiary hierarchical

structure for potassium ion batteries: enhanced conductivity from interior to exterior. *ACS Nano* (2019).

233. Fang, L. *et al.* Few-layered tin sulfide nanosheets supported on reduced graphene oxide as a high-performance anode for potassium-ion batteries. *Small* **15**, 1804806 (2019).

234. Greiner, A. & Wendorff, J. H. Electrospinning: A fascinating method for the preparation of ultrathin fibers. *Angew. Chemie Int. Ed.* **46**, 5670–5703 (2007).

235. Ramakrishna, W. E. T. and S. A review on electrospinning design and nanofibre assemblies. *Nanotechnology* **17**, R89 (2006).

236. Li, D. & Xia, Y. Electrospinning of nanofibers: Reinventing the wheel? *Adv. Mater.* **16**, 1151–1170 (2004).

237. Doshi, J. & Reneker, D. H. Electrospinning process and applications of electrospun fibers. *J. Electrostat.* **35**, 151–160 (1995).

238. Matthews, J. A., Wnek, G. E., Simpson, D. G. & Bowlin, G. L. Electrospinning of collagen nanofibers. *Biomacromolecules* **3**, 232–238 (2002).

239. Ramakrishna, W. E. T. and M. K. and X. M. M. and S. Porous tubular structures with controlled fibre orientation using a modified electrospinning method. *Nanotechnology* **16**, 918 (2005).

240. Sundaray, B. *et al.* Electrospinning of continuous aligned polymer fibers. *Appl. Phys. Lett.* **84**, 1222–1224 (2004).

241. Li, D., Wang, Y. & Xia, Y. Electrospinning of polymeric and ceramic nanofibers as uniaxially aligned arrays. *Nano Lett.* **3**, 1167–1171 (2003).

242. Li, D., Wang, Y. & Xia, Y. Electrospinning nanofibers as uniaxially aligned arrays and layer-by-layer stacked films. *Adv. Mater.* **16**, 361–366 (2004).

243. Yang, D., Lu, B., Zhao, Y. & Jiang, X. Fabrication of aligned fibrous arrays by magnetic electrospinning. *Adv. Mater.* **19**, 3702–3706 (2007).

244. Li, D. & Xia, Y. Fabrication of titania nanofibers by electrospinning. *Nano Lett.* **3**, 555–560 (2003).

245. Sill, T. J. & von Recum, H. A. Electrospinning: Applications in drug delivery and tissue engineering. *Biomaterials* **29**, 1989–2006 (2008).

246. Baumgarten, P. K. Electrostatic spinning of acrylic microfibers. *J. Colloid Interface Sci.* **36**, 71–79 (1971).

247. Hayati, I., Bailey, A. I. & Tadros, T. . Investigations into the mechanisms of electrohydrodynamic spraying of liquids. *J. Colloid Interface Sci.* **117**, 205–221 (1987).

248. Li, D., McCann, J. T., Xia, Y. & Marquez, M. Electrospinning: A simple and versatile technique for producing ceramic nanofibers and nanotubes. *J. Am. Ceram. Soc.* **89**, 1861–1869 (2006).

249. Megelski, S., Stephens, J. S., Chase, D. B. & Rabolt, J. F. Micro- and nanostructured surface morphology on electrospun polymer fibers. *Macromolecules* **35**, 8456–8466 (2002).

250. Sun, Z., Zussman, E., Yarin, A. L., Wendorff, J. H. & Greiner, A. Compound core–shell polymer nanofibers by co-electrospinning. *Adv. Mater.* **15**, 1929–1932 (2003).

251. Zhang, Y., Huang, Z.-M., Xu, X., Lim, C. T. & Ramakrishna, S. Preparation of core–shell structured PCL-r-Gelatin bi-component nanofibers by coaxial electrospinning. *Chem. Mater.* **16**, 3406–3409 (2004).

252. Li, D. & Xia, Y. Direct fabrication of composite and ceramic hollow nanofibers by electrospinning. *Nano Lett.* **4**, 933–938 (2004).

253. Kumar, A., Jose, R., Fujihara, K., Wang, J. & Ramakrishna, S. Structural and optical properties of electrospun TiO2 nanofibers. *Chem. Mater.* **19**, 6536–6542 (2007).

254. Lee, J. *et al.* Direct access to thermally stable and highly crystalline mesoporous transition-metal oxides with uniform pores. *Nat Mater* **7**,

222–228 (2008).

255. Nuansing, W., Ninmuang, S., Jarernboon, W., Maensiri, S. & Seraphin, S. Structural characterization and morphology of electrospun TiO_2 nanofibers. *Mater. Sci. Eng. B* **131**, 147–155 (2006).

256. Cheng, D. *et al.* Regulating micro-structure and biomineralization of electrospun PVP-based hybridized carbon nanofibers containing bioglass nanoparticles via aging time. *RSC Adv.* **6**, 3870–3881 (2016).

257. Ritala, M., Leskela, M., Niinisto, L. & Haussalo, P. Titanium isopropoxide as a precursor in atomic layer epitaxy of titanium dioxide thin films. *Chem. Mater.* **5**, 1174–1181 (1993).

258. Fictorie, C. P., Evans, J. F. & Gladfelter, W. L. Kinetic and mechanistic study of the chemical vapor deposition of titanium dioxide thin films using tetrakis-(isopropoxo)-titanium(IV). *J. Vac. Sci. Technol. A Vacuum, Surfaces, Film.* **12**, 1108–1113 (1994).

259. Kruk, M. & Jaroniec, M. Gas adsorption characterization of ordered organic–inorganic nanocomposite materials. *Chem. Mater.* **13**, 3169–3183 (2001).

260. Sattler, K. D. *Carbon Nanomaterials Source Book: Nanoparticles, Nanocapsules, Nanofibers, Nanoporous Structures, and Nanocomposites, Volume II*. (CRC Press, 2016).

261. Kim, S. *et al.* Preparation of flexible zinc oxide/carbon nanofiber webs for mid-temperature desulfurization. *Appl. Surf. Sci.* **320**, 218–224 (2014).

262. Lee, J. *et al.* Simple fabrication of flexible electrodes with high metal-oxide content: Electrospun reduced tungsten oxide/carbon nanofibers for lithium ion battery applications. *Nanoscale* **6**, 10147–10155 (2014).

263. Subrahmanyam, K. S., Vivekchand, S. R. C., Govindaraj, A. & Rao, C. N. R. A study of graphenes prepared by different methods: Characterization, properties and solubilization. *J. Mater. Chem.* **18**, 1517–1523 (2008).

264. Bisquert, J. & Compte, A. Theory of the electrochemical impedance of anomalous diffusion. *J. Electroanal. Chem.* **499**, 112–120 (2001).

265. Liang, G. *et al.* Ultrafine TiO_2 decorated carbon nanofibers as multifunctional interlayer for high-performance lithium–sulfur battery. *ACS Appl. Mater. Interfaces* **8**, 23105–23113 (2016).

266. Xiao, Z. *et al.* A lightweight TiO_2/graphene interlayer, applied as a highly effective polysulfide absorbent for fast, long-life lithium–sulfur batteries. *Adv. Mater.* **27**, 2891–2898 (2015).

267. Hong, S. Y. *et al.* Charge carriers in rechargeable batteries: Na ions vs. Li ions. *Energy Environ. Sci.* **6**, 2067–2081 (2013).

268. Fruchter, L., Crepy, G. & Le Mehaute, A. Batteries, identified fractal objects. *J. Power Sources* **18**, 51–62 (1986).

269. Wu, X. *et al.* Diffusion-free Grotthuss topochemistry for high-rate and long-life proton batteries. *Nat. Energy* **4**, 123–130 (2019).

270. Wang, P.-F. *et al.* Na^+ vacancy disordering promises high-rate Na-ion batteries. *Sci. Adv.* **4**, eaar6018 (2018).

271. Lee, M. *et al.* High-performance sodium–organic battery by realizing four-sodium storage in disodium rhodizonate. *Nat. Energy* **2**, 861–868 (2017).

272. Okoshi, M., Yamada, Y., Yamada, A. & Nakai, H. Theoretical analysis on de-solvation of lithium, sodium, and magnesium cations to organic electrolyte ssolvents. *J. Electrochem. Soc.* **160**, A2160–A2165 (2013).

273. Simon, P. & Gogotsi, Y. Materials for electrochemical capacitors. *Nat. Mater.* **7**, 845 (2008).

274. Wang, Q., Gao, Q. & Shi, J. Reversible intercalation of large-capacity hemoglobin into in Situ prepared titanate interlayers with enhanced thermal and organic medium stabilities. *Langmuir* **20**, 10231–10237 (2004).

275. Besselink, R., Stawski, T. M., Castricum, H. L., Blank, D. H. A. & ten Elshof,

J. E. Exfoliation and restacking of lepidocrocite-type layered titanates studied by small-angle x-ray scattering. *J. Phys. Chem. C* **114**, 21281–21286 (2010).

276. Kamada, K. & Soh, N. Temperature-controlled reversible exfoliation-stacking of titanate nanosheets in an aqueous solution containing tetraalkylammonium ions. *RSC Adv.* **4**, 8682–8685 (2014).

277. Divigalpitiya, W. M. R., Frindt, R. F. & Morrison, S. R. Inclusion systems of organic molecules in restacked single-layer molybdenum disulfide. *Science (80-.).* **246**, 369 LP – 371 (1989).

278. Heising, J. & Kanatzidis, M. G. Exfoliated and restacked MoS_2 and WS_2: Ionic or neutral species? Encapsulation and ordering of hard electropositive cations. *J. Am. Chem. Soc.* **121**, 11720–11732 (1999).

279. Nicolosi, V., Chhowalla, M., Kanatzidis, M. G., Strano, M. S. & Coleman, J. N. Liquid Exfoliation of Layered Materials. *Science (80-.).* **340**, (2013).

280. Geim, A. K. & Grigorieva, I. V. Van der Waals heterostructures. *Nature* **499**, 419 (2013).

281. Pomerantseva, E. & Gogotsi, Y. Two-dimensional heterostructures for energy storage. *Nat. Energy* **2**, 17089 (2017).

282. Lim, J., Jin, X., Jo, Y. K., Lee, S. & Hwang, S. Kinetically controlled layer-by-layer stacking of metal oxide 2D nanosheets. *Angew. Chemie Int. Ed.* **56**, 7093–7096 (2017).

283. Bediako, D. K. *et al.* Heterointerface effects in the electrointercalation of van der Waals heterostructures. *Nature* **558**, 425–429 (2018).

284. Wang, S. L. *et al.* Fabrication and properties of a free-standing two-dimensional titania. *J. Am. Chem. Soc.* **139**, 15414–15419 (2017).

285. Tsai, C.-C. & Teng, H. Structural features of nanotubes synthesized from NaOH treatment on TiO_2 with different post-treatments. *Chem. Mater.* **18**, 367–373 (2006).

286. Howe, R. F. & Gratzel, M. EPR study of hydrated anatase under UV irradiation. *J. Phys. Chem.* **91**, 3906–3909 (1987).

287. Yang, J. *et al.* Study on composition, structure and formation process of nanotube $Na_2Ti_2O_4(OH)_2$. *Dalt. Trans.* 3898–3901 (2003).

288. Peng, C.-W. *et al.* Chimie douce route to sodium hydroxo titanate nanowires with modulated sructure and conversion to highly photoactive titanium dioxides. *Chem. Mater.* **20**, 7228–7236 (2008).

289. Xie, J., Yang, P. & He, H. Layered $Na_2Ti_2O_4(OH)_2$ and $K_2Ti_2O_4(OH)_2$ nanoarrays for Na/Li-ion intercalation systems: Effect of ion size. *J. Electrochem. Soc.* **163**, A2203–A2210 (2016).

290. Kresse, G. & Furthmüller, J. Efficient iterative schemes for ab initio total-energy calculations using a plane-wave basis set. *Phys. Rev. B* **54**, 11169–11186 (1996).

291. Kresse, G. & Furthmüller, J. Efficiency of *ab initio* total energy calculations for metals and semiconductors using a plane-wave basis set. *Comput. Mater. Sci.* **6**, 15–50 (1996).

292. Kresse, G. & Joubert, D. From ultrasoft pseudopotentials to the projector augmented-wave method. *Phys. Rev. B* **59**, 1758–1775 (1999).

293. Perdew, J. P. *et al.* Atoms, molecules, solids, and surfaces: Applications of the generalized gradient approximation for exchange and correlation. *Phys. Rev. B* **46**, 6671–6687 (1992).

294. Grimme, S., Antony, J., Ehrlich, S. & Krieg, H. A consistent and accurate ab initio parametrization of density functional dispersion correction (DFT-D) for the 94 elements H-Pu. *J. Chem. Phys.* **132**, 154104 (2010).

295. Zhang, S. *et al.* Formation mechanism of $H_2Ti_3O_7$ nanotubes. *Phys. Rev. Lett.* **91**, 256103 (2003).

296. Ma, R., Bando, Y. & Sasaki, T. Nanotubes of lepidocrocite titanates. *Chem. Phys. Lett.* **380**, 577–582 (2003).

297. Zhang, M. *et al.* Effect of annealing temperature on morphology, structure and photocatalytic behavior of nanotubed $H_2Ti_2O_4(OH)_2$. *J. Mol. Catal. A Chem.* **217**, 203–210 (2004).

298. Britvin, S. N., Lotnyk, A., Kienle, L., Krivovichev, S. V & Depmeier, W. Layered hydrazinium titanate: Advanced reductive adsorbent and chemical toolkit for design of titanium dioxide nanomaterials. *J. Am. Chem. Soc.* **133**, 9516–9525 (2011).

299. Shirpour, M., Cabana, J. & Doeff, M. New materials based on a layered sodium titanate for dual electrochemical Na and Li intercalation systems. *Energy Environ. Sci.* **6**, 2538–2547 (2013).

300. Wang, S. *et al.* Lithium titanate hydrates with superfast and stable cycling in lithium ion batteries. *Nat. Commun.* **8**, 627 (2017).

301. Adersoson, S. & Wadsley, A. D. Five co-ordinated titanium in $K_2Ti_2O_5$. *Nature* **187**, 499–500 (1960).

302. Sasaki, T., Watanabe, M., Komatsu, Y. & Fujiki, Y. Layered hydrous titanium dioxide: potassium ion exchange and structural characterization. *Inorg. Chem.* **24**, 2265–2271 (1985).

303. Masaki, N., Uchida, S., Yamane, H. & Sato, T. Hydrothermal synthesis of potassium titanates in Ti-KOH-H2O system. *J. Mater. Sci.* **35**, 3307–3311 (2000).

304. Cullity, B. D. & Stock, S. R. *Elements of x-ray diffraction*. (Prentice Hall, 2001).

305. Kim, C. *et al.* Comparison of titanium soaked in 5M NaOH or 5M KOH solutions. *Mater. Sci. Eng. C* **33**, 327–339 (2013).

306. Zhang, H. & Banfield, J. F. Structural characteristics and mechanical and thermodynamic properties of nanocrystalline TiO_2. *Chem. Rev.* **114**, 9613–9644 (2014).

307. Ferrari, A. C. & Robertson, J. Raman spectroscopy of amorphous,

nanostructured, diamond–like carbon, and nanodiamond. *Philos. Trans. R. Soc. London A Math. Phys. Eng. Sci.* **362**, 2477–2512 (2004).

308. Cuesta, A., Dhamelincourt, P., Laureyns, J., Martínez-Alonso, A. & Tascón, J. M. D. Raman microprobe studies on carbon materials. *Carbon N. Y.* **32**, 1523–1532 (1994).

309. Bogdanov, K. *et al.* Annealing-induced structural changes of carbon onions: High-resolution transmission electron microscopy and Raman studies. *Carbon N. Y.* **73**, 78–86 (2014).

310. Hu, C. *et al.* Raman spectroscopy study of the transformation of the carbonaceous skeleton of a polymer-based nanoporous carbon along the thermal annealing pathway. *Carbon N. Y.* **85**, 147–158 (2015).

311. Raccichini, R., Varzi, A., Passerini, S. & Scrosati, B. The role of graphene for electrochemical energy storage. *Nat. Mater.* **14**, 271 (2014).

312. Endo, M., Kim, C., Nishimura, K., Fujino, T. & Miyashita, K. Recent development of carbon materials for Li ion batteries. *Carbon N. Y.* **38**, 183–197 (2000).

313. Cullen, P. L. *et al.* Ionic solutions of two-dimensional materials. *Nat. Chem.* **9**, 244 (2016).

314. Hwang, J.-Y., Myung, S.-T. & Sun, Y.-K. Sodium-ion batteries: Present and future. *Chem. Soc. Rev.* (2017).